BUBBLE TEMPLATE SYNTHESIS OF HOLLOW GOLD NANOPARTICLES AND THEIR APPLICATIONS AS THERANOSTIC AGENTS

by

CHIENWEN HUANG

Presented to the Faculty of the Graduate School of
The University of Texas at Arlington in Partial Fulfillment
of the Requirements
for the Degree of

DOCTOR OF PHILOSOPHY

THE UNIVERSITY OF TEXAS AT ARLINGTON
August 2010

ACKNOWLEDGEMENTS

I would like to thank all of those who have helped me to carry out the research for this thesis. First of all, I would like to express sincere gratitude to my advisor Dr. Yaowu Hao for his intuitive research advices, patience, and opening the nanotechnology world to me. I would like to give my great thanks to the team at Dr. Hao's laboratory. Shih-Hsin Chang, Punnapob Punnakitikashem, Chivarat Muangphat, Orathai Thumthan, Megha Panuganti and Yijiun Li provided courage and supports.

Finally I would like to thank my wife, Yachi, here in Arlington and my father, mother, brother and sister in Taiwan. They brought me the strength, confidence, and encouragement during my tough education process in graduate school. Without them, this would have been long and painful process.

July 12, 2010

ABSTRACT

BUBBLE TEMPLATE SYNTHESIS OF HOLLOW GOLD NANOPARTICLES AND THEIR APPLICATIONS AS THERANOSTIC AGENTS

Chienwen Huang, PhD

The University of Texas at Arlington, 2010

Supervising Professor: Yaowu Hao

Hollow gold nanoparticle with a sub-30nm polycrystalline shell and a 50 nm hollow core has been successfully synthesized through the reduction of sodium gold sulfite by electrochemically evolved hydrogen. Such hollow gold nanoparticles exhibit unique plasmonic properties. They strongly scatter and absorb near infrared light. In this thesis we seek to understand the formation mechanism of hollow gold nanoparticles in this new synthesis process and their plasmonic properties. Also, we explore their biomedical applications as theranostic agents (therapeutic and diagnostic imaging).

A lithographically patterned electrode consisting of Ag stripes on a glass substrate was used to investigate the formation process of hollow gold nanoparticles. Ag stripes served as working electrode for electrochemically evolution of hydrogen, and adjacent glass areas provided supporting surface for hydrogen nanobubbles nucleation and growth. Hydrogen nanobubbles served as both templates and reducing agents to trigger the autocatalytic disproportionation reaction of sodium gold sulfite. The effects of applied potential and the additives in the electrolyte have been studied. It has been found that the size and size distribution of hollow gold nanoparticle are directly relative to the applied potential, i.e. the hydrogen evolution rate. It has also been found the addition of Ni^{2+} ions can greatly improve the size distribution of hollow gold nanoparticles that can be contributed to that the newly electrodeposited nickel metal can enhance the hydrogen evolution efficiency. Another additive, ethylenediamine (EDA) can suppress the autocatalytic reaction of gold sulfite to increase the stability of sodium gold sulfite electrolyte.

To capture such electrochemically evolved hydrogen nanobubbles, and subsequently to generate hollow gold nanoparticles in large numbers, alumina membranes were placed on the top of the working electrode. Anodic alumina membrane consists of ~200 nm pores, which provides a large surface area for the formation of hydrogen nanobubbles. By this approach, the electroless reaction can be easily separated from the electrodeposition process, and hollow gold nanoparticles can be easily collected.

Synthesized hollow gold nanoparticles exhibit unique plasmonic properties; the surface plasmon resonance (SPR) lies in the near infrared region (NIR). This is very different from the solid spherical gold nanoparticles. Three-dimensional finite difference time domain (FDTD) simulation was employed to study the plasmonic properties of hollow gold nanoparticles. It has been found that the red-shifts of SPR peaks are mainly caused by their surface roughness, and the hollow nature of these particles only plays a minor role. The surface roughness of hollow gold nanoparticles can be tuned by adjusting the pH of the electrolyte (from 6.0 to 7.0) by adding sodium sulfite. Different surface roughness (from smooth to very rough) can be readily obtained, and correspondingly, surface plasmon resonance (SPR) peaks red-shift from ~600 nm to ~750 nm.

Using hollow gold nanoparticles as multifunctional agents for biomedical applications have been explored. Two kinds of agents have been constructed. It has been demonstrated that pegylated Raman dye encoded hollow gold nanoparticles, terms as Raman nanotags, can serve as both diagnostic imaging agents and photothermal therapy agents. When illuminated by near infrared light, the enhanced Raman signal makes the hollow gold nanoparticles to become optically detectable for biomedical imaging, and absorbed light rapidly heat up the hollow gold nanoparticles which can be used to photothermal ablation therapy. The cytotoxicity evaluation using [^{3}H] thymidine incorporation method has shown non-toxicity of the Raman nanotags. The photothermal effects of hollow gold nanoparticles have been examined by two methods: (1) by embedding hollow gold nanoparticles in tissue-like phantom environment; (2) by recording infrared images as temperature increase. The results show that hollow gold nanoparticles are capable to generate sufficiency heat for photothermal therapy. To fully take advantage of the unique hollow core space of hollow gold nanoparticles, a facile route has been develop to trap Fe_3O_4 nanoparticles into the hollow gold nanoparticles to form Fe_3O_4/Au core/shell nanoparticles. Fe_3O_4/Au core/shell nanoparticles possess the desirable magnetic and plasmonic properties that can be used as magnetic resonance contrast (MRI) agents and photothermal therapy agents.

TABLE OF CONTENTS

APPENDIX

LIST OF ILLUSTRATIONS

LIST OF TABLES

Table Page

CHAPTER 1

INTRODUCTION

In recent years, the investigations of gold nanoparticles have greatly increased due to their unique surface plasmon resonance (SPR) optical properties. SPR is an optical phenomenon arising from the interaction between the conduction electrons in a metal and the electromagnetic field. These nanoparticles strongly enhance the scattering and absorption of the electromagnetic field, which leads to several applications such as surface enhanced Raman scattering (SERS)(1-3) , bio-imaging contrast enhancement agents(4, 5) and photothermal therapy(6, 7). The SPR properties of gold nanoparticles are strongly dependent on the size and shape of gold nanoparticles. A variety of methods have been reported to prepare gold nanoparticles with different sizes, and shapes. Spherical solid gold nanoparticles can be easily synthesized with a wide range of size using well-know citrate reduced gold chloroaurate ($HAuCl_4$) method(8). Such as spherical gold nanoparticles with 40-100 nm in diameter have SPR peaks at around 530-560 nm, while those with larger diameter (140 nm) are red-shifted to 650 nm. Several methods have been demonstrated for preparing gold nanorods, including the template-directed method(9), the electrochemical method(10) and the seed-mediated growth method(11). The SPR peak of gold nanorods would split into two modes due to different orientations of the rod with respect to the electric field of incident light. A SPR peak around 530 nm corresponds to the transverse plasmon oscillation, and a stronger SPR peak at NIR region arising from the plasmon oscillation along the longitudinal axis of the nanorods(12). So-called “Gold Nanoshells” were produced by coating silica beads with gold shells of various thicknesses

(13, 14). The SPR peaks of nanoshells could be conveniently tuned by controlling the ratio of shell thickness to particle diameter(15). Another type of composite gold nanoparticles "Gold Nanocages" were produced by replacing Ag nanocubes with $HAuCl_4$ through the galvanic replacement reaction(4, 16, 17). Because the dimension and wall thickness of the resultant gold nanocages are well controlled by the molar ratio of Ag to $HAuCl_{4,}$ their SPR peaks can be shifted to cover a spectral region from 400 to 1200 nm. In this thesis, a new type of gold nanoparticle and its synthesis method will be discussed in details. We discovered the electrochemically evolved hydrogen nanobubbles can be served as templates and reducing agents for the formation of hollow gold nanoparticles through the electroless reaction with sodium gold sulfite. The SPR peaks of hollow gold nanoparticles can be tuned from visible light to near-infrared region by controlling the surface roughness which is detailed in this thesis.

Gold nanoparticles are extensively exploited for *in vivo* biomedical applications particularly for cancer imaging and therapy. Gold nanoparticles are generally considered as biocompatible, as evidenced by the fact that colloidal gold has been safely used to treat rheumatoid arthritis for half a century(18). It also has been reported that the pegylated gold nanoparticles can increase *in vivo* biodistribution and pharmacokinetic properties upon systemic injection(19). Moreover, gold nanoparticles can be functionalized with biomolecules that are specific to receptors over-expressed on cancer cells, in such way gold nanoparticles can conjugate with cancer cells.

The applications of gold nanoparticles to cancer nanotechnology originally come from their SPR effects. The two parts of the SPR phenomenon, scattering and absorption can be utilized for cancer cell imaging and cancer photothermal ablation, respectively. One imaging modality is using Raman scattering.

Raman scattering is dramatically enhanced if the molecules are close to the gold nanoparticle surface(2). This consequence is due to the scattering of the incident light is strongly stimulated at the SPR frequency. This effect is called surface-enhanced Raman scattering(1-3). Surface enhanced Raman scattering (SERS) based techniques have been demonstrated the ability to image a large number of cells, and the potential for rapid multiplexed imaging(20, 21). The advantages of SERS imaging are the capability to monitor particle uptake *in situ* without significant sample preparation and the capability to create multifunctional SERS probes. Therefore, SERS imaging provides highly specific and quantitative information that allows rapid screening of nanoparticle uptake in cell cultures or in tumor sites(22). Recently, gold nanoparticles based Raman tags have been demonstrated their capability to be used for *in vivo* cancer biomarker detection(21, 23).

The therapeutic function of gold nanoparticles has been focused on photothermal ablation. When gold nanoparticles absorb light the free electrons in the gold nanoparticles are excited. At the SPR frequency, this excitation is strongly enhanced causing a collective oscillation of free electrons. Upon the interaction between the electrons and the crystal lattice of gold nanoparticles, the electrons relax and the thermal energy is transferred to the lattice. Subsequently, the heat from gold nanoparticles is dissipated into vicinity leading the death of the cancer cells. Several works have been demonstrated that gold nanoparticles can be used as heat generating agents to ablate the cancer cells(6, 24-27). However, for *in vivo* biomedical applications, there is a principle problem, tissues scatter and absorb light in the visible region, and even near-infrared light can only penetrate relatively tine tissue. Due to this limitation, gold nanoparticles with the SPR peaks in the near-infrared region are required(28).

Recently, another interesting multifunctional nanoparticle, iron oxide/Au core/shell nanoparticle, has become an intensive research topic(29-31). Superparamagnetic iron oxide nanoparticles (SPIONs) have been widely used as magnetic resonance imaging agents in clinic, and the heat-generating capability of SPIONs in the alternating magnetic field has also been studied intensively. To date, the demonstrated methods to combine SPION with gold nanoparticle are limited on coating iron oxide particles with a thin layer of gold in which gold shell retains the ability to be functionalized with biomolecules through the well-developed thiol-Au process. However, the reported results usually have SPR peaks in the visible region, which limit their *in vivo* biomedical applications(32, 33).

The hollow gold nanoparticles produced using above mentioned bubble template synthesis are explored as multifunctional agents for biomedical applications in this thesis. Two kinds of agents have been constructed: 1) Pegylated Raman dye encoded hollow gold nanoparticles, terms as Raman nanotags serving as both SERS diagnostic imaging agents and photothermal therapy agents. 2) Fe_3O_4/Au core/shell nanoparticles fabricated by trapping Fe_3O_4 nanoparticles into the hollow gold nanoparticles serving as magnetic resonance contrast (MRI) agents and photothermal therapy agents.

In this thesis, first, background information about the general synthesis methods and the optical properties of gold nanoparticles are given in Chapter 2. The detailed synthesis process and formation mechanism are described in Chapter 3 and Chapter 4. The understanding optical properties of hollow gold nanoparticles are discussed in Chapter 5. The applications of hollow gold nanoparticles are discussed in Chapter 6. Finally, conclusion is summarized in Chapter 7.

CHAPTER 2

BACKGROUND INFORMATION

In the 20th century, a variety of methods for the preparation of gold colloidal were reported and reviewed. Gold nanoparticles have been an intensive research subject in biomedical applications due to their fascinating optical properties. In this chapter, the methods used to synthesize gold nanoparticles with different sizes and shapes were described, and their optical properties were also discussed. The potential of *in vivo* biomedical applications of gold nanoparticles were introduced followed by the literature reviews on the synthesis methods and optical properties of gold nanoparticles.

2.1 Synthesis of Gold Nanoparticles

Around the 4th century B.C. in Egypt and China, colloidal gold was already used to make ruby glass and for coloring ceramics. One of the most fascinating examples of this technology is probably the famous Lycurgus cup (Figure 2.1) which can be seen in the British Museum in London. This object was made by the Romans in the 4th century features an amazing property of change in colors depending on how the light illuminated it. Reflected light makes it appear green, whereas in transmission a bright red color can be seen. Later, it was evidenced the presence of mixed Au–Ag particles of approximately 70 nm in the glass matrix of the vase. In 1857, Michael Faraday was the first person to report the formation of deep-red solutions of colloidal gold by reduction of an aqueous solution of chloroaurate ($AuCl_4^-$) using phosphorus in CS_2(8). Recently, several methods have been developed to synthesize gold nanoparticles with different sizes and shapes, such as spherical gold nanoparticles(8), gold nanorods(11), gold nanoshells(13) and gold nanocages(34).

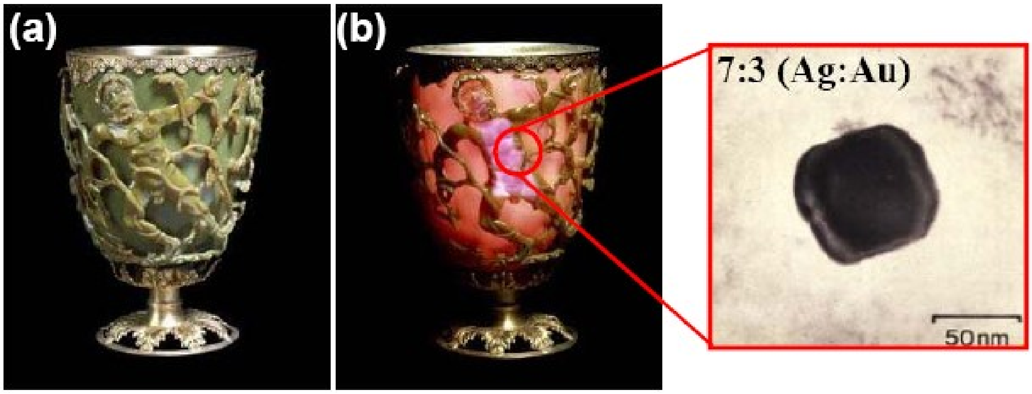

Figure 2.1 Lycurgus cup (a) the reflected light makes it appears green and (b) the transmitted light makes it appear red. The mixed Au-Ag particles of approximately 70 nm present in the glass matrix of the vase(35).

2.1.1 Spherical Gold Nanoparticles

Among the conventional methods of synthesis of spherical gold nanoparticles by reduction of gold(III), the most popular one has been that using citrate reduction of gold chloroaurate ($HAuCl_4$) in water, which was introduced by Turkevitch in 1951(8):

$$6AuCl_4^- + C_6H_8O_7 + 5H_2O \rightarrow 6CO_2 + 24Cl^- + 6Au^0 + 18H^+ \qquad (2\text{-}1)$$

In this method Cl^- and CO_3^{-2} ions resulting from the gold reduction process assemble on the surface in which the metal particles are given a net negative charge to provide the necessary electrostatic forces to maintain colloidal stability(36). In 1994, Brust−Schiffrin introduced a synthesis method which allowed the facile synthesis of thermally stable and air-stable spherical gold nanoparticles with the controllable size. This synthesis technique is to use the thiol ligands that strongly bind with gold due to the strong affinity between gold and S(37). $AuCl_4^-$ is transferred to toluene ($C_6H_5CH_3$) using tetraoctylammonium bromide (TOABr) ($C_{32}H_{68}BrN$) as the phase-transfer reagent and reduced by $NaBH_4$ in the presence of dodecanethiol ($C_{12}H_{25}SH$) (Figure 2.2).

$$AuCl^{-}_{4(aq)} + N(C_8H_{17})_4 + (C_6H_5Me) \rightarrow N(C_8H_{17})_4 + AuCl^{-}_4(C_6H_5Me) \qquad (2\text{-}2)$$

$$mAuCl^{-}_4(C_6H_5Me) + nC_{12}H_{25}SH(C_6H_5Me) + 3me^{-} \rightarrow 4mCl^{-}_{(aq)} + [Au_m(C_{12}H_{25}SH)_n](C_6H_5Me) \qquad (2\text{-}3)$$

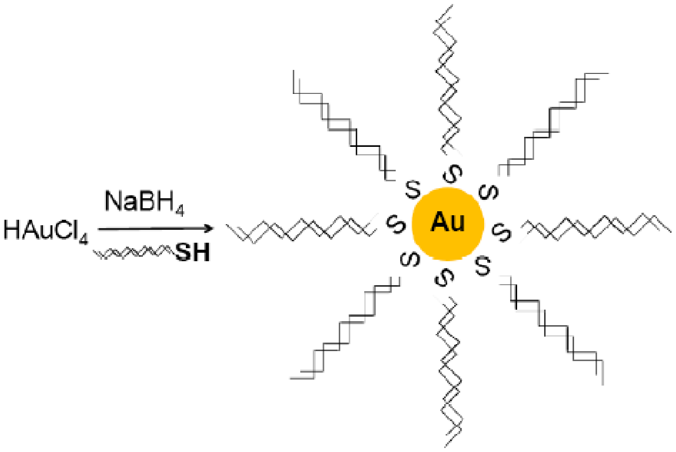

Figure 2.2 Formation of spherical gold nanoparticles coated with organic shells by reduction of Au(III) compounds in the presence of alkanethiols(38).

2.1.2 Gold Nanorods

A variety of methods have been demonstrated for preparing gold nanorods. For example, the template-directed method pioneered by Martin and co-workers(9), the electrochemical method introduced by Wang and co-workers(10), and the seed-mediated growth method demonstrated by Murphy and co-workers(11).

2.1.2.1 Template-Directed Method

The template-Directed method for the synthesis of gold nanorods was first introduced by Martin and co-workers(9). This method is based on the electrochemical deposition of gold within the pores of nanoporous polycarbonate or alumina membranes. Gold nanorods with different diameters can be prepared by controlling the pore diameter of the membrane and the length of the nanorods can be controlled through the amount of gold deposited within the pores of the membrane (Figure 2.3)(39).

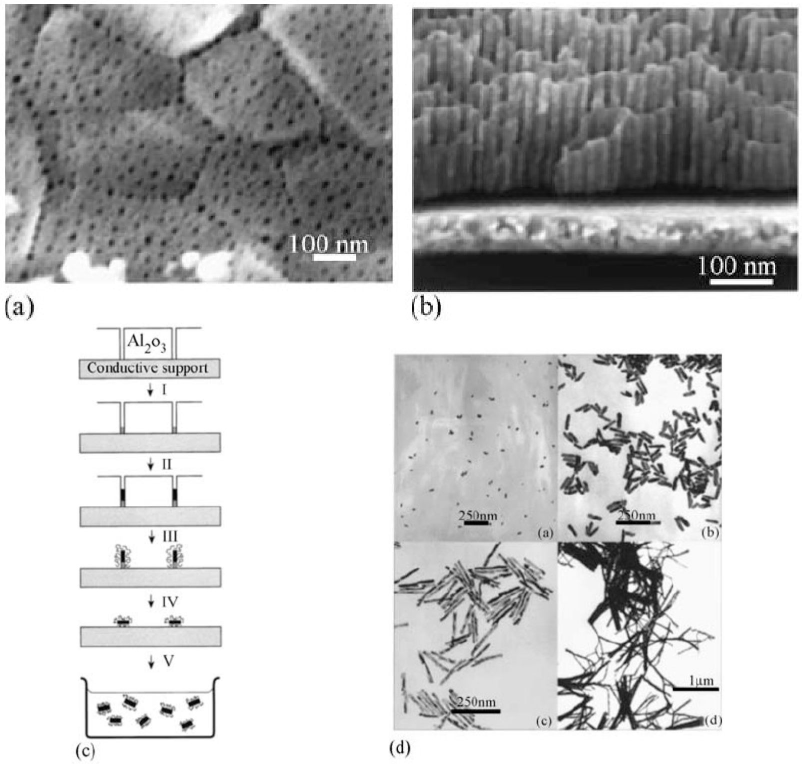

Figure 2.3 (a) and (b) are SEM micrographs of alumina membrane. (c) Schematic representation of the successive stages during formation of gold nanorods via the template method. (d) TEM micrographs of gold nanorods obtained by the template method(39).

2.1.2.2 Electrochemical Method

Using electrochemical method to fabricate gold nanorods was first demonstrated by Wang and co-workers(10). This synthesis process is conducted within a simple two-electrode-type electrochemical cell (Figure 2.4). A gold metal plate is used as a sacrificial anode, and the cathode is a platinum plate. Both electrodes are immersed in an electrolytic solution containing a cationic surfactant, hexadecyltrimethylammonium bromide ($C_{16}TAB$), and a small amount of hydrophobic cationic surfactant, tetradodecylammonium bromide ($TC_{12}AB$), which acts as a rod-inducing co-surfactant. The $C_{16}TAB$ not only serves as the supporting electrolyte but also as the stabilizer for the nanoparticles in terms to prevent their aggregation. Acetone is used for weakening the micellar framework and cyclohexane (C_6H_{12}) is for facilitating the formation of elongated, rod-like C_{16}TAB micelles. Electrolysis is conducted under a constant current mode for a typical period of 20 minutes. During the synthesis, the bulk gold metal is converted from the anode to gold complex ions $AuBr_4^-$, and these ions are driven by the current to the cathode. The reduction reaction takes place at the interfacial region between the cathode and the electrolytic solution. The gold complex ions may also combine with the cationic surfactants to facilitate the formation of rod-like gold nanoparticles. In order to have the better control of the aspect-ratio of the gold nanorods, an additional silver plate is added to the electrolytic solution. The $AuBr_4^-$ produced from the anode oxidizes the silver metal to ions (in the form of AgBr), and it is found that the concentration of silver ions and their release rate can affect the length of the nanorods. This method provides a synthetic route for preparing high yields of gold nanorods.

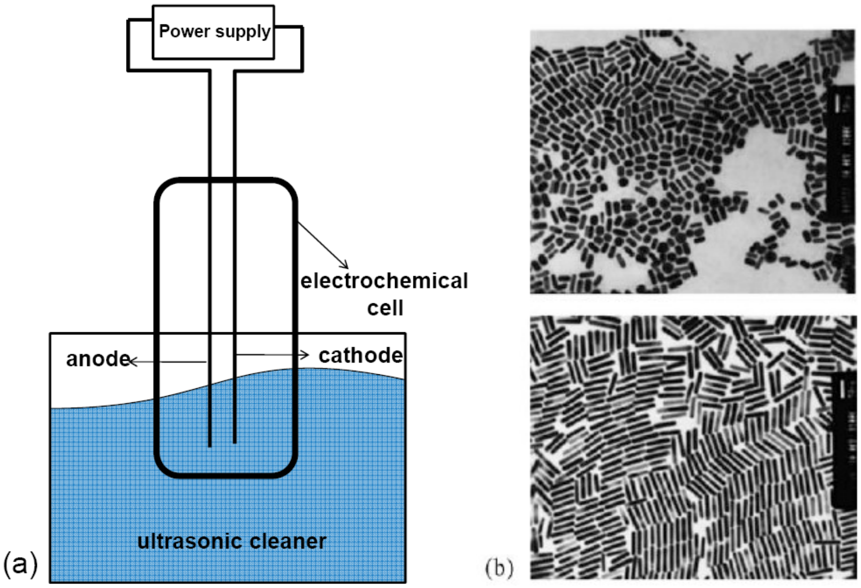

Figure 2.4 Schematic diagram of the set-up for preparation of gold nanorods via the electrochemical method containing (b) TEM micrographs of gold nanorods with different aspect ratio 2.7 (top) and 6.1 (bottom). Scale bars represent 50 nm(10).

2.1.2.3 Seed-Mediated Growth Method

A number of groups have reported the use of seeds to facilitate the formation of monodispersed gold nanorods. Different reducing regents can be employed, such as hydroxylamine (NH_2OH), sodium citrate ($C_6H_5Na_3O_7$), and ascorbic acid ($C_6H_8O_6$). A systematic study has been reported by Murphy and co-workers(11). In a typical process, a solution of 3.5 nm gold seed particles is first prepared by reducing $HAuCl_4$ with sodium borohydride ($NaBH_4$) in the presence of citrate, which only serves as the capping agent since it cannot reduce gold salt at room temperature. A growth solution containing $HAuCl_4$ and $C_{16}TAB$ is mixed with freshly prepared ascorbic acid solution and then added to a seed solution to generate gold nanorods. Although gold nanospheres are also formed in this synthesis, they can be readily removed *via* centrifugation. Most recently, Mulvaney and co-workers investigated the factors affecting the formation of gold nanorods and modified the solution-phase synthesis to adjust the length of the rods from 25–170 nm (Figure 2.5)(40).

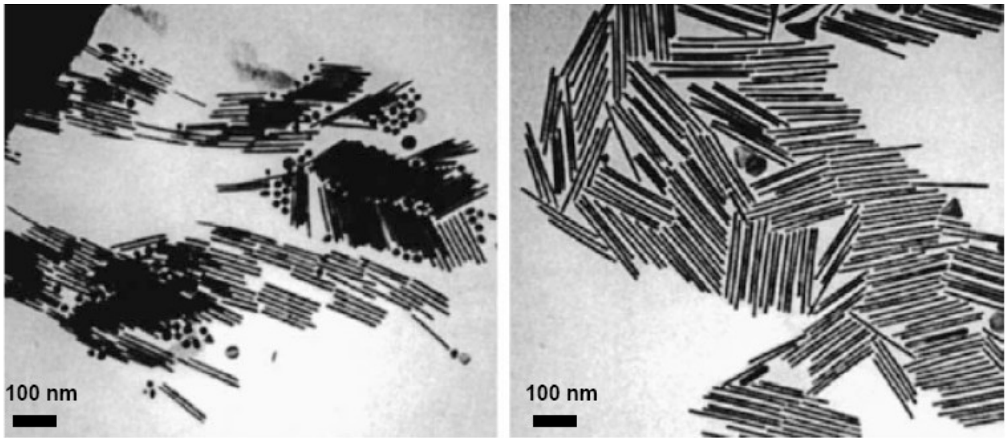

Figure 2.5 TEM micrographs of gold nanorods prepared by the seed-mediated method(40).

2.1.3 Gold Nanocages

Gold nanocages were recently developed by Xia and co-workers(34). Ag nanocubes suspended in solution can be oxidized and replaced by $HAuCl_4$ according to the following replacement reaction.

$$3Ag_{(s)} + AuCl^{-}_{4(aq)} \rightarrow Au_{(s)} + 3Ag^{+}_{(aq)} + 4Cl^{-}_{(aq)} \qquad (2\text{-}4)$$

The silver nanocubes were prepared using a polyol process(41), and then the silver nanocubes reacted with the $HAuCl_4$ to form small holes on a specific face. As reaction continued, gold atoms are deposited on the surface of the silver nanocube to generate a thin shell. The Ag atoms can also diffuse into the gold shell, leading to the formation of a closed box made of Au/Ag alloy. This eventually led to the formation of a hole at each corner of the nanobox as show in Figure 2.6.

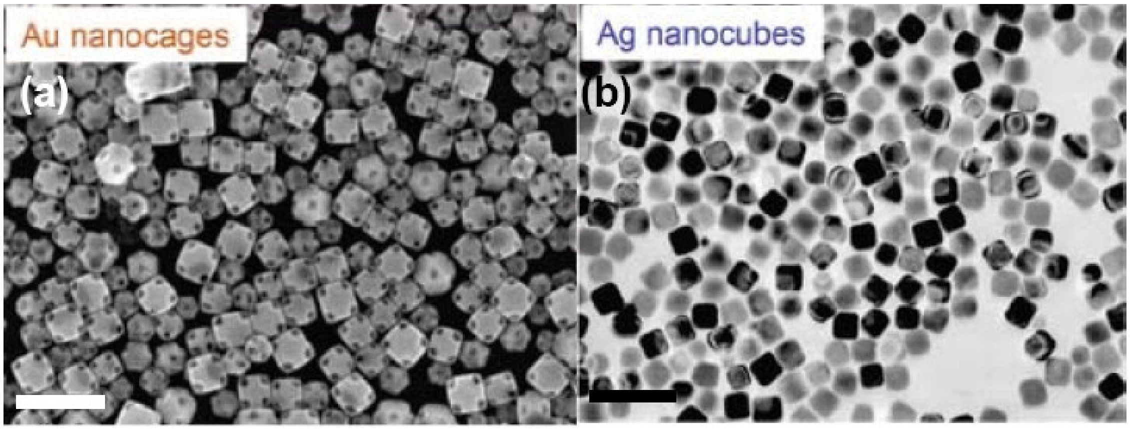

Figure 2.6 (a) SEM micrograph of gold nanocages prepared through the galvanic replacement reaction with Ag nanocubes. (b) The insert is a TEM micrograph. The scale bars are 100 nm for both images(34).

2.1.4 Gold Nanoshells

Gold nanoshells were first engineered by Halas and co-workers(13) with directly depositing gold onto silica colloidal spheres. In a typical process, uniform silica spheres were first synthesized using the Stöber method.

$$\text{Tetraethylorthosilicate(TESO)}(SiC_8H_{20}O_4) + \text{Ammonium hydroxide}(NH_4OH) \text{ in Ethanol} \rightarrow \text{Silica} \qquad (2\text{-}5)$$

The surfaces of silica beads were then modified with a monolayer of amino-terminated silane (either aminopropyltriethoxysilane (APTES) ($C_9H_{23}NOSi$) or aminopropyltrimethoxysilane (APTMS) ($C_6H_{17}NO_3Si$)). The gold shell is grown on the silica cores via the seed-mediated electroless plating. First, small gold colloids (~2nm), were attached to the amine-terminated silica surfaces. Then Gold was electrolessly plated onto the colloidal nucleation sites from diluted solution of gold chloroauric ($HAuCl_4$) and potassium carbonate (K_2CO_3) using formaldehyde (CH_2O) as a reduction agent. The thickness of shell is controlled by the relative amounts of silica core and the gold salt solutions. A continuous gold shell generally has a thickness between 5 and 30 nm as shown in Figure 2.7.

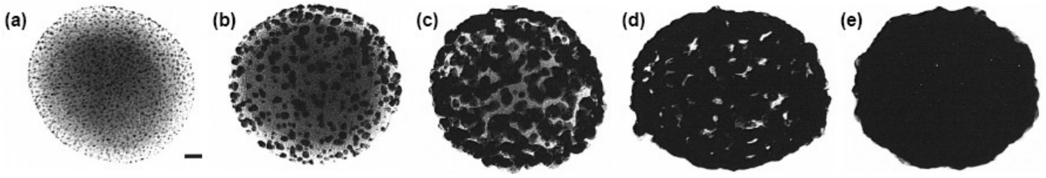

Figure 2.7 TEM micrographs of nanoshell growth on 120 nm diameter silica dielectric nanoparticle. (a) Initial gold colloid-decorated silica nanoparticles (b)–(d) Gradual growth and coalescence of gold colloid on silica nanoparticle surface. (e) Completed growth of metallic nanoshell(13).

2.2 Optical Properties of Gold Nanoparticles

The ruby-red color of colloidal gold suspensions is due to their strong interaction with visible light at around 520 nm. At this wavelength, free electrons in the gold nanoparticles collectively oscillated with the incident electromagnetic wave, a phenomenon known as surface plasmon resonance (SPR).

2.2.1 Surface Plasmon Resonance (SPR)

Surface plasmon resonance (SPR) is a nanoscale size effect of the interaction between the electromagnetic wave and the conduction electrons in a metal. When a metal is under the irradiation of light, the electromagnetic field drives the conduction electrons to oscillate. The collective motion of electrons has its own resonance frequency, plasma frequency, and the quantized plasma oscillations are called plasmons. For a nanoparticle which has the size much smaller than the wavelength of the light, this collective excitation mode of the plasma will be localized near the surface, and the resonance frequency will shift from the plasma frequency to surface plasmon resonance frequency. For some novel metals such as Au, Ag and Cu nanoparticles, the SPR peaks are in the visible region(42). At SPR frequency, these nanoparticles strongly enhance the scattering and absorption of the electromagnetic field. The SPR highly depends on the geometry of the nanoparticles. For the spherical gold nanoparticles with a diameter 40-100 nm, SPR peaks are centered at around 550 nm. For the gold nanorods, the SPR peaks are split into two parts; one is located in the visible light region and the other one can be shifted into near infrared region. For the gold nanoshells and gold nanocages, the SPR peaks can be tuned in the range of 400 nm-1000 nm by controlling the shell thickness.

In order to understand the physical properties behind this phenomenon, two traditional theories were introduced here: First, the Drude-Maxwell model and second, the theory exposed by Gustav Mie. The expression of the dielectric constant of the bulk metal ε(ω) is obtained phenomenologically(43) or with the help of electrostatics(44). In the latter case, the Drude theory has been used.

2.2.2 Electromagnetism in Bulk Metal: Drude-Maxwell Model

In Drude-Maxwell model, the propagation of an electromagnetic wave in a metal can be described by Maxwell equations which expressed as the Equation 2-13 below:

$$\varepsilon(\omega) = \varepsilon_0 + \frac{i\delta(\omega)}{\omega\varepsilon_0} \tag{2-13}$$

where ω is the angular frequency, and ε(ω) is the frequency dependent dielectric constant of the medium in the presence of a wave, and ε_0 is the permittivity of free space, and ε_∞ is the dielectric constant of the surrounding medium and, δ(ω) is the frequency dependent conductivity of the medium.

In order to fully express frequency dependent ε(ω) and δ(ω), the Drude theory of free electrons can be used. The Drude theory describes the mechanics of the electrons inside a metal. Electrons are considered as free and independent. The motion of a whole electron cloud is the sum of the motion of the individual electrons: the coupling between them is thus considered as maximum, electrons acting all in phase(45). The motion of one electron is described by Equation 2-14.

$$m_e \frac{dv}{dt} + m_e \Gamma v = eE \tag{2-14}$$

where m_e stands for the effective mass of the electron, and v is the electron speed, and e is the charge of the electron m, and Γ is the damping constant that is usually fitted with experimental data(46). The second term is a friction due to free electron inelastic collisions, electron-phonon coupling, defects and impurities(46). The third term is the force due to the electric field E. Compared to that of the electric field, the force exerted on the electrons by the magnetic field is negligible. This approximation is justified since electrons are moving very slowly compared to light. It is stated that $E(\omega) = E_0 e^{-i} \omega ^{t}$. Then v will also be sinusoidal, $v(\omega) = v_0 e^{-i} \omega ^{t}$ and Equation 2-14 becomes Equation 2-15:

$$(-i\omega m_e + m_e\Gamma) v_0 e^{-i}\omega^{t} = eE_0 e^{-i}\omega^{t} \tag{2-15}$$

Hence,

$$v_0 = \frac{e}{m_e\Gamma - i\omega m_e} E_0 \tag{2-16}$$

Then j can be expressed as resulting from the individual motion of all electrons, with n, the electron density Equation 2-17.

$$j = env_0 = \frac{ne^2}{m_e\Gamma - i\omega m_e}E_0 = \delta(\omega)E_0 \tag{2-17}$$

$$\delta(\omega) = \frac{ne^2}{m_e\Gamma - i\omega m_e} \tag{2-18}$$

δ(ω) has given by Equation 2-18. By injecting Equation 2-18 into Equation 2-13, finally, the dielectric constant can be expressed as a function of known constants: ε_∞, n, e, m_e and ε_0, of the frequency ω and of Γ in Equation 2-19.

$$\varepsilon(\omega) = \varepsilon_\infty - \frac{\omega_p^2}{\omega^2 + i\omega\Gamma} = \varepsilon_\infty - \frac{\omega_p^2}{\omega^2 + \Gamma^2} + i\frac{\omega_p^2\Gamma}{\omega(\omega^2 + \Gamma^2)} \tag{2-19}$$

$$\omega_p = (\frac{ne^2}{\varepsilon_0 m_e})^{1/2} \tag{2-20}$$

ω_p is known as the plasma frequency.

However, in the case of nanoparticles, the Drude-Maxwell model became incorrect. The reason is that the electron density is no longer uniform in nanoparticle which means the charges tend to accumulate at nanoparticle edges. Because the size of nanoparticle is much smaller than the wavelength of incident light, all the electrons are confined in a nanoparticle seeing the same field at a given time(45). The electric field is considered as independent of the position. This hypothesis is called the *quasi-static* approximation. The displacement of the electron cloud under the effect of the electric field leads to the creation of surface charges, positive where the cloud is lacking, negative where it is concentrated as shown in Figure 2.8 (45). The electrons are moving collectively while under the effect of the electromagnetic field. Such collective oscillation leads to plasmon dipolar(45). This plasmon dipolar charge places a new force on the electron cloud, and then the electrons undergo a restoring force which conflicts with the external electric field.

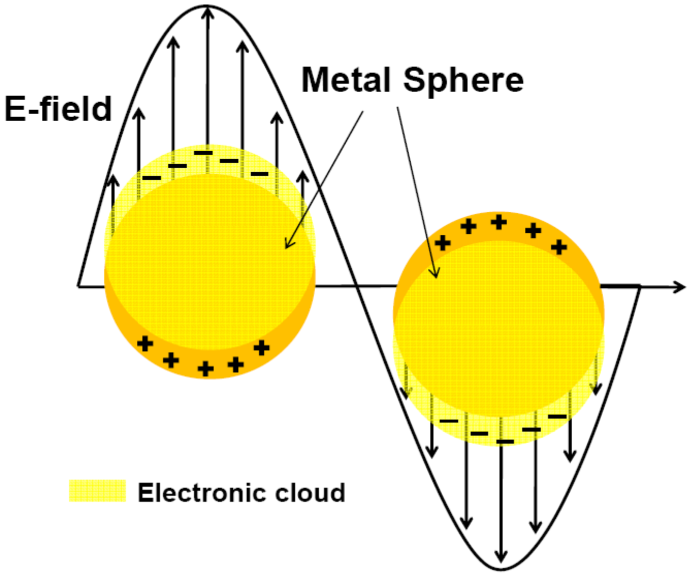

Figure 2.8 Schematic description of the interaction of a metal nanosphere with light. The electromagnetic field of the light induces a coherent dipolar oscillation of the metal conduction electrons across the nanoparticle.

2.2.3 Optical Properties of Spherical Gold Nanoparticles

The most popular theory to explain the color of suspension of gold nanoparticles was published in 1908 by Gustav Mie(47). Mie explained the origin of this SPR phenomenon by solving Maxwell's electromagnetic equation for the interaction between the light and the spherical nanoparticles with the appropriate boundary conditions. The theory has been proved extremely useful for predicting and explaining the extinction spectra of colloidal nanoparticles made of various materials. The extinction efficiency factor σ_{ext} is defined as the ratio of the extinction cross-section to the physical cross-sectional area (πR^2), and it is a sum of both scattering and absorption efficiency. The extinction cross-section (σ_{ext}) of the nanospheres can be obtained as a series of multipole oscillations if the boundary conditions are specified. When the radius of the spherical particle is much smaller than the wavelength of the radiation ($R \ll \lambda$), the dipole oscillation is the only contributor to the extinction cross-section. In the case of 20 nm gold nanoparticles, dipolar plasmon absorption is the dominant contribution. The electrodynamics calculation can be simplified by ignoring high order terms. This gives the most popular form of Mie theory for spherical nanoparticles (48):

$$\sigma_{\mathrm{ext}}(\omega) = 9\frac{\omega}{c}\varepsilon_{m}^{3/2}V\frac{\varepsilon_{2}(\omega)}{[\varepsilon_{1}(\omega) + 2\varepsilon_{m}]^{2} + \varepsilon_{2}(\omega)^{2}} \tag{2-21}$$

where V is the nanoparticle volume, and ω is the angular frequency of the exciting light, and c is the speed of light, and ε_m is the dielectric constant of the surrounding medium, and $\varepsilon = \varepsilon_1 + i\varepsilon_2$ is the complex dielectric constant of the nanoparticle. A resonance peak occurs whenever the condition of $\varepsilon_1 = -2\varepsilon_m$ is satisfied(45). Figure 2.9 shows the extinction spectra calculated using Mie theory for spherical solid gold nanoparticles of different sizes, as well as aqueous solutions containing the spherical solid gold nanoparticles. The peak slightly shifts to the red and becomes broader as the particle diameter increases to 100 nm(49).

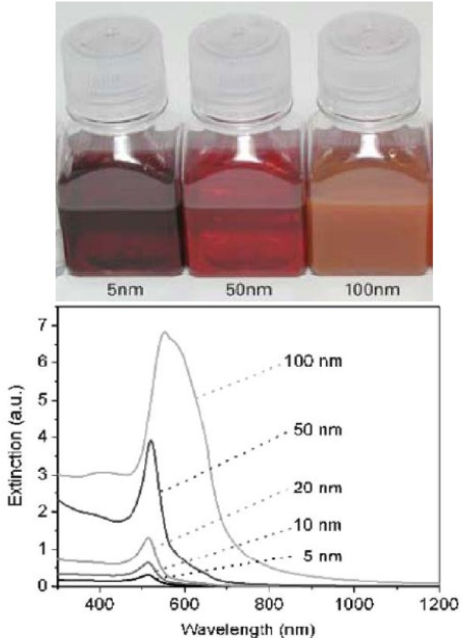

Figure 2.9 Extinction spectra calculated using Mie theory for solid spherical gold nanoparticles with varying diameter from 5 nm to 100 nm(49), as well as the aqueous containing spherical gold nanoparticles.

2.2.4 Optical Properties of Gold Nanorods

In 1912, Gans modified Mie theory and predicted that for rod-shape nanoparticles the SPR peaks would split into two modes due to different orientations of the rod with respect to the electromagnetic field of the incident light(12). According to Gans's theory, the extinction cross-section of rod-shape nanoparticles can be expressed as(48):

$$\sigma_{ext} = \frac{\omega}{3c}\varepsilon_m^{3/2} V \sum_j \frac{(1/P_j^2)\varepsilon_2}{\{\varepsilon_1 + [(1-P_j)/P_j]\varepsilon_m\}^2 + \varepsilon_2^2} \qquad (2\text{-}22)$$

where V is the volume of the rod-shape particle, P_j ($j = A, B, C$; $A > B = C$, A = length, $B = C$ = width) are the depolarization factors for the elongated particles (nanorods), which are given by:

$$p_A = \frac{1-e^2}{e^2}\left[\frac{1}{2e}\ln\left(\frac{1+e}{1-e}\right) - 1\right] \qquad (2\text{-}23)$$

$$P_B = P_C = \frac{1-p_A}{2} \qquad (2\text{-}24)$$

$$e = \left[1-\left(\frac{B}{A}\right)^2\right]^{1/2} = \left(1-\frac{1}{R^2}\right)^{1/2} \qquad (2\text{-}25)$$

where e is the rod ellipticity given by $e^2 = 1 - \xi^{-2}$, and ξ is the aspect-ratio (A.R.) of the nanorod ($\xi = A/B$). These equations can be used to calculate the extinction cross-section of gold nanorods of any aspect-ratio. With the known values for the complex dielectric constant of gold(43), Equation 2-22 is plotted in Figure 2.10 for different aspect ratios of gold nanorods(50). It can be seen that two maxima are present in the calculated absorption spectra corresponding to the transverse and longitudinal resonances. The absorption maximum of the transverse mode shifts to shorter wavelength with increasing aspect ratio.

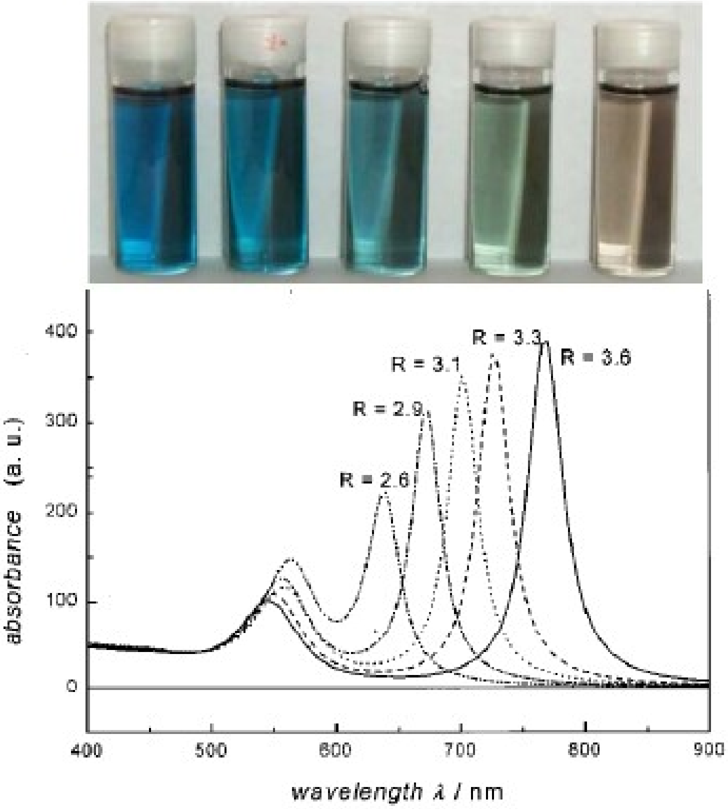

Figure 2.10 Calculated absorption spectra of gold nanorods with varying aspect ratios R using Equation 2-22(50).Upper panel: the color of gold nanorods changes with aspect ratio.

2.2.5 Optical Properties of Gold Nanoshells

In 1989, Neeves and Birnboim proposed a composite spherical nanoparticle which consists of a dielectric core and a metallic shell could give a tunable surface plasmon resonance over a broad range of the spectrum(51). Halas and co-workers(13) were the pioneers to engineer gold nanoshell which consists of a spherical dielectric core encapsulated by a thin gold metal shell(13). The ratio of core to shell thickness rules the scattering and absorbing properties of gold nanoshells. For a given core radius, decreasing the shell thickness shifts SPR peak to longer wavelength as shown in Figure 2.11(15).

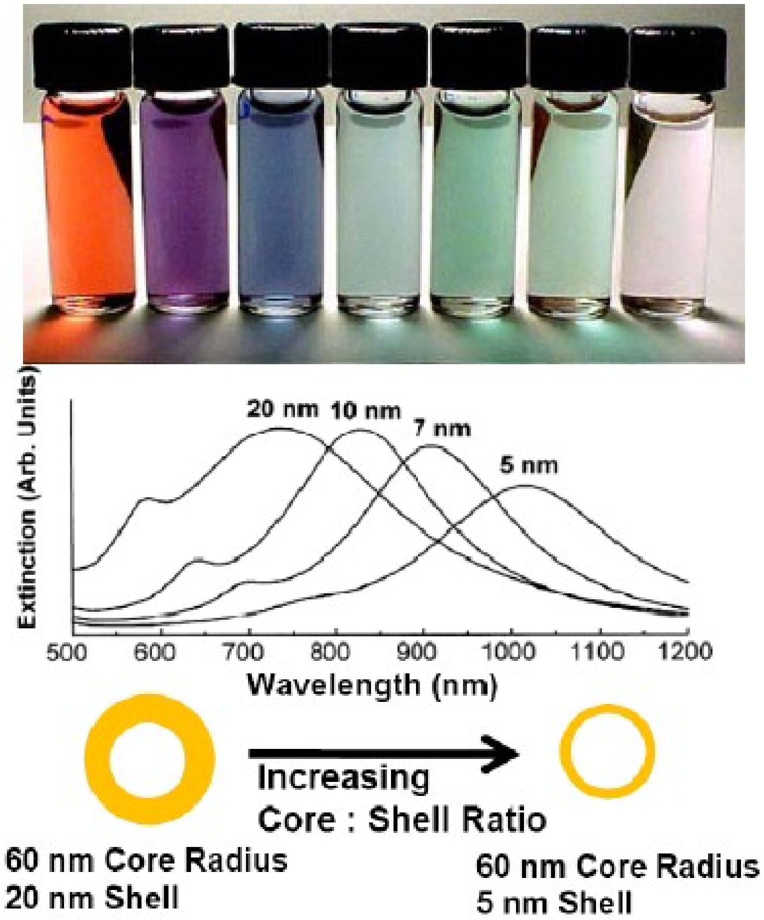

Figure 2.11 Theoretically calculated optical resonances of gold nanoshells silica core, gold shell(15). Upper panel: the color of gold nanoshells changes with the ratio of core to shell thickness.

Using the geometry depicted in Figure 2.12, the full electromagnetic behavior of the nanoshells can be calculated using Mie theory. Mie theory predicts the polarizability Equation 2-26 of nanoshells based on their size and the dielectric functions of the core (ε_1), shell (ε_2), and embedding medium (ε_3)(15, 52). Because the particle diameter is much smaller than the wavelength of incident light ($R<<\lambda$), *quasi-static* approximation calculations are used to simplify the equations. The permittivity of free space is ε_0; ε_a and ε_b are defined in Equation 2-27 and Equation 2-28; and P (Equation 2-29) defines the relationship between the inner radius r_1 and outer radius r_2. As the denominator of Equation 2-26 approaches zero, maximum polarizability is reached and plasmon resonance occurs. The relationship between the core/shell ratio and the plasmon resonance is seen in Equation 2-30.

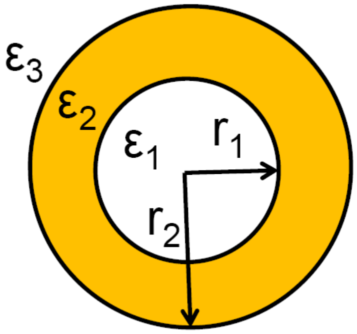

Figure 2.12 Geometry for metal nanoshell consisting of dielectric functions for embedding medium (ε_3), shell (ε_2), and core (ε_1), as well as core to total radii (r_1) and (r_2) respectively. These dimensions and constants are used to define the resonance conditions outlined in Equation 2-18 to Equation 2-22(15).

$$\alpha = 4\pi\varepsilon_0 r_2^3\left[\frac{\varepsilon_2\varepsilon_a - \varepsilon_3\varepsilon_b}{\varepsilon_2\varepsilon_a + 2\varepsilon_3\varepsilon_b}\right] \tag{2-26}$$

$$\varepsilon_a = \varepsilon_1(3 - 2P) + 2\varepsilon_2 P \tag{2-27}$$

$$\varepsilon_b = \varepsilon_1 P + \varepsilon_2(3 - P) \tag{2-28}$$

$$P = 1 - \left(\frac{r_1}{r_2}\right)^3 \tag{2-29}$$

$$\frac{r_1}{r_2} = \left[1 + \frac{3}{2}\frac{\varepsilon_2'(\lambda)(\varepsilon_1 + 2\varepsilon_3)}{[\varepsilon_2'(\lambda)]^2 - \varepsilon_2'(\lambda)(\varepsilon_1 + \varepsilon_3) + \{\varepsilon_1\varepsilon_3 - [\varepsilon_2''(\lambda)]^2\}}\right]^{1/3} \tag{2-30}$$

However, as the shell thickness of nanoshells increases for a given core radius, the *quasi-static* approximation ($R << \lambda$) is no longer can be applied. Due to the increase of the overall nanoparticle size, the electric field of incident light at a given wavelength is no longer uniform over the entire particle (all the electrons are not seeing the same field at a given time). This effect is known as phase retardation which increases the multipolar oscillations of the nanoshells and prevents the dipole from being tuned to shorter wavelengths that results in the generation of higher order plasmon modes, such as quadrupole, octupole, etc(13, 53).

Recently, new conceptual model “plasmon hybridization” has been developed for understanding the optical properties of nanoshells(54). For this concentric nanostructure, the energy level of the nanoshell depends on the interaction of two hybridized plasmons which are the sphere (the outer surface of the metallic shell layer) and the cavity (the inner surface of the shell layer). A thin shell results in strong plasmon hybridization caused the red-shift of the plasmon which also can be understood as an increase in the interaction of the sphere and cavity. However, the apparent blue-shift of the plasmon resonance can be observed with the increase of the shell thickness. As this interaction between sphere and cavity becoming weaker, the plasmon resonance frequency approaches to as a solid nanosphere as shown in Figure 2.13.

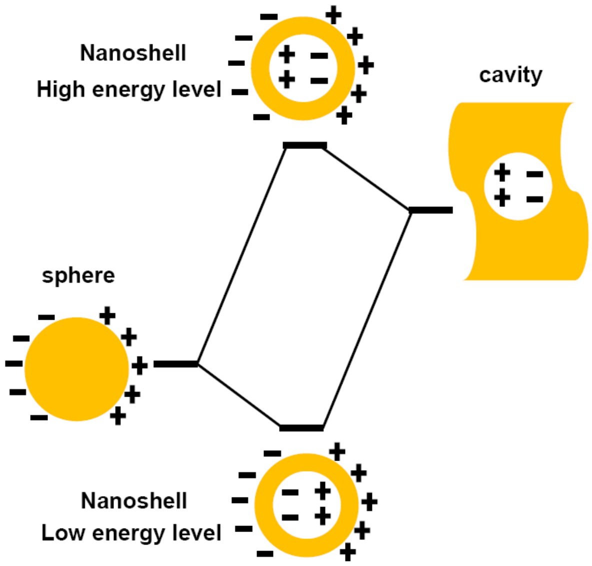

Figure 2.13 An energy-level diagram describing the plasmon hybridization in metal nanoshell resulting from the interaction between the sphere and cavity plasmons(54).

2.2.6 Numerical Methods

Analytical solutions have been used to describe the surface plasmon modes of some complex structures, including cubes(55), hemispheres(56), nanoshells(57, 58) nonconcentric nanoshells(59). However, in order to understand the optical response of more complex nanostructures, such as nanocages(16), it is necessary to use computational approaches capable of handling arbitrary geometries. Among the numerical methods, most commonly used are the discrete dipole approximation (DDA)(44) and the finite difference time domain (FDTD) method(60).

In DDA, the whole particle and its environment are divided into elementary cubic volumes each characterized by their position and their polarizability. If the box size is small enough, they can be considered as dipoles (no higher multipole oscillations need to be taken into account). The polarization of each cubic box results from the local electric field in the box. This field can be seen as the sum of an external electromagnetic field (induced by incoming light) and the field induced by the polarization of the surrounding boxes. Various numerical methods can then be used to determine the time dependent value of the electromagnetic field in the boxes. DDA thus provides a very precise mapping of the field enhancement induced by incoming light in resonating nanoparticles. Figure 2.14 shows the SPR spectra of gold nanocages calculated by using DDA method(16).

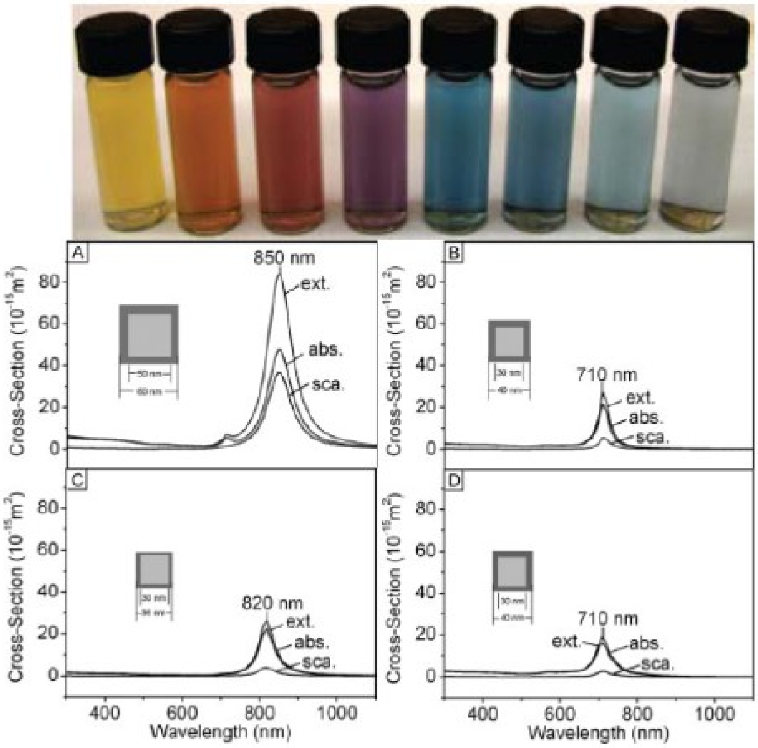

Figure 2.14 Extinction calculated using the DDA method for gold nanocages having four different sets of geometric parameters: (A) a Au nanobox 50 nm in inner edge length and 5 nm in wall thicknes; (B) a Au nanobox 30 nm in inner edge length and 5 nm in wall thickness; (C) the same as in (B), except that the wall thickness is 3 nm; and (D) the same as in (B), except that eight corners are decorated with triangular holes 5 nm in length(16). Upper panel: the color of gold nanocages changes with the volume of $HAuCl_4$ solution.

FDTD also relies on the use of a discrete mapping of the space to resolve the Maxwell Curl equations replacing all the derivatives by finite differences (including the time differences). As underlined by Oubre and Nordlander(58), this method enables one to follow the time evolution of the local electric field using a highly time saving algorithm. FDTD method has become the powerful method for solving Maxwell's equations in complex geometries. It is a fully vectorial method that naturally gives both time domain, and frequency domain information also offering unique insight into all types of nanostructures. The technique is discrete in both space and time. The electromagnetic fields and structural materials of interest are described on a discrete mesh made up of so-called Yee cells. Maxwell's equations are solved discretely in time, where the time step used is related to the mesh size through the speed of light. This technique is an exact representation of Maxwell's equations in the limit that the mesh spacing goes to zero. Structures to be simulated can have a wide variety of electromagnetic material properties. Multiple sources may be added to the simulation and subsequent iteration results in the electromagnetic field propagation. In this thesis, the FDTD method was applied to simulate the plasmonic properties of hollow gold nanoparticles.

2.3 *In Vivo* Biomedical Applications of Gold Nanoparticles

Gold nanoparticles have been extensively explored for *in vivo* biomedical applications particularly for cancer imaging and therapy. Generally, gold nanoparticles are regarded as biocompatible, and no acute cytotoxicity has been observed so far(61). The colloidal gold has been safely used to treat rheumatoid arthritis for half a century(18). Moreover, gold nanoparticles can be easily functionalized with targeting biomolecules through well-established thiol-gold conjugation chemistry.

The applications of gold nanoparticles to cancer nanotechnology originate from their SPR effects. SPR resulted in the enhancement of scattering and absorption of the local electromagnetic field at the metal surface which has made gold nanoparticles as attractive candidates for cancer imaging(21, 23) and photothermal therapy agents(62). For *in vivo* biomedical applications, it required deeper penetration of NIR light. The reason is because the primary absorbers in tissue are water, and blood (hemoglobin and oxyhemoglobin) and both are slightly" transparent" in the NIR range(28) as shown in Figure 2.15. Therefore, by designing gold nanoparticles with SPR peaks in this NIR region, the NIR light is preferentially scattered and absorbed by gold nanoparticles and doesn't attenuate by the tissue.

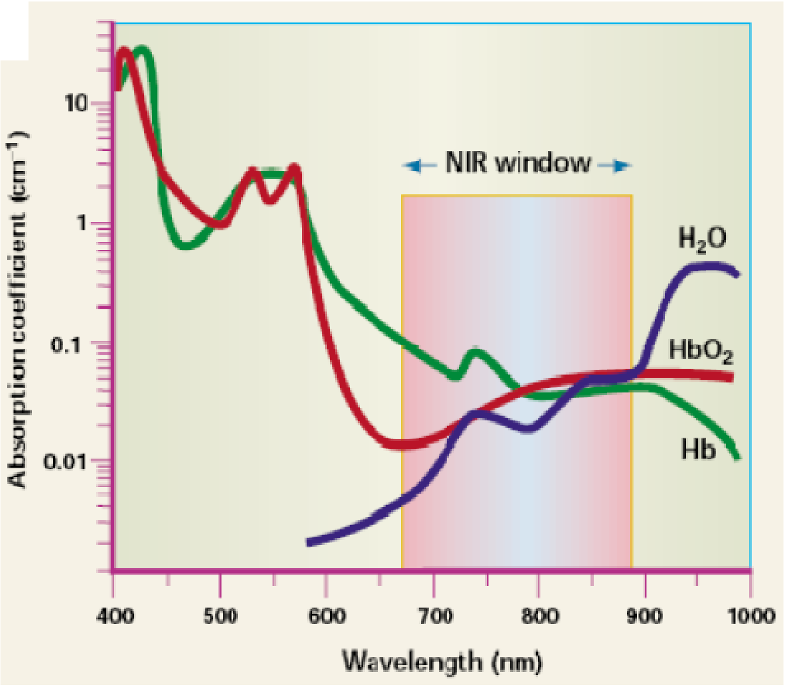

Figure 2.15 Spectras of the major chromaphores in tissue. The major chromophores in tissue have a collective minimum in the near infrared region, allowing deep penetration of light(28).

2.3.1 Gold Nanoparticles as Diagnostic Agents

The development of new and early cancer diagnostic techniques is contributing to an increase in cancer survival rates(63). Researchers are trying to improve the resolution of the conventional imaging techniques and developing new imaging modalities. The performance of these platforms could be increased through integration with appropriate contrast enhancement agents such as gold nanoparticles. Optical coherence tomography (OCT)(64, 65) and surface-enhanced Raman scattering (SERS)(1-3) using gold nanoparticles as agents are promising diagnostic techniques for *in vivo* imaging. These gold nanoparticles possess larger and tunable absorption and scattering cross-section.

2.3.1.1 Optical Coherence Tomography (OCT)

The OCT is based on the a Michelson interferometer, which measures the interference signal between the backscattered light of a sample and a reference, Thus image contrast increased primarily from the intrinsic scattering and absorption of light by tissue. As a result, it is hard to resolve the minor morphological changes involved in the early stage development of a disease. But this effect can be enhanced by gold nanoparticles with their large absorption and scattering cross-section. Xia and co-workers(16) have demonstrated that using gold nanocages as contrast agents for the OCT technique. The OCT was performed on phantom samples with gold nanocages. As a laser with a central wavelength 825 nm was scanned over the tissue phantom, the intensity of backscattered light was measures as a function of depth. Because of the intense absorption of the gold nanocages, a strong modulation of the backscattered spectrum can be observed at blue side of the OCT source spectrum.

2.3.1.2 Surface-Enhanced Raman Scattering (SERS)

Raman spectroscopy is the measurement of the wavelength and the intensity of the inelastically scattered light and has been widely used as an analytical tool for the chemical research. The Raman effect is an inelastic scattering of light as a result of its interaction with material. The incident light is scattered inelastically by the vibrational states of molecules. Typically, Raman signals are quite weak and therefore a sufficient analyze concentration is needed in order to provide enough signal. Raman scattering is dramatically enhanced if the molecules are close to the gold nanoparticle surface(2) as illustrate in Figure 2.16. This effect is called surface-enhanced Raman scattering (SERS)(1-3). Based on this enhancement on gold nanoparticles, SERS is an alternative candidate to fluorescence for biomolecular sensing. Compared to fluorescence, gold nanoparticles are more stable and they do not suffer from photobleaching which is the major limitation for fluorescence based methods.

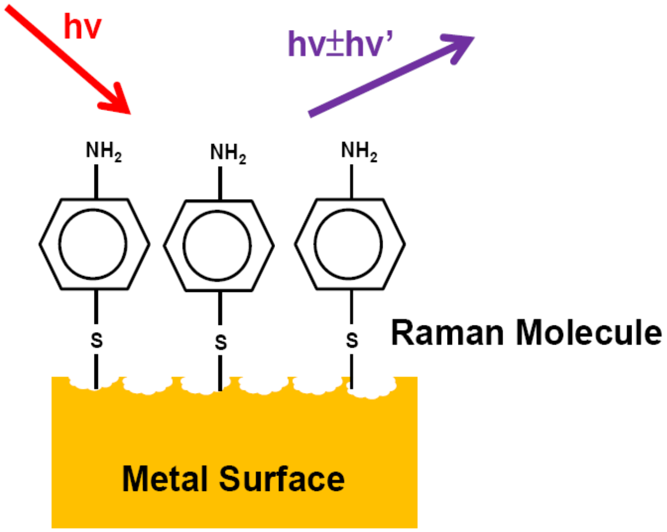

Figure 2.16 Illustration of surface enhanced Raman scattering (SERS). The red light represents the incident light and the purple line is the Raman shifted emitted light.

Recently, SERS based techniques have been demonstrated the ability to image a large number of cells, and the potential for rapid multiplexed imaging(20, 21). The advantages of SERS imaging are the capability to monitor particle uptake *in situ* without significant sample preparation and the capability to create multifunctional SERS probes. Therefore, SERS imaging provides highly specific and quantitative information that allows rapid screening of nanoparticle uptake in cell cultures or in tumor sites(22). Nie and co-workers have demonstrated that using gold nanoparticles based SERS technique for *in vivo* cancer biomarker detection(23). In their work the pegylated Raman dye encoded spherical gold nanoparticles were functionalized with ScFv antibody to target with EGFR-positive tumors and then the strong enhanced Raman signal can be detected optically.

2.3.2 Gold Nanoparticles as Photothermal Agents

Cancer cells are more sensitive on heat damage than health tissue(64), heat induced cell death is used as a noninvasive cancer treatment method. Several kinds of gold nanoparticles have been demonstrated that they can be used as photothermal therapy agents such as spherical gold nanoparticles, gold nanorods and gold nanoshells. All of them have shown their capability to generate localized heat to induce cancer cell death only in the nearby area of the nanoparticles while limiting the damage to the surrounding health tissues.

2.3.2.1 Spherical Gold Nanoparticles

Spherical gold nanoparticle has the SPR peak located at approximately 530 nm where chromaphores also have high absorbance at this wavelength(28). The overlapping of the absorption peak decreases the efficiency of induced heat to tumor sites. Nevertheless, the red-shifted SPR peak can be achieved with aggregated gold nanoparticles. As the nanoparticles are accumulated on the cancer cells, the absorption peak can shift from 530 nm to as far as 1000 nm(65). This ensured the near infrared light can easily penetrate the tissue and the majority of light is absorbed by gold nanoparticles, thereby heating the cancer cells. Unfortunately, the red shift is dependent on the concentration of the gold bound to each cell and may not be reproducible or controllable among samples.

2.3.2.2 Gold Nanorods

Unlike spherical gold nanoparticles, the SPR peaks of gold nanorods can be tuned to strongly absorb NIR by controlling the aspect ratios(50). The overall concept is very straightforward; gold nanorods with SPR peaks in the NIR region accumulate at the tumor site. The SPR peak is in the NIR region where tissue absorption is minimal, permitting optimal penetration(28). When the tumor site is exposed to NIR radiation which the nanorods absorb intensely because of SPR effect, the absorbed energy is efficiently converted into heat leading to thermal destruction of the tumor. El-Sayed and co-workers(66) have demonstrated that gold nanorods can be used as heat-generating agents for *in vivo* photothermal therapy. In their study, the pegylated gold nanorods were conjugated to anti-EGFR antibodies enabling selective photothermal therapy due to their preferential binding onto human oral cancer cells. A NIR laser with a wavelength 800 nm, overlapping with the SPR absorption maximum of the gold nanorods (aspect ratio of 3.9), was used for the photothermal ablation of cancer cells which binding with the gold nanorods. After exposure to a NIR laser, tumor cells stop growing.

2.3.2.3 Gold Nanoshells

Multiple *in vivo* studies have also demonstrated the efficiency of gold nanoshells for the non-invasive treatment of tumors through targeted photothermal ablation(67, 68). O'Neal and co-workers have successfully treated mice inoculated with tumors using this technique(67). In their experiment, mice were inoculated subcutaneously with colon cancer cells and pegylated gold nanoshells solution was injected into mice via a tail vein. After certain time, gold nanoshells were accumulated on the tumor sites and the NIR light at 808 nm was illuminated. The results show a complete destruction of tumors and all mice were healthy and free of tumors up to 90 days after NIR treatment. Although gold nanocages have also shown that the SPR peaks can be shifted to cover a spectral region from 400 to 1200 nm by controlling the porosity of the shells(4, 16, 17), and the ability of gold nanocages to mediate the photothermal destruction of targeted cancer cells *in vitro*(69, 70). However, the details of *in vivo* studies carried out with gold nanocages have not yet been reported.

CHAPTER 3

BUBBLE TEMPLATE SYNTHESIS OF HOLLOW GOLD NANOPARTICLES ON THE ELECTRODE SURFACE

3.1 Introduction

The electrodeposition using aqueous electrolyte is usually accompanied by simultaneous hydrogen evolution. Hydrogen evolution could cause extremely rough deposited surface due to small hydrogen bubbles generated and absorbed on electrode surfaces(71). Therefore, hydrogen evolution has usually been regarded as undesired and deliberately suppressed during the electrodeposition process.

However, we have found that the electrochemically evolved hydrogen nanobubbles can be used as templates and the reducing agents for the formation of hollow nanoparticles through the electroless reaction with gold sulfite electrolyte. Figure 3.1 shows the SEM micrograph of hollow interior of gold nanoparticles after this electrodeposition process. In order to confirm this hypothesis, we conducted a systematic study, which is discussed in detail in this chapter.

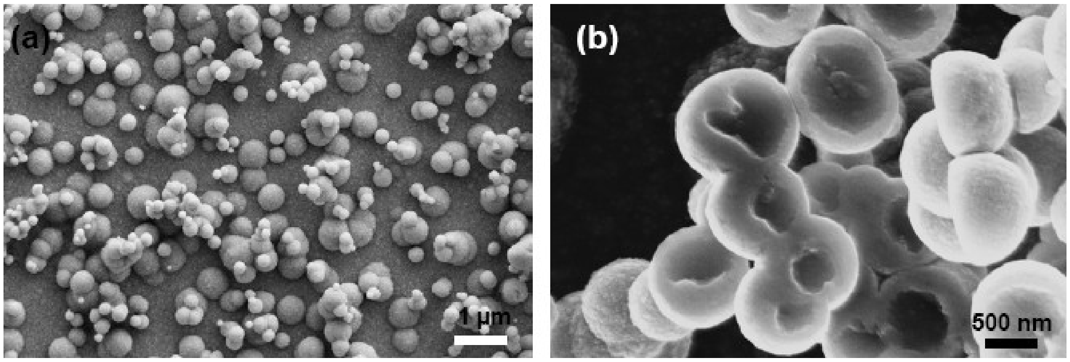

Figure 3.1 SEM micrographs show (a) spherical particles were formed on the conductive substrate surface and (b) bowl-shape gold nanoparticles were revealed after peeled from the deposited thin film.

A lithographically pattered electrode consisting of Ag stripes on a glass substrate was used. The Ag stripes were used as working electrode for electrochemically evolved hydrogen and the glass areas provided the surface for the nucleation and growth of the hydrogen bubbles. When a potential more negative than hydrogen evolution equilibrium potential is applied to Ag stripes, a large number of gold nanoparticles were formed on the glass areas. Since electrodeposition can only occur on Ag electrode surface, electroless reaction would be the only reason for the formation of gold nanoparticles on glass areas.

The formation mechanism of hollow gold nanoparticles could be described as a three-stage process. In the first stage, at a certain overpotential, hydrogen evolution starts, and hydrogen nanobubbles form on the substrate surfaces. In the second stage, the Au^+ ions were reduced into metallic gold by hydrogen nanobubbles and this reduction takes place at the hydrogen bubble boundary. In the last stage, autocatalytic disproportionation reaction (Equation 3-1) occurs in the gold sulfite electrolyte.

$$3Au^{+1}(\text{in sulfite complex}) \xrightarrow{\text{on Au surface}} 2Au^{0} + Au^{3+} \qquad (3\text{-}1)$$

The effects of additives and applied potential on the formation of hollow gold nanoparticles have been investigated. The stability of electrolyte plays an important role in the synthesis process. It has been investigated in both gold cyanide and gold sulfite electrolyte solutions. As expected, only Au^+ ions in sulfite complex were able to be reduced by electrochemically evolved hydrogen nanobubbles. It has shown that the stabilizer ethylenediamine (EDA), a key additive, was not only able to increase the stability of the gold sulfite electrolytes, but also able to clean surface oxides from active metal electrode, and thus lead to the increase of hydrogen evolution efficiency. It also has been found that the size distribution of hollow gold nanoparticles was improved by the addition of Ni^{2+} ions in the electrolyte. The cyclic voltammetry (CV) measurement revealed that the electrodeposited nickel metal was able to enhance the hydrogen evolution efficiency, leading to the better size distribution of hollow gold nanoparticles.

We have directly observed gold metal formation around electrochemically evolved hydrogen bubbles. However, reduction did not take place around the directly pumped hydrogen gas bubbles. We speculated that hydrogen gas bubbles are less reactive than electrochemically evolved hydrogen bubbles. It is impossible to generate nanoscale bubbles by directly pumping gas into the solution, so that the hydrogen molecular concentration inside the electrochemically evolved nanobubble can be many magnitudes larger than the pumping approach.

3.2 Experiment

3.2.1 Preparation of Electrolytes and Substrates

The electrolytes used in the electrodeposition were prepared with reagent-grade chemicals. Gold cyanide solution with a pH~6.8 was purchased from VWR. The sodium gold sulfite solution (($Na_3Au(SO_3)_2$) with a pH~10.5 was purchased from Colonial Metals Inc., and diluted to 10% with deionized water, terms as self-prepared gold sulfite solution. The 99% ethylenediamine (EDA) was diluted to 50% with deionized water and used as a stabilizing additive to suppress the disproportionation of gold sulfite complex. 0.4 M nickel sulfamate tetrahydrate ($Ni(SO_3NH_2)_2 \cdot 4H_2O$) with a pH~5.8 was prepared. All the prepared sodium gold sulfite electrolytes were acidified with 5% sulfuric acid to reach a pH~6 except gold cyanide solution. The electrodeposition experiments were conducted potentiostatically using a typical three-electrode cell with a Ag/AgCl electrode in 3 M NaCl solution as the reference and a platinum mesh as the counter electrode. Potentials were applied to the working electrode using a Princeton Applied Research 273A Potentiostat/Galvanostat as illustrated in Figure 3.2.

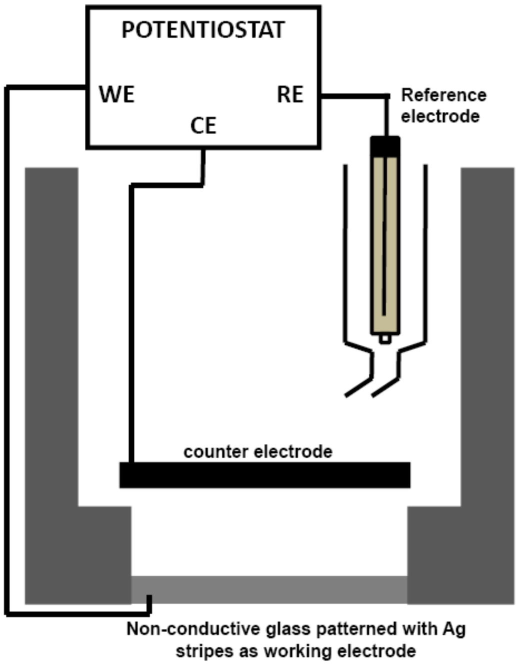

Figure 3.2 Illustration of the three electrode electrochemical cell.

Various electrolytes were used to understand the electroless reduction of Au^+ ions with electrochemically evolved hydrogen nanobubbles and are given in Table 3.1. Gold cyanide and self-prepared gold sulfite electrolytes were used to study the electrochemical behaviors of electrolytes. Self-prepared gold sulfite solution with the addition of stabilizer (EDA) was used to understand the stability of electrolytes. Nickel sulfamate tetrahydrate was used to investigate the effects of electrodeposited nickel metal on hydrogen evolution efficiency. The self-prepared solutions with other addition additives were prepared in the following orders:

Diluted 10 % $Na_3Au(SO_3)_2$ → EDA → 0.4 M of nickel sulfamate → 5% sulfuric acid.

Table 3.1 Summary of Gold Electrolytes

Additive Bath	EDA	Ni Sulfamate	Acidifier	pH
Gold Cyanide				~6.8
Self-Prepared Gold Sulfite			√	~6
Self-Prepared Gold Sulfite	√		√	~6
Self-Prepared Gold Sulfite		√	√	~6
Self-Prepared Gold Sulfite	√	√	√	~6
Self-Prepared Gold Sulfite			√	~6
Self-Prepared Gold Sulfite	√		√	~6

The optical microscope glass slide was rinsed with deionized water and then cleaned with plasma treatment before use. Glass was chosen as a substrate because of its extremely low conductivity. The photolithography technique was used to pattern the glass substrate. The design of photomask used in the experiments is shown in Figure 3.3 (a). The width of the stripes is 50 μm, and the stripes were duplicated every 100 μm. The Ag stripes patterned substrate is shown in Figure 3.3 (b).

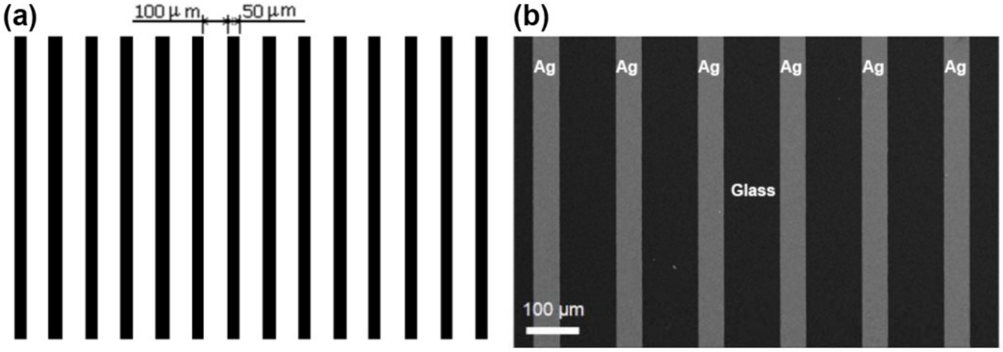

Figure 3.3 (a) Photomask pattern for photolithography; (b) Ag stripes patterned glass substrate.

3.2.2 Stability of Gold Electrolytes

For gold salt electrolytes, Au^+ ions can be combined with different complexes which are mainly classified into cyanide and non-cyanide complex. Gold cyanide complex $[Au(CN)_2]$ is one of the most important gold salt electrolytes for electrochemical deposition used in acidic, neutral or alkaline condition because of its high stability. However, there are several disadvantages of using $[Au(CN)_2]$ in acid, such as toxicity and disposal concerns. In addition, when the electrolyte is used under acid, the gold cyanide complex will decompose, leading to the formation of undissociated HCN. Thus many non-cyanide systems have been developed(72-74).

Non-cyanide baths could be operated in mild acid with stabilizing additives by either electrolytic or electroless mechanism. Sulfite bath is the commonly used complex for cyanide-free electrolyte, but the main problem with the sulfite system is its stability with gold complexes. For a homogenous reversible reaction, the law of mass -action dictates that

$$\frac{[\text{Au - complex}]}{[\text{Au}]\,[\text{complex}]} = \beta(\text{constant}) \qquad (3\text{-}2)$$

where [Au], [complex] and [Au-complex] are the concentration of Au^+ ion, complex ion and gold complex, respectively, in the solution. The constant, β, is a measurement of the strength of the complexant. Since the disproportionation of gold in solution is controlled by the concentration of gold complex, the stability constant for the complex is the determination of the bath stability. In the sulfite bath, gold ions presented in $[Au(SO_3)_2]^{3-}$ are suffered from instability at pH < 8. The stability constant of sulfite complex is approximately 10^{10} ,Equation 3-3, the magnitude of which is several orders smaller than that of cyanide complex which is roughly 10^{38} ,Equation 3-4(75, 76).

$$[Au^+] = \frac{[Au(SO_3)_2{}^{3-}]}{[SO_3{}^{2-}]^2} \times 10^{-10} \qquad (3\text{-}3)$$

$$[Au^+] = \frac{[Au(CN)_2{}^{-}]}{[CN_2{}^{-}]} \times 10^{-38} \qquad (3\text{-}4)$$

Discharge of the gold sulfite complex goes through the following steps(77).

$$Na_3Au(SO_3)_2 \rightarrow 3Na^+ + Au(SO_3)_2^{3-} \tag{3-5}$$

$$Au(SO_3)_2^{3-} \rightarrow Au^+ + 2SO_3^{2-} \tag{3-6}$$

Due to the low stability of gold sulfite complex, Au^+ ions cause the disproportionation reaction, Equation 3-7, when they are operated at $pH < 8$ (77-79).

$$3Au^+ \rightarrow 2Au^0 + Au^{3+} \tag{3-7}$$

Metallic Au^0 and Au^{3+} ions are formed in the solution which becomes turbid as a result of colloidal precipitation and finally decomposes. This spontaneous decomposition issue of the bath had been resolved by adding stabilizing additives to enhance the stability.

Several additives have been added to improve the stability of gold sulfite baths. H. Honma and co-workers(77, 79) have reported that gold sulfite bath can be operated at pH 8 using 2,2`-bipyridine as stabilizing additives. Morrissey(80) has also developed a gold sulfite bath which is stable at pH 4.0 to pH 6.5 using polyamines and aromatic nitro compounds as additives. These stabilizers have greatly improved the stability of the gold sulfite bath with the suppression of the disproportionation reaction of gold ions.

Other types of baths were demonstrated having higher stability without stabilizer. Ammonium sulfite baths have been developed which are operable in the pH range 6 - 8. The slightly acidic electrolytes containing tri-ammonium citrate, $KAuCl_4$ and Na_2SO_3 have been utilized as the stable gold solution. These electrolytes appear to be stable in the absence of stabilizing additives, and yet have not found wide use due to the low quality of gold(81, 82). The mixed ligand electrolyte, sulfite-thiosulfate baths, without additives have been demonstrated and characterized to be stable with a pH close to 7.0(78, 83-85). The formation of colloidal gold can be avoided by combining Au^+ ions with thiosulfate (stability constant = 10^{26}), and sulfite prevents the formation of sulfur by maintaining a high level of bisulfite (HSO_3^-) in the solution

(73, 85). However, the baths were found to be unstable at neutral or slightly acid condition due to the disproportionation of free thiosulfate ions in forming colloidal sulfur as shown in Equation 3-8, and that of sulfite ions in forming SO_2(74, 78, 85):

$$S_2O_3^{2-} \leftrightarrow S + SO_3^{2-} \tag{3-8}$$

The summary of gold electrodepostion electrolytes is given in Table 3.2.

Table 3.2 Summary of Gold Electrodepostion Electrolytes

Bath Type	Cyanide	Sulfite	Ammonium Sulfite	Sulfite-Thiosulfate
Stability	High	Low	Medium	Medium
Stabilizer	N/A	EDA	N/A	N/A
Stable at pH	6-10	5 - 8	6 - 8	Near Neutral
Toxicity	YES	NO	NO	NO

In our study, the stability of gold sulfite bath was improved by the chelating agent ethylenediamine (EDA), a sort of organic amine, working as the stabilizing additive. The ligand complexes of EDA with free Au^+ ions can suppress the disproportionation reaction. Therefore, EDA would be able to stabilize the electrolytes and enable operation of gold sulfite bath within pH range of 5 - 8(73, 79).

Cyclic voltammetry (CV) was carried out to study the electrochemical behaviors of gold electrolytes. The investigated electrolytes included self-prepared gold sulfite and gold cyanide. The CV measurements were recorded from open circuit potential toward the negative direction. Figure 3.4 shows the reduction potential of different electrolytes.

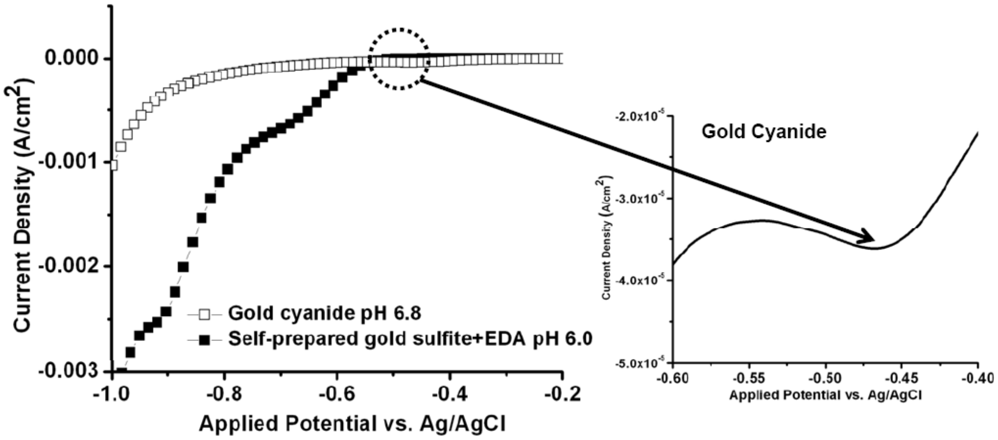

Figure 3.4 Cyclic voltammograms for self-prepared gold sulfite and gold cyanide from open circuit potential to -1.0 V (vs. Ag/AgCl) at scan rate 5 mV/s.

The CV measurements have shown that gold cyanide has extremely high stability compared to self-prepared gold sulfite. For gold cyanide, the reduction potential of Au^+ ions was observed at -0.45 V (vs. Ag/AgCl) with very stable low current density and the hydrogen evolution occurred at applied potential -0.9 V with current density -0.3 mA. For the self-prepared gold sulfite electrolyte, the reduction potential of Au^+ ions was observed at -0.68 V and the hydrogen evolution occurred at applied potential -0.78 V with current density -1.0 mA.

3.2.3 Effects of Ethylenediamine (EDA)

In this section, the effects of stabilizer EDA were investigated. To study the effects of EDA on the formation of hollow gold nanoparticles, self-prepared gold sulfite electrolytes were prepared with and without EDA. The potential was applied at -0.6 V (vs. Ag/AgCl). As shown in Figure 3.5 (a), no well-defined gold nanoparticles were observed on both conductive and non-conductive areas with the absence of EDA. However, small number of gold particles appeared on the non-conductive area that might be due to the disproportionation reaction at a pH < 8. In order to clear out the questions, the bare silicon wafer was immersed into gold sulfite electrolyte with the same pH condition. As expected, gold particles were precipitated out and observed on silicon wafer.

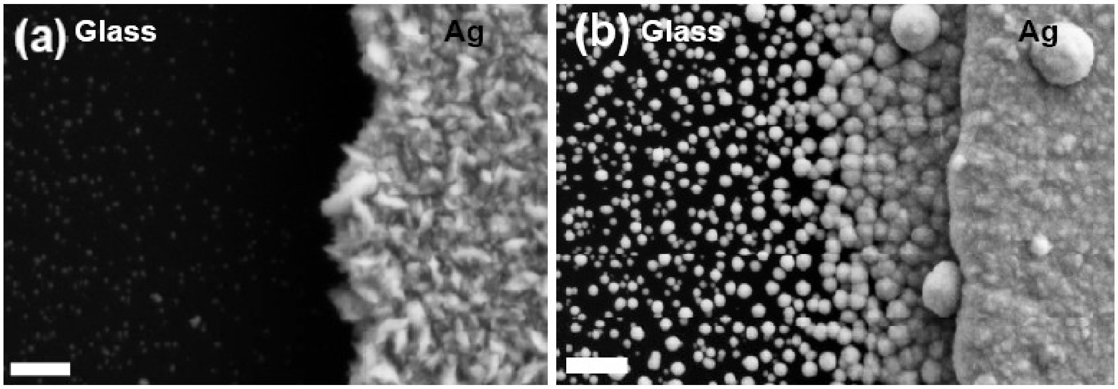

Figure 3.5 SEM micrographs of gold nanoparticles from self-prepared gold sulfite electrolytes; (a) in the absence of EDA; (b) in the presence of EDA, on patterned substrates with an applied potential -0.6 V (vs. Ag/AgCl). The scale bars are 1 μm.

For the gold sulfite electrolyte with EDA, as show in Figure 3.5 (b), well-defined gold nanoparticles were observed on the non-conductive areas. The above observations suggest that EDA plays an important role in the stability of the gold sulfite electrolytes. The complexes of EDA bond with free Au^+ ions to suppress the disproportionation reaction. Therefore, the gold sulfite electrolytes are able to be used with a lower range of pH.

CV was conducted to study the effects of EDA on the gold sulfite electrolytes. The reduction potential of the gold sulfite electrolytes with and without EDA was recorded from open circuit potential to -1.0 V (vs. Ag/AgCl) at the scan rate 5 mV/s. The acidifier, sulfuric acid, is not believed to be a significant issue in these experiments. As shown in Figure 3.6, with the addition of EDA, the current density of hydrogen evolution was increased from -2.8 mA to -5.1 mA at applied potential -0.95 V. The addition of EDA greatly enhanced hydrogen evolution efficiency. A possible explanation for this enhancement is that EDA has the same function as ethylenediamine tetra acetic acid (EDTA) which has the capability to clean and remove the adhering surface oxides from active metal electrodes for hydrogen evolution (the Rowland effect)(86-88). EDA, a key additive, was not only able to increase the stability of the gold sulfite electrolytes but also increase hydrogen evolution efficiency.

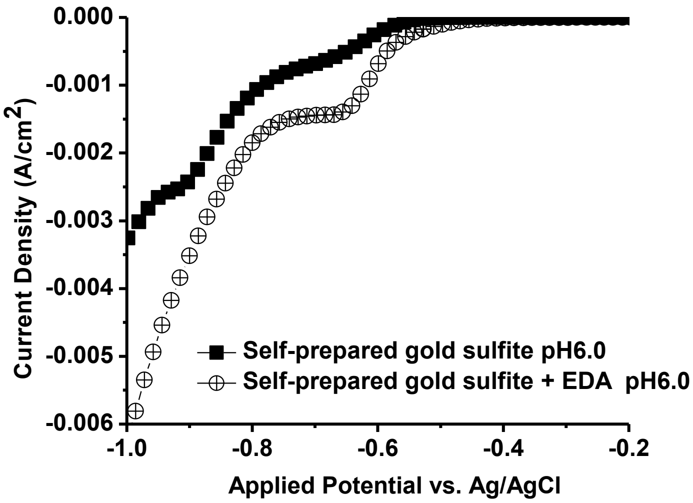

Figure 3.6 Cyclic voltammetry of self-prepared gold sulfite electrolytes without and with EDA were recorded starting from open circuit potential to -1.0 V (vs. Ag/AgCl) at scan rate 5 mV/s.

3.2.4 Effects of Applied Potential

When the applied potential is more negative than -0.6 V (vs. Ag/AgCl), a large number of gold nanoparticles were formed on the non-conductive areas as shown in Figure 3.7 (b). However, when the applied potential is more positive than -0.6 V only electrodeposited gold thin film on Ag stripes, and no gold nanoparticles were observed on the non-conductive areas as shown in Figure 3.7 (a). According to the Nernst equation, the hydrogen evolution occurred at hydrogen equilibrium potential -0.55 V (vs. Ag/AgCl) with a pH=6 at room temperature. In the electrochemistry process, elements can only be electrodeposited on conductive surfaces which means electrodeposited gold nanoparticles cannot be occurred on non-conductive areas. The only possible explanation for the formation of gold nanoparticles on the non-conductive areas is through the electroless reaction. Electroless-deposited gold nanoparticles have only been observed when the applied potential is more negative than the equilibrium potential of hydrogen evolution. This strongly suggests that hydrogen evolution is involved in the formation of gold nanoparticles on non-conductive areas.

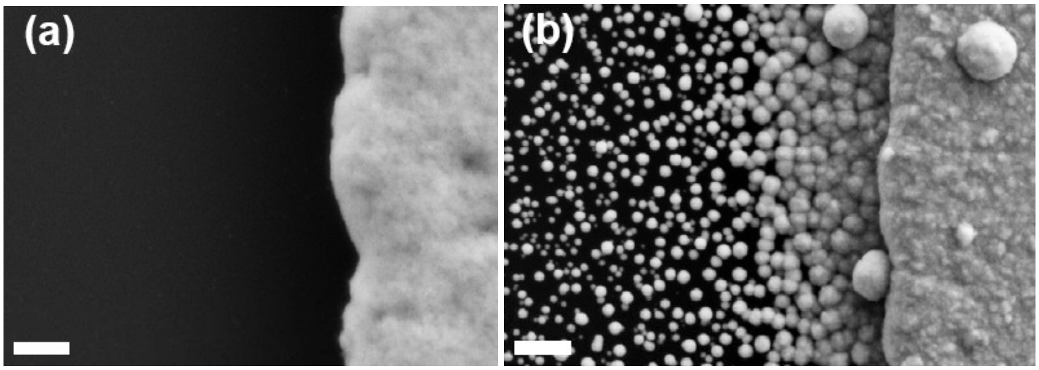

Figure 3.7 SEM micrographs of formation of gold nanoparticles on non-conductive substrates patterned with periodical Ag strips at applied potential: (a) -0.5 V; (b) -0.6 V (vs. Ag/AgCl). The scale bars are 1 μm.

In order to exclude the possibility of the formation of gold nanoparticles from the edge of the metal stripes, two electrolytes were used, gold sulfite and gold cyanide. As shown in Figure 3.8, with gold sulfite electrolyte, gold nanoparticles were observed on the non-conductive areas. However, with gold cyanide electrolytes, no gold nanoparticles were observed on the non-conductive areas, but only electrodeposited gold thin film on the Ag stripes.

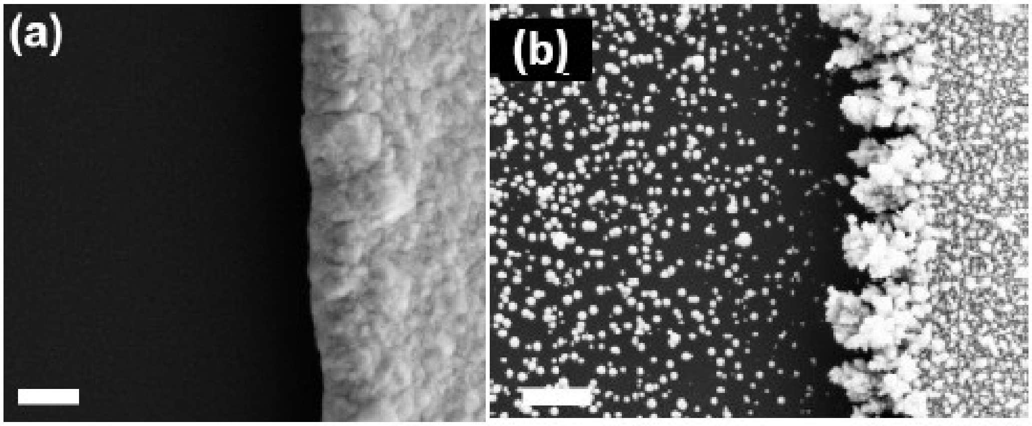

Figure 3.8 SEM micrographs of gold nanoparticles formation from: (a) gold cyanide electrolytes; (b) gold sulfite electrolytes on Ag stripes patterned substrates with an applied potential -0.8 V (vs. Ag/AgCl). The scale bars are 1 μm.

According to the standard reduction potential in Table 3.3(89), the hydrogen molecules have the capability to reduce Au^+ ions to become metallic Au^0 through the electroless deposition reaction. The overall reaction:

$$H_{2\,(g)} + 2Au^+_{(aq)} \rightarrow 2Au^0_{(S)} + 2H^+_{(aq)} \qquad (3\text{-}8)$$

Table 3.3 Standard reduction potential of various metals(89)

Metal/Metal Ion Couple	Electrode Reaction	Standard Value (V)
Au/Au^+	$Au^+ + e^- \leftrightarrow Au$	1.692
Au/Au^{3+}	$Au^{3+} + 3e^- \leftrightarrow Au$	1.498
Ag/Ag^+	$Ag^+ + e^- \leftrightarrow Ag$	0.779
Pd/Pd^{2+}	$Pd^{2+} + 2e^- \leftrightarrow Pd$	0.951
Cu/Cu^+	$Cu^+ + e^- \leftrightarrow Cu$	0.521
H_2/H^+	$2H^+ + 2e^- \leftrightarrow H_2$	0
Ni/Ni^+	$Ni^+ + e^- \leftrightarrow Ni$	-0.257

Electroless deposition is the spontaneous reduction and oxidation of metal ions in an aqueous solution form metallic particles or films in the absence of an external source of electric current(72, 90, 91). The literature commonly classifies "electroless deposition" into three fundamentally different mechanisms as shown in Figure 3.9(78, 92). These include autocatalytic, substrate catalyzed, and galvanic displacement processes.

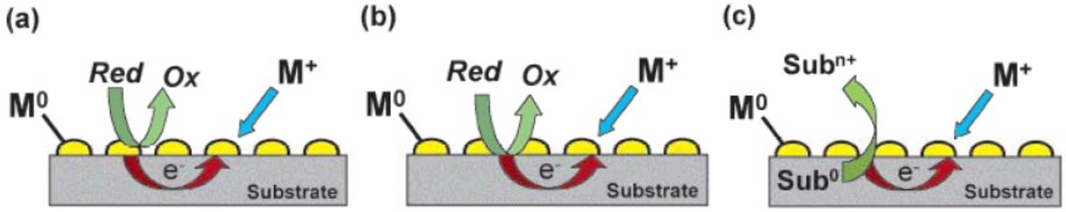

Figure 3.9 Electroless deposition processes: (a) autocatalytic: the reduced noble metal serves as the catalyst for further reduction of the metal salt by the external reducing agent; (b) substrate catalyzed: the substrate surface catalyzes the reduction of the metal salt by the reducing agent; (c) Galvanic displacement: the surface serves as the reducing agent and electron source for reduction of the metal salt(92).

Autocatalytic process uses a complex electrolyte composition to allow the reduced metal itself to serve as a catalyst for further reductive deposition. Once initiated, the reduced metal species serve to catalyze subsequent metal reduction. In autocatalytic system, the electrolytes typically contain a metal salt, a pH adjuster, a reducing agent, and other various additives. Similarly, substrate catalyzed deposition baths also contain a metal salt and reducing agent, but metal reduction is facilitated on the substrate surface. Once the surface is completely covered, metal ions cease to be reduced from solutions because the surface is no longer exposed(72, 93). In the case of galvanic displacement, the deposition is carried out in the absence of an external reducing agent(78) because the reducing electrons are provided by the substrate itself. The reducing electrons are derived from the valence band or bonding electrons of the solid and reduce metal ions in solution to metallic particles on the surface(94). The galvanic displacement mechanism can be applied to describe the electroless reaction of Au^+ ions with hydrogen molecules. In this case, the hydrogen molecules were served as reducing electrons provider for the formation of gold nanoparticles.

3.2.5 Effects of Addition of Ni^{2+} Ions

We have found that the addition of Ni^{2+} ions into the electrolyte greatly affect the formation of gold nanoparticles. The hydrogen evolution efficiency is directly associated with hydrogen exchange current density of metal electrodes. It is known that nickel metal has a relatively high current density in hydrogen evolution reaction.

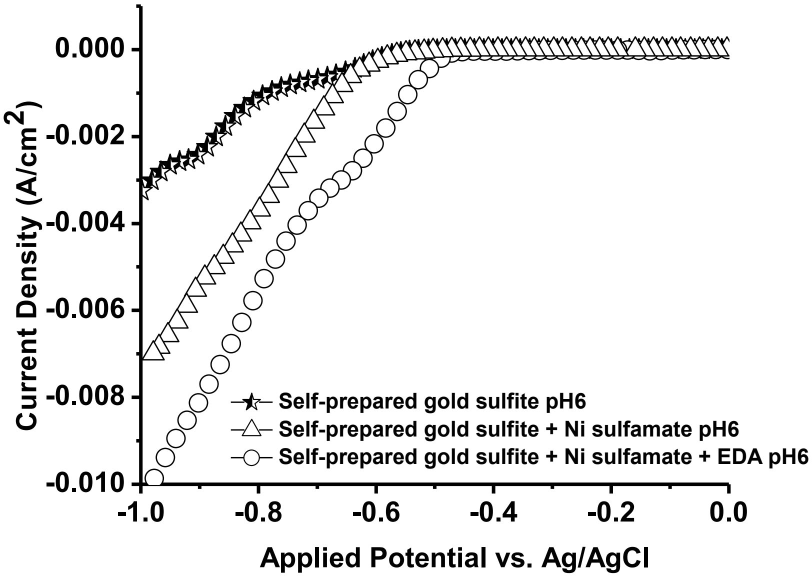

Figure 3.10 Cyclic voltammetry of self-prepared gold sulfite electrolytes in the presence of Ni^{2+} ions with and without EDA were recorded starting from open circuit potential to -1.0 V (vs. Ag/AgCl) at scan rate 5mV/s.

First, the hydrogen evolution efficiency was studied in the self-prepared gold sulfite electrolyte with and without Ni^{2+} ions by CV measurement. CV measurement in Figure 3.10 shows that the addition of Ni^{2+} ions and EDA greatly increased the total current density. As reported literature by Vogt(95), the current efficiency of the hydrogen generation is a directly relative to the total current density. With Ni^{2+} ions, nickel metal was electrodeposited and replaced the electrode surface during the electrodeposition. The newly electrodeposited nickel metal has higher hydrogen exchange current density(96, 97). Moreover, the addition of EDA can increase the hydrogen evolution efficiency as well. The current density of hydrogen evolution reaction at applied potential -0.95 V (vs. Ag/AgCl) was increased from -2.8 mA to -6.5 mA with the addition of Ni^{2+} ions and -9.2 mA in the presence of both Ni^{2+} ions and EDA.

The effects of electrodeposited nickel metal on the formation of gold nanoparticles were again investigated on non-conductive glass substrates patterned with Ag stripes. Figure 3.11 shows gold nanoparticles formed from the gold sulfite electrolytes in the absence and presence of electrodeposited nickel metal. It can be been that the size distribution of gold nanoparticles was greatly improved by the addition of Ni^{2+} ions.

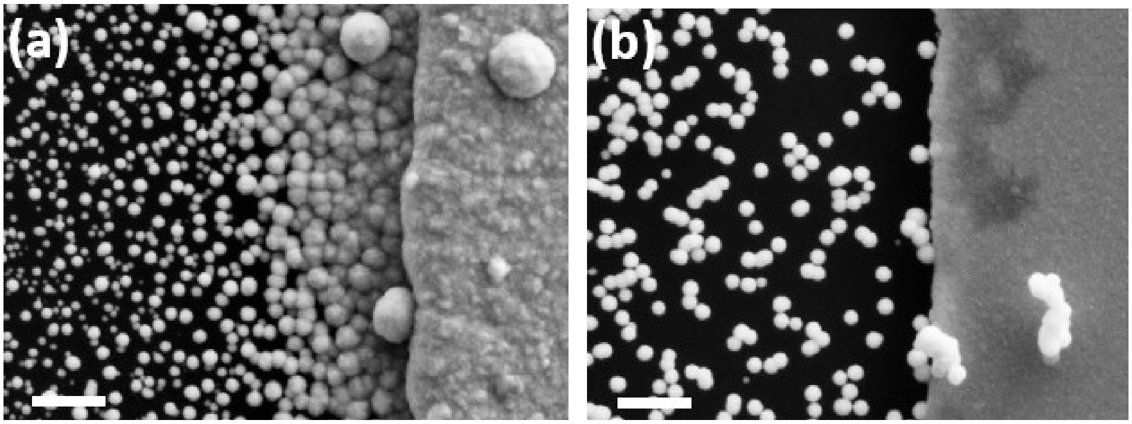

Figure 3.11 SEM micrographs of gold nanoparticles formation using self-prepared gold sulfite electrolytes with EDA: (a) in the absence of Ni^{2+} ions; (b) in the presence of Ni^{2+} ions with an applied potential -0.8 V (vs. Ag/AgCl) on non-conductive substrates patterned with Ag stripes. The scale bars are 1 μm.

The effects of electrodeposited nickel metal on the formation of gold nanoparticles were also observed on plain conductive substrates. Figure 3.12 shows the electrochemically deposited gold from the gold sulfite electrolytes with the absence and presence of Ni^{2+} ions. Without Ni^{2+} ions, the deposited metallic Au was very rough and with no well-defined particles. With Ni^{2+} ions, a large number of spherical particles were observed. Some parts of the spherical particles peeled off from the substrate to expose their interior. It clearly shows the hollow nature of these gold nanoparticles, which suggests that hydrogen nanobubbles act as templates for the formation of gold nanoparticles.

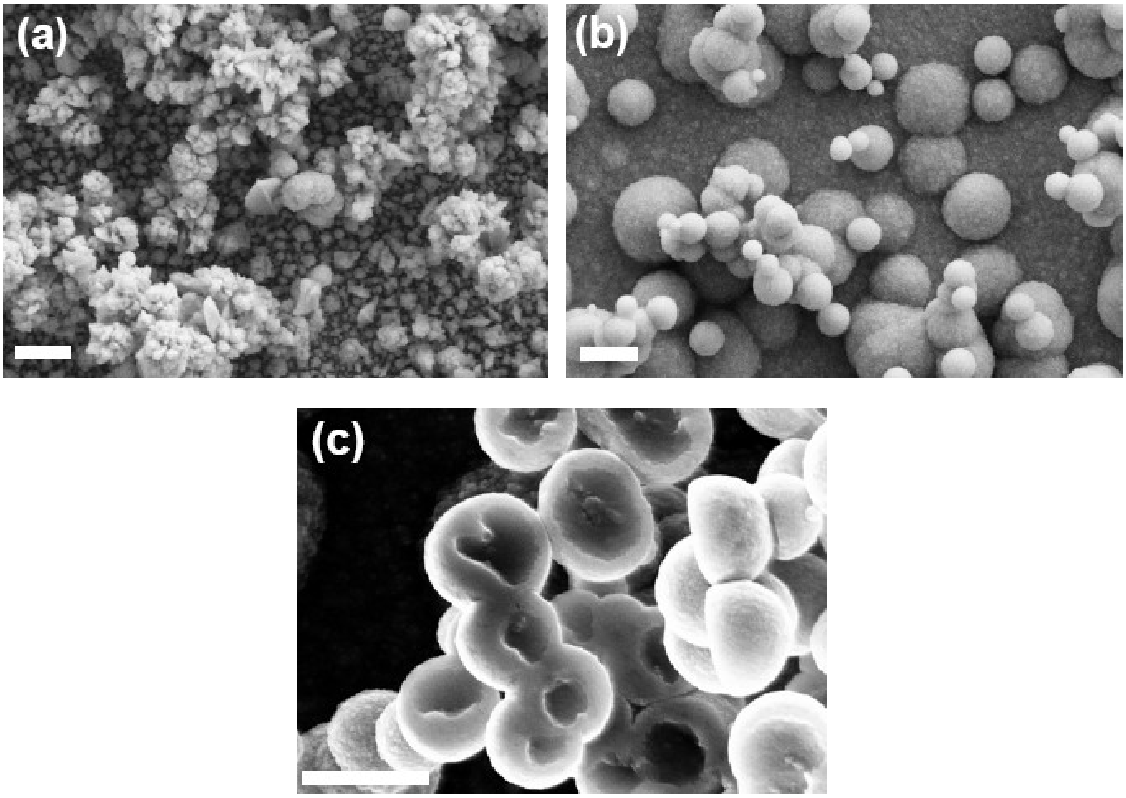

Figure 3.12 SEM micrographs of gold nanoparticles formation from self-prepared gold sulfite electrolytes: (a) in the absence of Ni^{2+} ions; (b) in the presence of Ni^{2+} ions at applied potential -0.8 V (vs. Ag/AgCl) on conductive substrates. (c) SEM micrographs show bowl-shape gold nanoparticles peeled from the deposited thin film. The scale bars are 1 μm.

Hydrogen evolution includes several atomic processes. Protons from solution combine with electrons to form hydrogen atoms which are chemisorbed at the electrode surfaces and form H_2 molecules. H_2 molecules dissolve in the electrolyte and become supersaturated in the solution close to the electrode, from which H_2 bubbles nucleate on the electrode surface. The ability of a metal to catalyze the hydrogen evolution reaction is usually measured by the exchange current density, which is the rate of hydrogen evolution at equilibrium per surface area at a certain electrode potential. The exchange current density of Ni metal is relatively high, only lower than Pt group metals and much higher than Ag and Au(98). With the addition of Ni^{2+} ions in the electrolyte, electroplated nickel metal replaced the electrode surface during the electrodeposition, which greatly increases the formation rate of H_2 molecules, and therefore, the solution quickly reaches a high supersaturation state and the nanoscale nuclei of hydrogen bubbles rapidly cover the electrode surface.

The narrow size distribution of the void in the gold nanoparticles suggests that the electroless deposition occurs immediately after a stable bubble has formed and prevents its growth. There are two possible Au formation mechanisms. First, a high concentration of molecular hydrogen may be able to reduce the Au^+ ions into metallic Au to form Au clusters, then the Au clusters act as catalyst to trigger the disproportionation reaction and more metallic Au forms. Another possibility is that the hydrogen bubbles act as catalytic supports, just like metallic Au, for the disproportionation reaction to take place.

However, the existence of nanobubbles has not been unequivocally established. Nanobubbles would be dissolved and disappeared rapidly due to the high internal pressure associated with the interfacial curvature. Ljunggren and co-workers have reported the calculation of the lifetime of a bubble as a function of its size(99), for instance, H_2 nanobubble with a radius of 25 nm will be dissolved rapidly into water within 5 μs. Thus it is still not fully understood why these nanobubbles can remain stable for several hours. However, the possible existence of nanobubbles at interface between hydrophobic solids and water has been reported (100-109). In the heterogeneous nucleation mechanism, gas molecules may first nucleate at the solid surface. And then the diffusion of dissolved gas molecules from bulk solution would then enhance bubble formation. The existence of nanobubbles at the solid-liquid interface has been detected by various techniques. In most experiments, atomic force microscopy (AFM) in tapping mode is used to detect the nanobubbles(110). In high-resolution tapping-mode atomic force microscopy (TMAFM), an oscillating tip is brought to be intermittently in contact with the sample surface by applying a lighter force compared with that applied in contact mode AFM. Thus, the technique is commonly used to detect nanobubbles. Zhang and co-workers presented the electrochemically controlled formation of hydrogen nanobubbles on bare highly oriented pyrolytic graphite (HOPG) with a hydrophobic surface via AFM as shown in Figure 3.13. The formation and growth of hydrogen nanobubbles could be controlled by tuning either the applied potential or the reaction time. The evolution process of hydrogen nanobubbles can be described as formation, growth, coalescence, as well as the eventual release of merged microbubbles from the HOPG (110). This evolution process is very similar to our nanobubble speculation. But ours is very different, first, the shape of the nanobubbles and second, the substrate we used is hydrophilic. Therefore, the hydrogen evolution process is still remaining unknown.

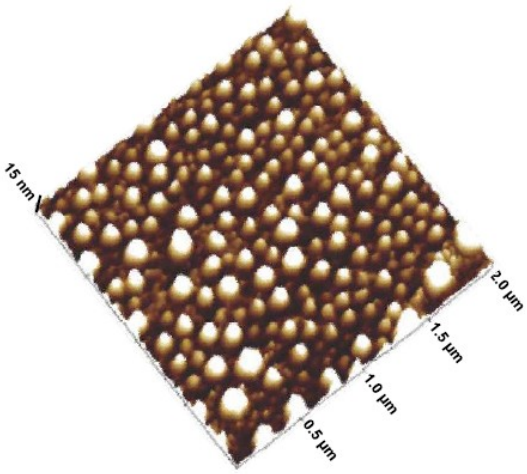

Figure 3.13 Electrochemical generated hydrogen nanobubbles detected by AFM(110).

3.3 Reduction of Au^+ Ions by Hydrogen Bubbles

The assumption that electrochemically evolved hydrogen bubbles can serve as both templates and reducing agents has been confirmed by direct observation of gold metal formed around electrochemically evolved hydrogen bubbles. This reduction reaction was directly observed in an experiment where an Au-coated silicon wafer was used as the working electrode. When a high negative potential -0.9 V (vs. Ag/AgCl) is applied, hydrogen bubble depart from the working electrode surface and could be seen rising upward to the electrolyte surface. Pieces of metal debris which floated on the electrolyte surface were collected for analysis. Scanning electron micrographs and energy dispersive spectrometer (EDS) confirmed that the debris is comprised of bowl-shaped gold nanoparticles, indicating that metallic gold indeed was reduced at the bubble boundary as shown in Figure 3.14.

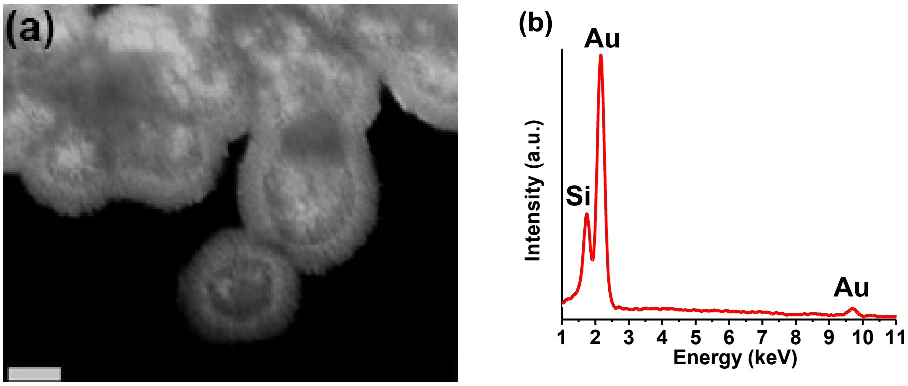

Figure 3.14 (a) SEM micrograph shown the bowl-shape gold nanoparticles collected from the electrolyte surface. The electrodeposition was conducted at applied potential -0.9 V (vs. Ag/AgCl) with a modified commercial gold sulfite electrolyte with a pH ~ 6.0. Au-coated silicon wafer served as the working electrode. The scale bar is 100 nm. (b) Energy dispersive spectrometer data of bowl –shape gold nanoparticles.

We also tried to generate hydrogen gas bubbles by directly pumping pure hydrogen gas into the electrolyte solution. Figure 3.15 illustrates this process. However, even with the same electrolyte condition as electrochemically generated hydrogen nanobubbles, no reaction was observed on the boundary of these hydrogen gas bubbles. The possible reason could be that the hydrogen molecule concentration of hydrogen gas bubbles is different from the electrochemically evolved hydrogen nanobubbles. We performed the calculations to estimate the pressure inside these two cases. The inside pressure of a bubble was calculated using Newton's second law of motion:

$$-2\gamma(2\pi R) + p_i(\pi R^2) = 0 \tag{3-9}$$

where γ is the surface tension of water (0.073 N/m at 20°C), R is the radius of the bubble and P_i

is the pressure inside the bubble.

The first left hand term is the force due to surface tension of water and the second left hand term is the force due to the pressure inside bubble. Solving above equation for the pressure inside the bubble gives $P_i=4\gamma/R$. In general, the pressure P_0 outside the bubble is not zero. However, this result still gives the difference between the inside and outside pressures $\Delta P = 4\gamma/R$. Based on the above equation, we estimated the pressure difference ΔP for the electrochemically generated hydrogen nanobubble is about 1.2×10^7 N/m^2 with a radius of 25 nm, and the pumped hydrogen gas is about 292 N/m^2 with a radius of 1 mm. According to the estimation, we can know that the hydrogen molecular concentration inside the electrochemically evolved nanobubbles can be many magnitudes larger than the pumping approach.

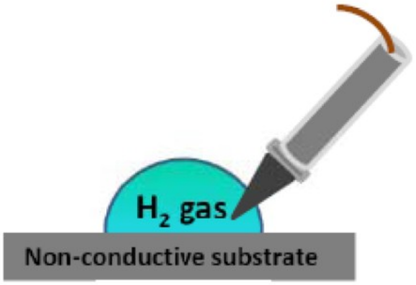

Figure 3.15 Illustration of pumping hydrogen gas bubbles in the gold sulfite electrolyte without external electric current.

3.4 Observation of Gold Nanoparticle Formation on TEM Grid

Gold nanoparticles were directly generated on TEM grid which provided a convenient way for analyzing the structure of gold nanoparticles. The hollow nature of gold nanoparticles was revealed by high-resolution transmission electron microscopy (HRTEM).

TEM grid illustrates in Figure 3.16 (a), consists of copper meshes with a heavy layer of carbon film. They were directly used as working electrode. Figure 3.16 (b) shows that a large number of gold nanoparticles were formed on carbon film after electrodeposition. This suggests that electrochemically evolved hydrogen nanobubbles were trapped on the carbon film, which reduced the Au^+ ions into gold nanoparticles.

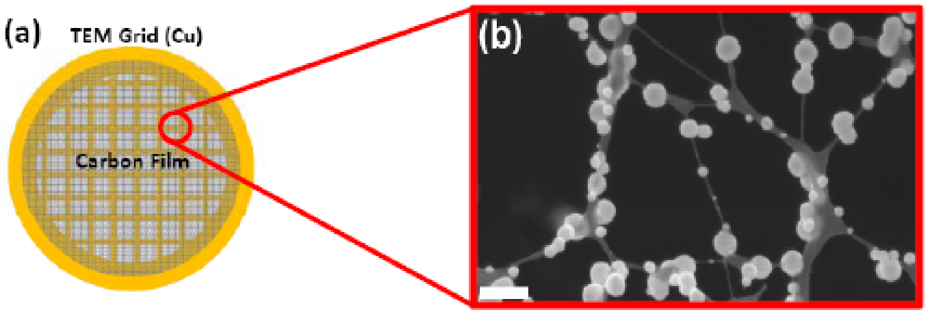

Figure 3.16 (a) Illustration of TEM grid consists of copper meshes and carbon film; (b) SEM micrographs of gold nanoparticles on carbon film. The scale bar is 1 μm.

The HRTEM micrographs were taken after the electrodeposition without any further treatment. Figure 3.17 (a) clearly indicates the hollow feature of gold nanoparticles, showing the hollow core with the radius of 25 nm. This hollow feature again suggests that hydrogen nanobubbles acted as templates for the formation of gold nanoparticles. Unexpectedly, we also found that some of the gold nanoparticles with a multilayer structure as shown in Figure 3.17 (b). The possible route for the formation of these nanostructures can be explained as following. After gold metal forms in the surrounding of a hydrogen nanobubble, a larger nanobubble grows on the same or a nearby site and engulfs the already-formed gold nanoparticle. Then again, gold metal forms on the surface of the larger nanobubble. This shell formation may able to be repeated many cycles.

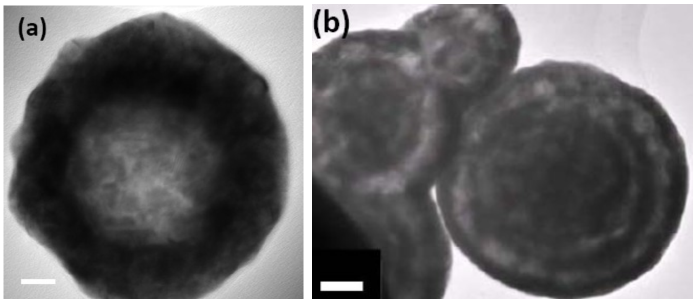

Figure 3.17 TEM micrographs of (a) single layer gold nanoparticle, and (b) multiple-shell gold nanoparticles. The scale bar (a) is 10 nm (b) is 50 nm.

CHAPTER 4

MASSIVE PRODUCTION OF HOLLOW GOLD NANOPARTICLES USING ALUMINA MEMBRANE

4.1 Introduction

In this chapter, the alumina membranes were used as substrates to capture the electrochemically evolved hydrogen nanobubbles, and subsequently to generate a large number of hollow gold nanoparticles through the electroless reaction with sodium gold sulfite electrolyte. The formation mechanism of hydrogen nanobubbles inside the alumina membrane has been studied. The effects of the addition of Ni^{2+} ions on the morphology of hollow gold nanoparticles were observed. Moreover, the effects of applied potential and deposition time on the formation of hollow gold nanoparticles were also discussed.

As described in chapter 3, the Ag stripes have been used as substrates to demonstrate the effect of the electrochemically evolved hydrogen nanobubbles on the formation of hollow gold nanoparticles. However, there are several disadvantages with using Ag stripes patterned glass slide as substrate to produce hollow gold nanoparticles. First, the electroless deposited hollow gold nanoparticles are easy to coalesce with each other and end up with relative bigger particles. Second, it is difficult to release the hollow gold nanoparticles from the substrate surface. Therefore, the alumina membrane was chosen as the medium to capture these electrochemically evolved hydrogen nanobubbles, and subsequently to generate hollow gold nanoparticles in large numbers. Alumina membrane consists of ~200 nm pores and the pore density of membrane is about 10^9 /cm^2 and the channel length is about 60 μm. The alumina membrane provided a large surface area for the formation of hydrogen nanobubbles on the

4.2 Synthesis of Hollow Gold Nanoparticles

The electrodeposition experiments were conducted potentiostatically using a typical three-electrode cell with a Ag/AgCl electrode in 3 M NaCl solution as the reference and a platinum mesh as the counter electrode. Potentials were applied to the working electrode using a Princeton Applied Research 273A Potentiostat/Galvanostat as illustrated in Figure 4.1.

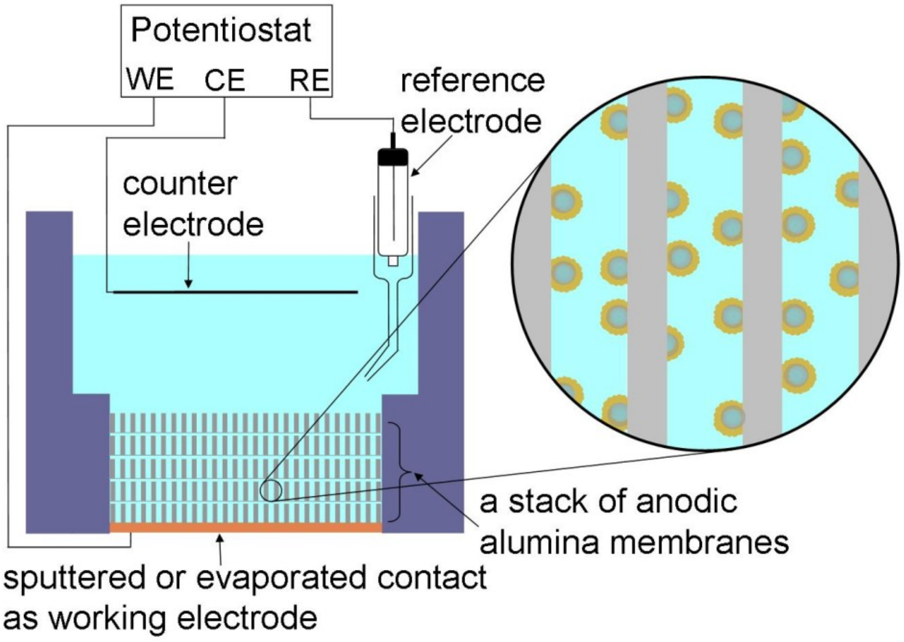

Figure 4.1 Illustration of the three electrode electrochemical cell. A stack of alumina membrane membranes was used. A 500 nm Cu layer was sputter-deposited on the bottom side of the bottom membrane and served as the working electrode.

Commercial filter alumina membranes from Whatman Corp. were used. They are 60 µm thick. The channels go through the entire thickness with small segment of branches on one end. The channel diameter is about 300 nm and the diameter of branches can vary from 20 nm to 200 nm. The one side of the membrane was sputter-deposited with 500 nm Cu layer that served as the working electrode (the bottom membrane). Two to five membranes were simply stacked together with their branched side facing towards the previous membrane. A Teflon cell with an o-ring 1 cm diameter as placed on the top of the membrane stack. By this approach, the electroless reaction was easily separated from the electrodeposition process, and hollow gold nanoparticles were collected from the top membranes.

The electrolyte used is the same as the Ni^{2+} ions containing electrolyte discussed in chapter 3. Briefly, the pH of the solution was about 7.0 and the solution composed of: ~3% sulfuric acid (for adjusting pH), ~3% ethylenediamine (EDA), ~10% sodium gold sulfite $Na_3Au(SO_3)_2$ and ~7% sodium sulfite (Na_2SO_3). The solution was altered by adding 0.01 M sulfuric acid (H_2SO_4) or 0.4 M nickel sulfamate tetrahydrate ($Ni(SO_3NH_2)_2 \cdot 4H_2O$) solution to change the pH to ~6.0.

Electrodeposition experiments were carried out in applied potentials more negative than -0.6 V (vs. Ag/AgCl), the inner pore wall surfaces in all membranes were filled with distinct and well defined gold nanoparticles. The number of these nanoparticles gradually decreases with the distance from the bottom electrode. Figures 4.2 (a) and (b) show the scanning electron micrographs of these nanoparticles as formed within the pores of the second and bottom membrane, respectively.

Following electrodeposition, the nanoparticles were released into water by pouring out the electrolyte from the entire cell and washing using deionized water. Then, deionized water was kept in the cell for at least half hour to allow complete diffusion of the electrolyte out of the membranes. This process was repeated for at least three times. Membranes in the stack were individually dissolved using 1 M sodium hydroxide (NaOH) solution. The particles were cleaned by several cycles of dispersion in deionized water followed by centrifugation. Figure 4.3 shows accumulation of gold nanoparticles on top of the electrodeposited metal on the working electrode after dissolving the first membrane by using 1 M NaOH solution.

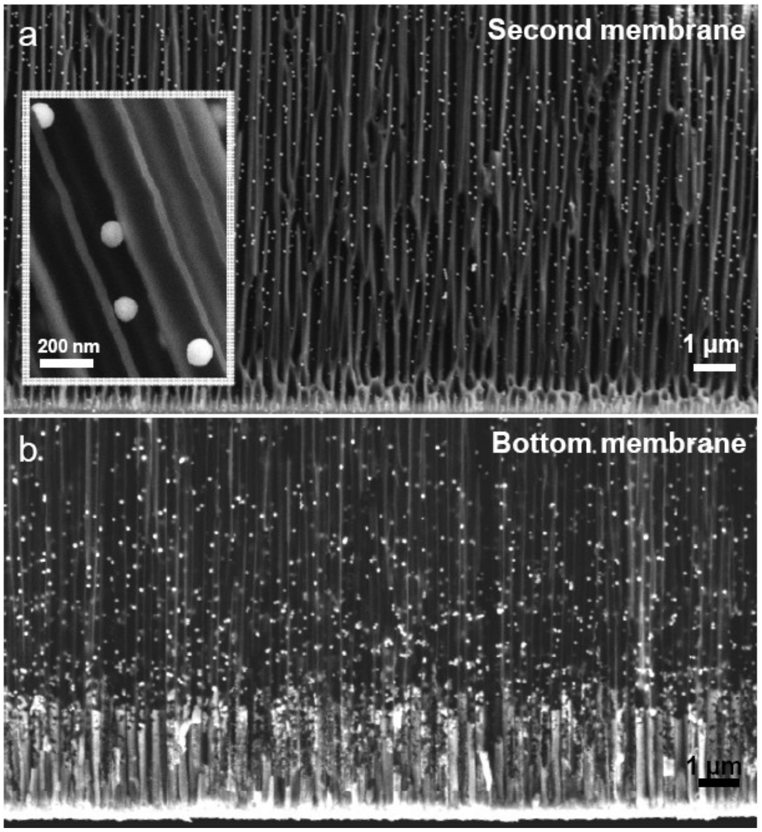

Figure 4.2 SEM micrographs of gold nanoparticles formed inside the channels of alumina membranes.

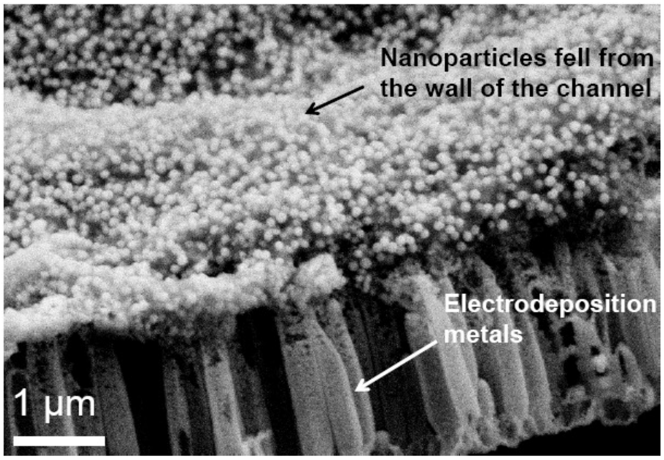

Figure 4.3 SEM micrograph taken after dissolving the first membrane showing a large number of particles on top of the electrodeposited metal on the working electrode.

4.3 Structure Characterization

After the membrane was dissolved by using 1 M NaOH solution, hollow gold nanoparticles were released into deionized water. The size of the cavity and the completed nanoshells were determined using both scanning electron microscopy (SEM) and transmission electron microscopy (TEM).

4.3.1 Characterization of Hollow Gold Nanoparticles by TEM

The bright field images and selective area electron diffraction were acquired using a Hitachi H9500 HR-TEM operating at 300 kV. Samples were prepared by placing a drop of gold suspension on a carbon coated copper grid, waiting 10 minutes for the particles to settle on the grid, and then removing excess solution. Figure 4.4 shows the TEM micrographs and the selected area diffraction pattern of nanospheres. It clearly shows these nanospheres have hollow interiors, and the shell consists of polycrystalline gold with a grain size of about 5 nm.

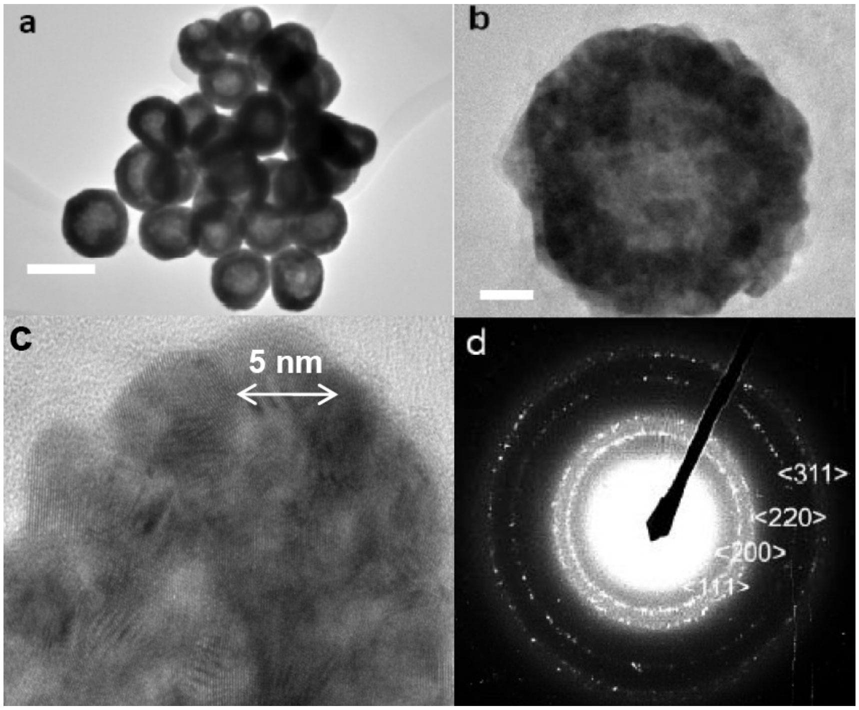

Figure 4.4 Hollow gold nanoparticles. (a) -(c) are TEM micrographs of nanospheres, and (d) is the selected area diffraction pattern. The scale bar in (a) is 100 nm and (b) is 20 nm.

4.3.2 Characterization of Hollow Gold Nanoparticles by SEM

Ion milling was used to open the hollow gold nanoparticles for SEM to reveal their interior. SEM micrographs were taken in a ZEISS Supra 55 VP SEM. Samples were prepared by spreading diluted hollow nanosphere water suspension on a piece of silicon wafer, a monolayer of these spheres was formed on the surface. Ion milling was performed using a Gatan Precision Ion Polishing System with 4.5 keV ion guns tilted at 4 degrees for 5 minutes. The two beam currents were 36 uA and 48 uA, and the sample rotated at 4 rpm. The results are shown in Figure 4.5. It clearly shows the hollow cores in each particle.

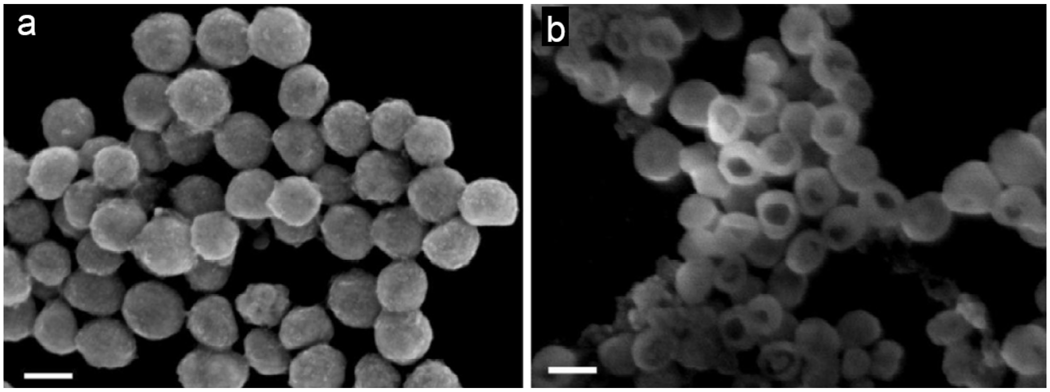

Figure 4.5 SEM micrographs of nanospheres before (a) and after (b) ion milling. The hollow interior of the particles is clearly shown. The scale bars are 100 nm.

4.3.3 Size Distribution of Hollow Gold Nanoparticles

The narrow size distribution can be achieved by using this method. Figure 4.6 (a) is the result of dynamic light scattering (DLS) measurement for hollow gold nanoparticles, clear indicating the monodisperity of nanoparticles, which was confirmed with SEM micrograph shown in Figure 4.6 (b).

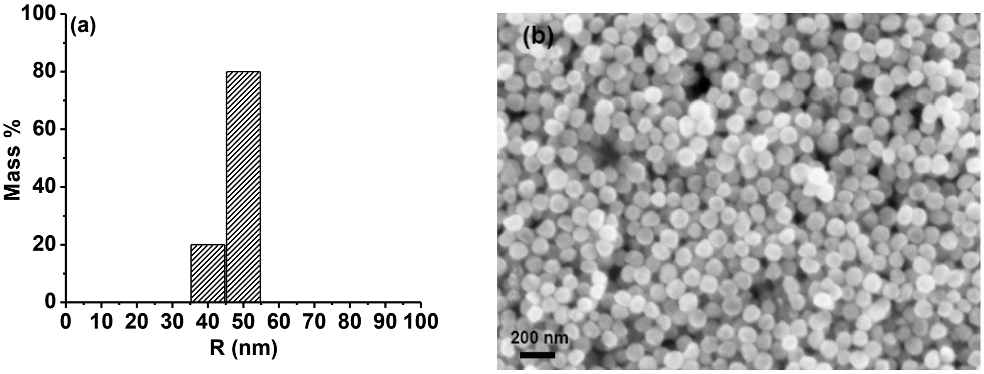

Figure 4.6 The size distribution of hollow gold nanoparticles (a) The dynamic light scattering (DLS) measurement. (b) SEM micrograph showing the narrow size distribution of hollow gold nanoparticles

4.4 Formation of Hydrogen Nanobubbles inside Alumina Membrane

Hydrogen bubble nucleation always requires certain supersaturation level of hydrogen molecules. When the overpotential is applied, the hydrogen molecules start to generate from the working electrolyte. The channels inside alumina membrane confine the hydrogen molecules in a small volume. After certain time, the hydrogen molecules in the electrolyte reached the supersaturated condition. The channel walls provide favorable nucleation sites for hydrogen nanobubbles. Thus, the nanobubbles form on the wall of the pore from the H_2 supersaturation solution. This hypothesis is indirectly supported by two evidences. First, a larger number of gold nanoparticles formed on the bottom membrane and they gradually decreased as away from the bottom electrode as shown in Figure 4.7.

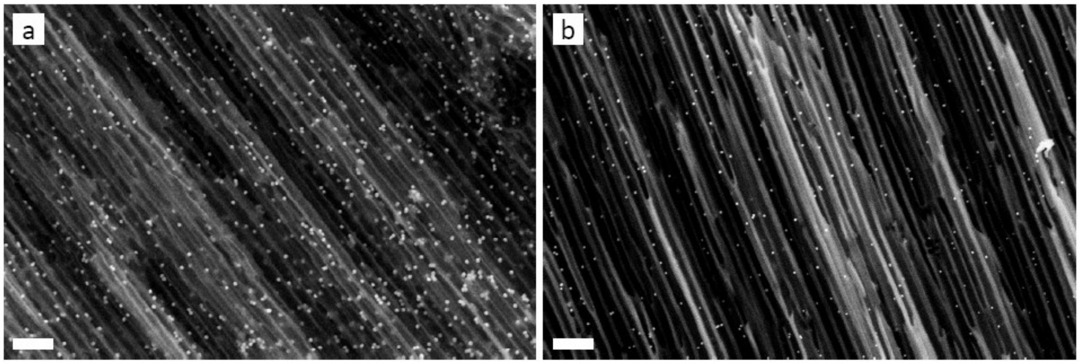

Figure 4.7 SEM micrographs of the bottom membrane after electrodeposition. The number of gold nanoparticles gradually decreased with a distance away from the bottom electrode. (a) shown the site close to the bottom electrode, and (b) shown the site far away from the bottom electrode. The scale bars are 1 μm.

Second, the channels in one side of the alumina membrane are branched and the size of the branched paths is about 20 nm in diameter as shown in Figure 4.8. The branched side of the second membrane was faced down to contact with the bottom membrane. TEM micrograph in Figure 4.4 (b) clearly shows the diameter of the hollow interior is about 50 nm. This hollow interior directly implies the size of the hydrogen nanobubble. It would have been impossible for 50 nm hydrogen nanobubbles to pass 20 nm narrow paths and travel upward into the second membrane. The hydrogen nanobubbles formed on the channel wall were from a supersaturated solution.

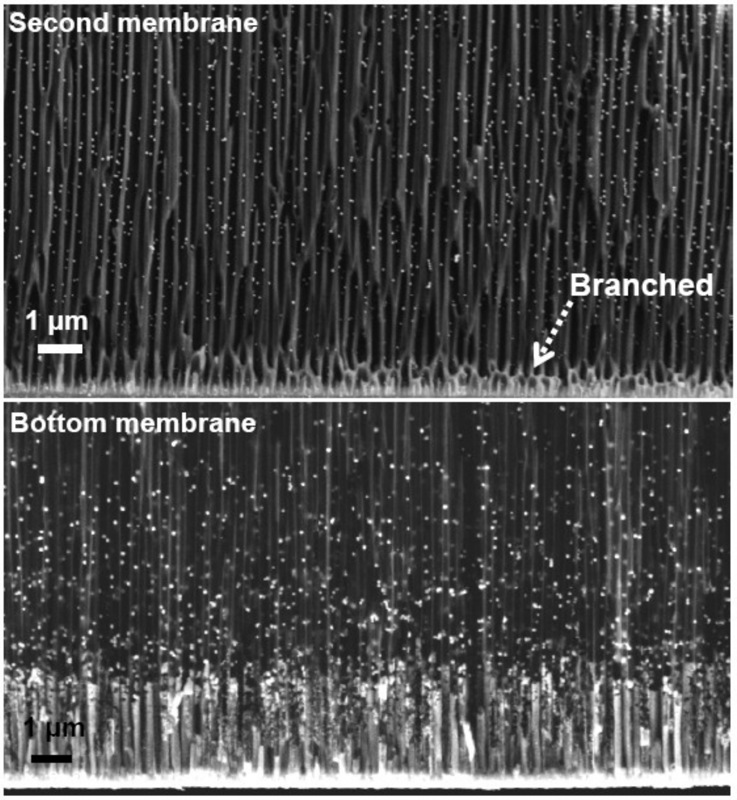

Figure 4.8 SEM micrographs of alumina membranes. The channels in one side of the second alumina membranes are branched and the size of this path is about 20 nm in diameter.

4.5 Effects of Ni^{2+} Ions on Morphology of Hollow Gold Nanoparticles

The morphology of hollow gold nanoparticles has been found to be related with Ni^{2+} ions. With Ni^{2+} ions the hollow gold nanoparticles with a complete shell were formed as shown in Figure 4.9. However, if Ni^{2+} ions are not present in the electrolyte, hemispherical gold nanoparticles form initially on the pore walls as shown in Figure 4.10 (a). If the reaction is allowed to progress for longer time, the initial particles grow and gold nanorods form as shown in Figure 4.10 (b). It is important to note that a round void is always present in every particle regarding of its size and shape. This experimental observation again strongly suggests that the formation of each gold nanoparticle occurs around electrochemically evolved hydrogen nanobubbles confined in the nanoscale channels in the alumina membrane.

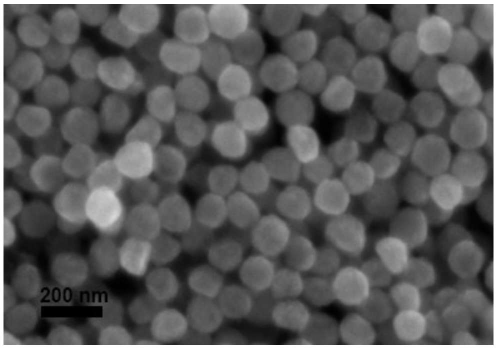

Figure 4.9 Hollow gold nanoparticles with complete shell. SEM micrograph of synthesized from an electrolyte with the pH adjusted by nickel sulfamate solution.

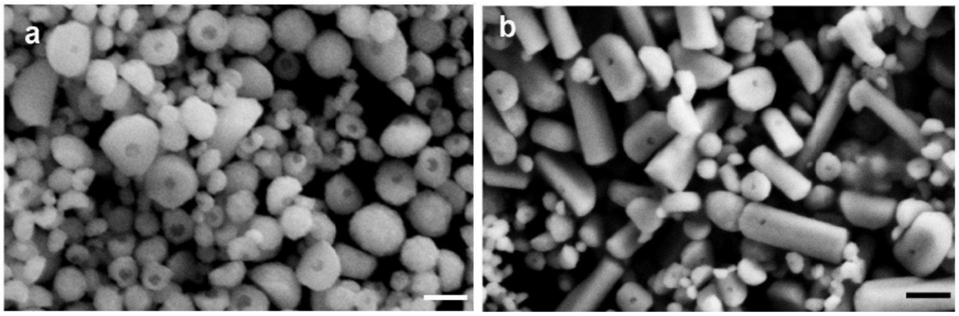

Figure 4.10 Gold nanoparticles with voids. SEM micrographs of synthesized from an electrolyte with the pH adjusted by sulfuric acid. (a) short deposition time (10 minutes). (b) long deposition time (60 minutes). The presence of a void in every particle is clearly shown, strongly suggesting that metal gold formation begins from a gas bubble. The scale bars are 200 nm.

The morphology of the resultant nanoparticles depends on the contact angle of bubbles on the nanopore walls, which is determined by the hydrophobicity of the wall surface. The half spheres resulted from bubbles with a contact angle of around 90°, and spheres from contact angles close to zero. The observation of the change of the nanoparticle morphology from half sphere to sphere by adding Ni^{2+} ions suggests that Ni^{2+} ions increases the hydrophobicity of the wall surface (the bubble contact angles). The interaction between Ni^{2+} ions and alumina membrane wall surface has been proposed to explain the fact that tubular structures can easily form when nickel is electrodeposited inside the alumina membrane(111, 112). Ni^{2+} ions are assumed to have higher affinity to alumina membrane pore wall surfaces on which hydroxyl groups are usually present. The change of surface charge of the alumina membrane wall surface due to the Ni^{2+} ions may contribute to the change of hydrophobicity of the wall surface. More research on the alumina-electrolyte interface is certainly needed to test this hypothesis.

4.6 Effects of Applied Potential and Deposition Time

Hydrogen evolution occurs electrochemically at a potential more negative than the H^+/H_2 equilibrium potential (-0.55 V vs. Ag/AgCl) at a pH = 6.0. At potentials positive to the equilibrium, no gold nanoparticles were observed inside the membrane; only electrodeposited metal rods formed on the bottom electrode. Hydrogen bubble nucleation required certain supersaturation level of hydrogen molecules which depends on the potential. When the potential is in the range from -0.7 V to -0.85 V, nanoparticles with uniform void size can be formed. We believed that this narrow potential window promotes homogeneous hydrogen bubble nucleation. The void size is a clear measure of the critical nucleus size of the hydrogen bubble. At potentials more positive to -0.7 V, a much smaller number of nanoparticles formed. At potentials more negative to -0.85 V copious hydrogen evolution occurs and the produced gold nanoparticles have a wide size distribution as a result of the wide size distribution of the produced hydrogen bubbles. The relation between the applied potential, the hollow gold nanoparticle size and the size distribution of hollow gold nanoparticles was summarized in Figure 4.11.

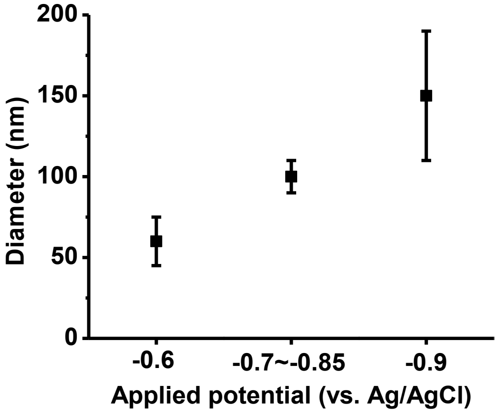

Figure 4.11 The relation between applied potential and hollow gold nanoparticle size and the size distribution of hollow gold nanoparticles. When the applied potential is in the range of -0.7 V to -0.85 V (vs. Ag/ AgCl), the hollow gold nanoparticles with the narrow size distribution can be achieved.

As the reaction time progresses, the shell thickness increases, and the total size of the hollow gold nanoparticles become much bigger as shown in Figure 4.12. But the size of the void remains the same around 50 nm.

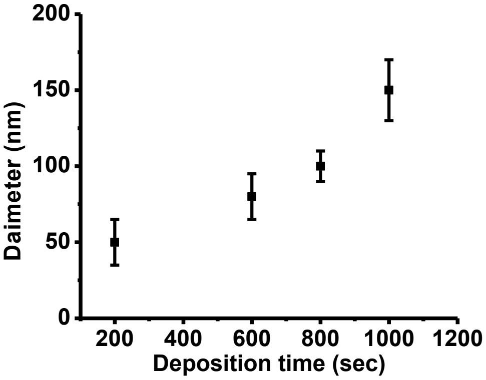

Figure 4.12 The relation between the deposition time and the size of hollow gold nanoparticles. The overall size gradually increased as the time increased.

4.7 Fabrication of Double-Shell Nanostructures

We also found that some nanoparticles have double-shell nanostructures as shown in Figure 4.13. These SEM micrographs were taken from gold nanospheres as extracted from membranes prior to any treatment. It was often observed that a few particles were already open and revealed a second half sphere inside the original particle.

The pulse potential method was conducted to demonstrate the possible route to fabricate such complex nanostructures. The fabrication of double-shell nanostructure was initiated with applied potential -0.8 V (vs. Ag/AgCl) for 600 seconds followed by an open circuit for 300 seconds. The pulse potential was repeated for two cycles. Figure 4.14 shows the SEM micrograph of double-shell nanostructures after ion milling treatment. The diameter of the first void is about 50 nm and the overall size is about 300 nm

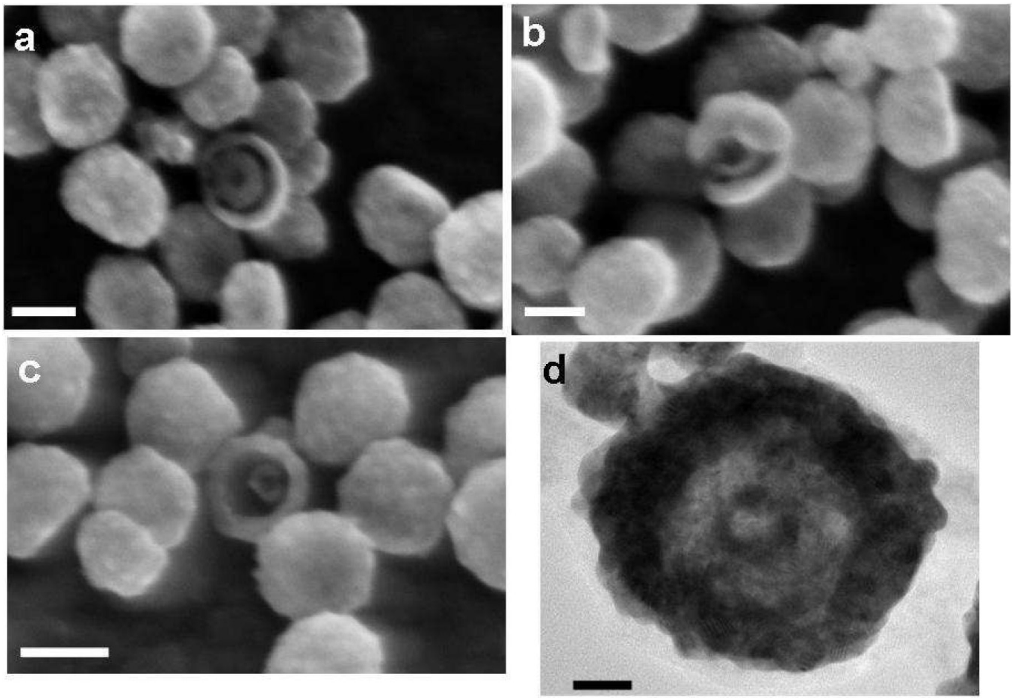

Figure 4.13 Double-shell nanostructures. SEM micrographs (a, b and c) showing some “nanomatryoshka” structures. The scale bars are 100 nm. (d) High resolution TEM micrograph. The scale bar is 20 nm.

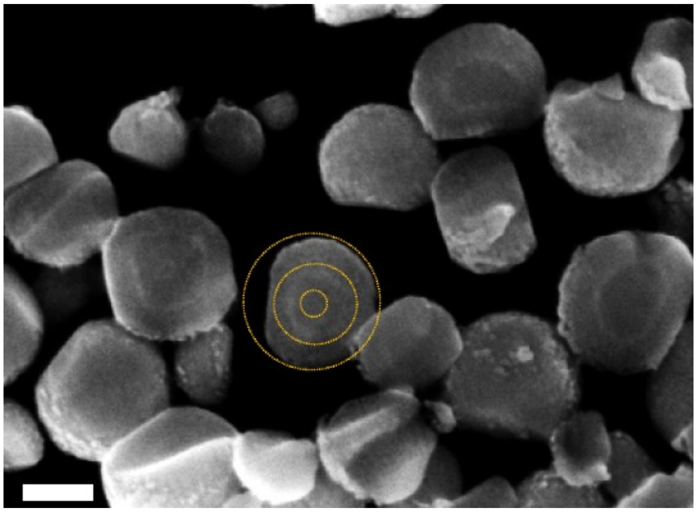

Figure 4.14 SEM micrograph of double-shell nanoparticles after ion milling treatment. The diameter of the first void is about 50 nm and the overall size is about 300 nm. The scale bar is 200 nm.

The possible route for the formation of these nanostructures can be considered as follows. After metallic gold forms in the surrounding of a hydrogen nanobubble, a larger bubble grows on the same or a nearby site and engulfs the already-formed gold nanoparticles. Then again, metallic gold forms on the surface of the larger bubble.

CHAPTER 5

PLASMONIC PROPERTIES OF HOLLOW GOLD NANOPARTICLES

5.1 Introduction

In Figure 5.1 shows the absorption spectra of hollow gold nanoparticle suspensions together with the calculated results using Mie theory applied computer code. Some of the measured peaks are red-shifted to NIR region compared to the simulation. This may be due to either the presence of the displacement of voids from the center of the spheres or the roughened surface of hollow gold nanoparticles. In order to study these two effects, the FDTD simulation was used to understand the plasmonic properties of hollow gold nanoparticles.

The simulation results show, for the non-concentric hollow gold nanoparticle, the offset of the void center only caused a slightly red-shift of SPR peak within the visible light region. The SPR peak red-shifted into near-infrared region is result from the surface roughness of hollow gold nanoparticles. This surface roughness dependence of plasmonic properties of hollow gold nanoparticle was discussed in details. The surface roughness of hollow gold nanoparticles can be controlled by controlling the pH of the electrolyte. The much roughened surface could be achieved with the increased pH of gold sulfite electrolyte.

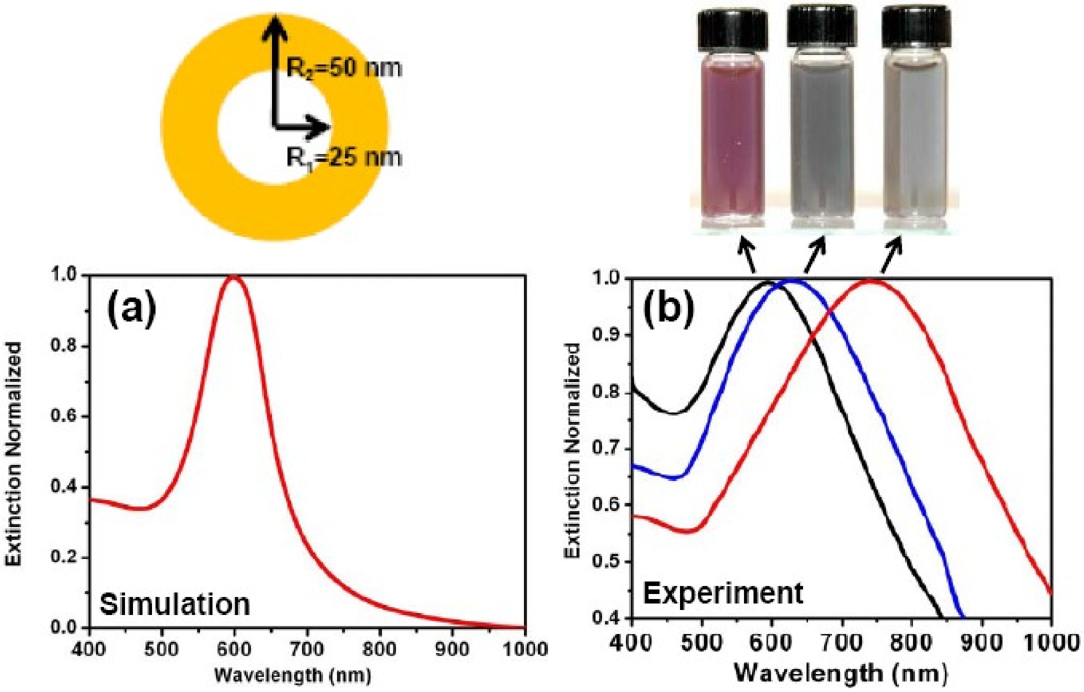

Figure 5.1 Absorption spectra of hollow gold nanospheres with the same inner radius R_1, and outer radius, R_2, (R_1, R_2)=(25,50) nm and dispersed in water. (a) Calculated total extinction for hollow nanospheres using Mie theory applied computer code. (b) Measured absorption peaks for hollow gold nanoparticle and the upper panel: vials containing hollow gold nanoparticle. The measured peaks are red-shifted compared to the calculation. This may be due to the displacement of void from the center of the spheres and the surface roughness.

5.2 Three-Dimensional Finite Difference Time Domain (FDTD)

FDTD has recently been shown to be highly useful in the study of the electromagnetic properties of metallic nanostructures of almost arbitrary complexity(113). FDTD method is an explicit time marching algorithm used to solve Maxwell's curl equations on a discrete spatial grid. It can be used for studying both the near and far field electromagnetic responses for heterogeneous material of arbitrary geometry. In this method, the electromagnetic field and a target structure are described on a discrete mesh make up of so-called 'Yell cells". In these Yell cells, the electric field components form the edges of the cube, and the magnetic field components form the normal to the faces of the cube. The incoming light pulse or wave illuminates a target containing one or several nanoparticles or structures. The electromagnetic field excites plasmon in the nanoparticles. The plasmon interacts on the nanoparticles resulting in a complicated and time dependent electromagnetic field. Maxwell's equations are solved discretely in time. The time step used is related to the mesh size through the speed of light. Therefore, FDTD is an exact representation of Maxwell's equations in the limit that the mesh spacing goes to zero. The schematically drawing in Figure 5.2 shows the type of phenomenon that will be modeled.

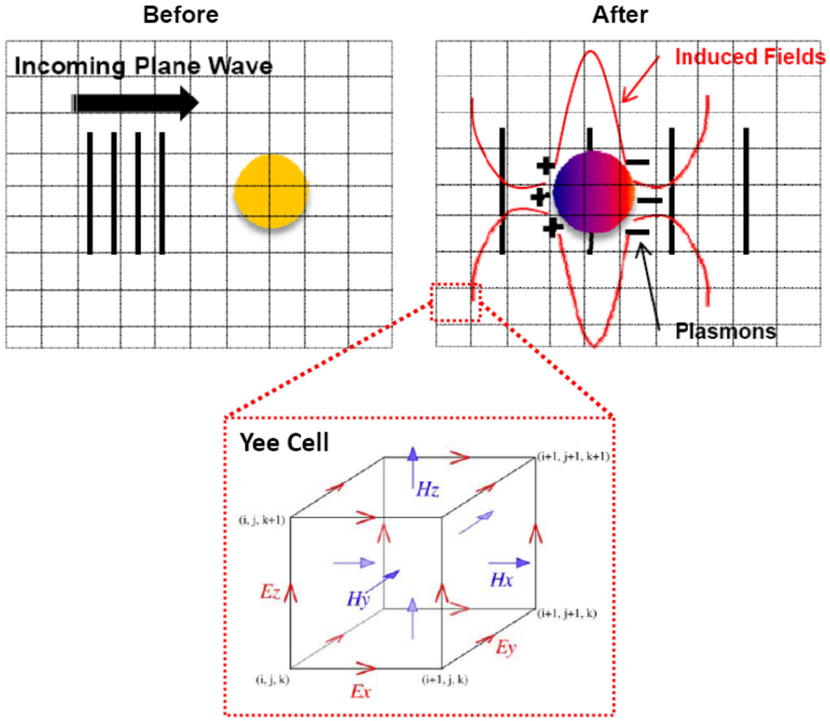

Figure 5.2 A typical nanoparticle experiment. A nanoparticle is illustrated with a plane wave. Surface plasmons are induced on the nanoparticle, creating local electromagnetic fields.

The model of a hollow gold nanoparticle is a nanosphere with an outer radius R_2=50 nm and inner radius R_1=25 nm embedded in water suspension, and the plane wave comes in from the left side, as shown in Figure 5.3. The calculation region is truncated by six perfectly matched layers (PMLs) boundary. The electromagnetic wave incidents upon the PML from a non-PML medium do not reflect at the interface. This property allows the PML to strongly absorb outgoing waves from the interior of a computational region without reflecting them back into the interior. Since the FDTD technique uses a finite volume to consider the electromagnetic wave propagating in infinite space, i.e. simulate an open-region problem by using a closed one, the boundary condition must be able to absorb the scattering field component arriving at the boundary edge from all directions as if no artificial boundary is applied at all. Therefore, inside the PML surface, the electromagnetic field was divided into two regions: the total field region and the scattering field region.

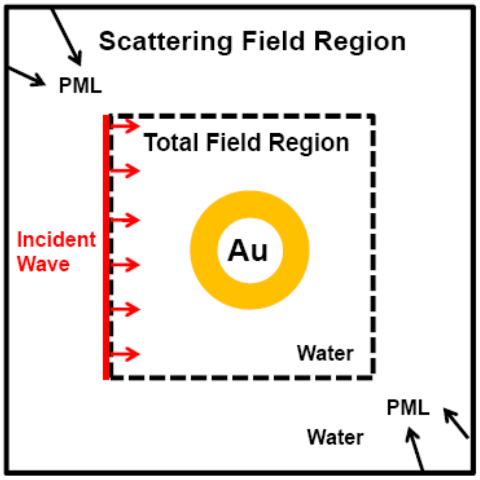

Figure 5.3 Schematic of 2-D cross-section of FDTD simulation domain.

The parameters for the simulation include the complex dielectric constant for the core, shell, and surrounding medium, ε_c, $\varepsilon(\omega)_{exp}$, *and* ε_m. ε_c was taken to be *1.0 + 0i* at all wavelengths. For $\varepsilon(\omega)_{exp}$ ($=\varepsilon_1+i\varepsilon_2$), values of the complex dielectric function at different wavelengths for bulk gold were obtained from the literature (43). Spline interpolation was used to obtain the complex dielectric constants at intermediate wavelengths, where data was not available directly from the literature as shown in Figure 5.4. ε_m was taken to be *1.77 + 0i* at all wavelengths for water.

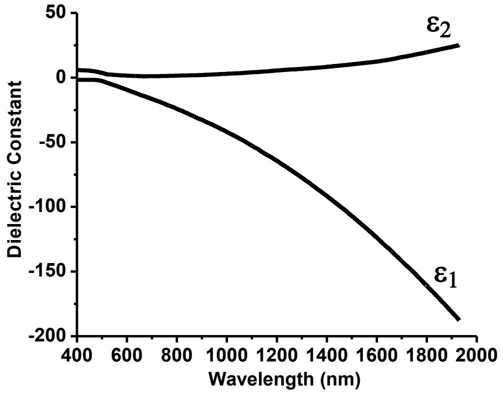

Figure 5.4 Spline interpolation was used to obtain the complex dielectric constants at intermediate wavelengths, where data was not available directly from the literature.

In bulk gold the conduction-electron mean free path at room temperature is ~42 nm (114). Since the shell thickness (25 nm) of hollow gold nanoparticle is less than the bulk gold electron mean free path, a contribution to the complex dielectric function $\varepsilon(\omega)_{exp}$ due to the size-dependent electron scattering becomes important. The bulk gold collision frequency has to be modified as Equation 5-1(115).

$$\Gamma = \gamma_{bulk} + A \times \frac{V_F}{a} \tag{5-1}$$

where γ_{bulk} is the bulk collision frequency V_F is the Fermi velocity of gold, a is the reduced electron mean free path. For our nanoparticles, we take a equal to the shell thickness, ($R_2 - R_1$). A is a parameter which depends upon the geometry and theory used to derive this expression(116). In the context of simple Drude theory and isotropic scattering, A=1. The bulk dielectric function of the hollow gold nanoparticles was then modified follows:

$$\varepsilon_s(a,\omega) = \varepsilon(\omega)_{exp} + \frac{\omega_p^2}{\omega^2 + i\omega\gamma_{bulk}} - \frac{\omega_p^2}{\omega^2 + i\omega\Gamma} \tag{5-2}$$

ε_a (a,ω) is the size-dependent dielectric function where ω_p is the bulk plasmon frequency of gold.

$$\varepsilon(\omega)_{exp} = \varepsilon_1 + i\varepsilon_2 \tag{5-3}$$

$$\text{Real part: } \varepsilon_1 + \frac{\omega_p^2}{\omega^2+\gamma^2_{bulk}} - \frac{\omega_p^2}{\omega^2+\Gamma^2} \tag{5-4}$$

$$\text{Imaginary part: } \varepsilon_2 - \frac{\omega_p^2\gamma_{bulk}}{\omega^3+\omega\gamma^2_{bulk}} + \frac{\omega_p^2\Gamma}{\omega^3+\omega\Gamma^2} \tag{5-5}$$

5.3 Effects of Non-Concentric Core

It has been shown the red-shift of the SPR peaks on non-concentric gold nanoshells comparing to the concentric ones(59). For a spherically symmetric gold nanoshell, where the center of the inner shell surface is coincident with the center of the outer shell surface, plasmon hybridization only occurs between cavity and sphere plasmon states of the same angular momentum, denoted by multipolar index *l*. In the dipole, only the dipolar bonding plasmon (*l* =1) is excited by an incident optical plane wave. However, when the center of the inner shell radius is displaced with respect to the center of the outer shell radius, the plasmons of all multipolar from the cavity and sphere are hybridized as shown in Figure 5.5. As a consequence, all plasmon modes of this structure can be optically excited resulting in a red-shifted of SPR peaks as shown in Figure 5.6(117).

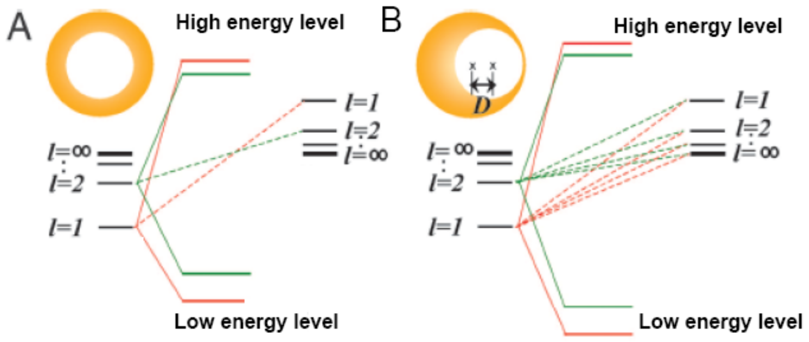

Figure 5.5 Schematic of plasmon hybridization in a (A) concentric gold nanoshell and (B) non-concentric gold nanoshell. l is a multipolar index (l=1: diploe, l=2: quadrupole etc.), and D is the displacement spacing(118).

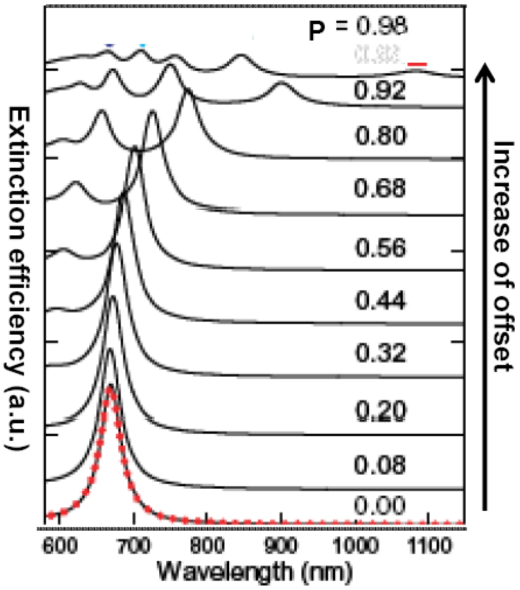

Figure 5.6 Extinction properties of non-concentric gold nanoshells with an outer radius R_2=35 nm and inner radius R_1=30 nm. The displacement P = offset (D)/(R_2-R_1), and P=0 corresponding to the gold nanoshell with concentric structure. The SPR peak shifts to longer wavelength with the increase of the offset distance (D)(117).

Concentric and non-concentric hollow gold nanoparticles were constructed with the same inner radius 25 nm and outer radius 50 nm. The non-concentric hollow gold nanoparticle has a displacement of the void with a 2 nm of shell thickness on the thinnest side as shown in Figure 5.7. Compared to the concentric hollow gold nanoparticle, SPR peak of the non-concentric hollow gold nanoparticle was only slightly red-shifted from 600 nm to 630 nm within the visible region as shown in Figure 5.7. Therefore, the displacement of the void cannot be the main factor to cause the SPR peaks of hollow gold nanoparticles to red-shift into the NIR region.

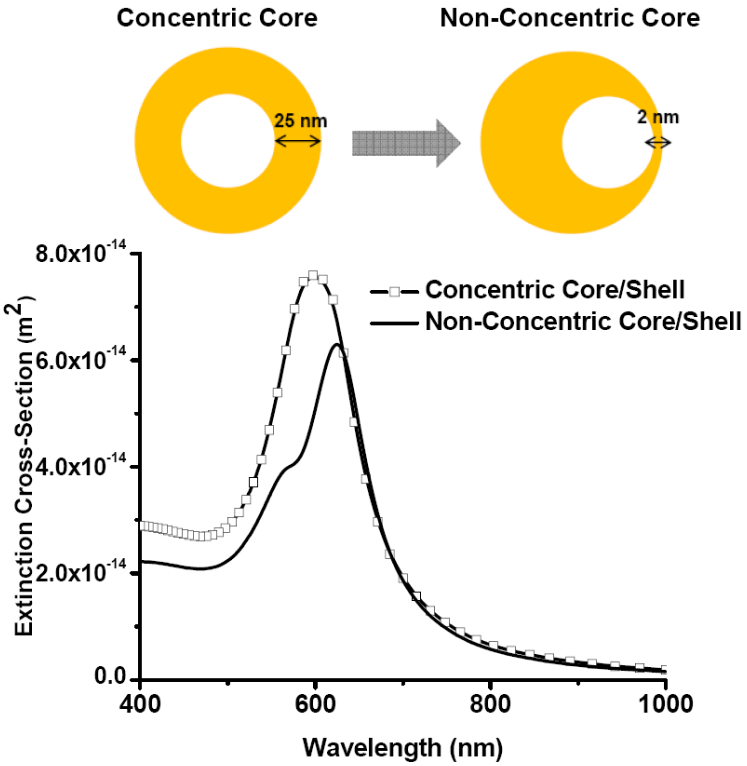

Figure 5.7 The simulated SPR response of one hollow gold nanoparticle has the same inner radius R_1, and outer radius, R_2, (R_1, R_2)=(25,50) nm. The non-concentric hollow gold nanoparticle has a displacement of the void with a 2 nm of shell thickness on the thinnest side.

5.4 Effects of Surface Roughness

Another possible reason for the red-shift of SPR is the surface roughness. The effect of surface texturing on the optical properties of sub-micrometer gold nanoshells have been investigated(119, 120). The surface roughness was achieved by using site-selective chemical etchant, biofunctional alkanethiol molecule (cysteamine). The degree of surface roughness of gold nanoshells is directly relative to the etching time as shown in Figure 5.8. The relative roughened surface can be obtained by increasing the etching time. The effect of roughness has also been observed in highly corrugated and porous gold rods(121, 122). All these works have shown that the surface roughness can induce red-shifts of SPR peaks. In other words, the surface roughness can be used as another tool to tune the SPR responses of gold nanoparticles. In Figure 5.9 shows time-dependent vis-NIR spectra of a gold nanoshell (average core radius of 93 nm and shell thickness of 35 nm) film immersed in 50 mM cysteamine solution(123). The SPR peaks are red-shifted as the immersing time increased in terms to the increase of surface roughness.

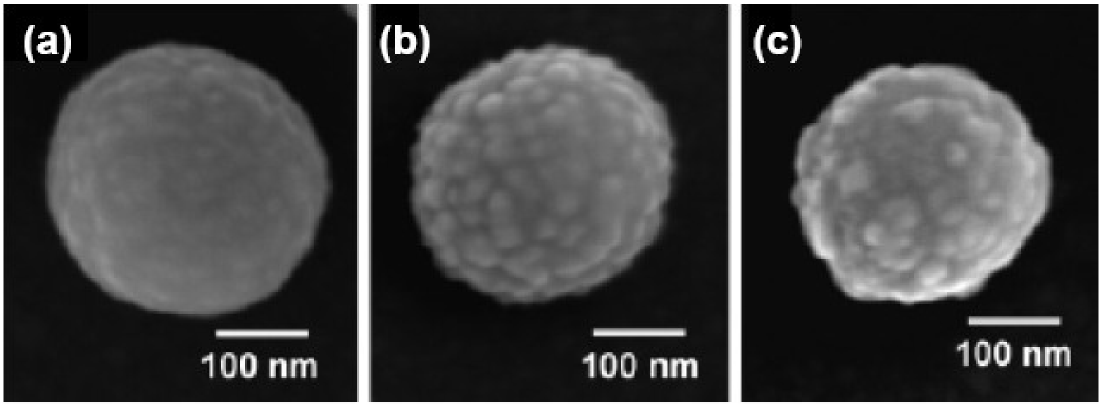

Figure 5.8 Surface morphological changes during etching: High resolution SEM images of the gold nanoshells (a) before etching, and (b) and (c) after immersed in 50 mM cysteamine for 1 h and 2 h, respectively. The whole etching process can be divided into three stages: relatively smooth nanoshells, rough nanoshells, and isolated gold islands attached on the silica surface(123).

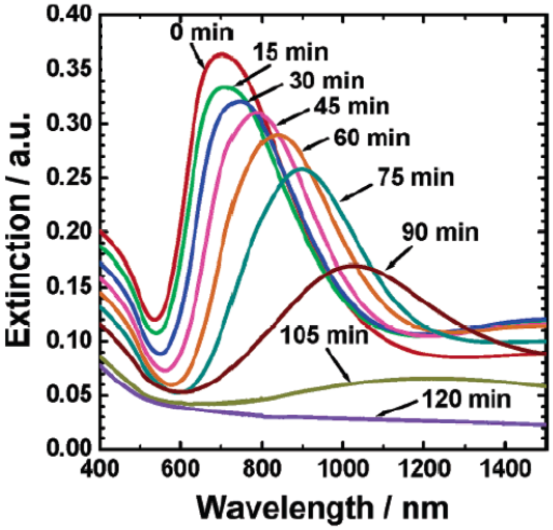

Figure 5.9 Time-dependent vis-NIR spectra of a gold nanoshell (average core radius of 93 nm and shell thickness of 35 nm) film immersed in 50 mM cysteamine solution(123).

5.4.1 FDTD Simulation

The rough surface was generated using a random number algorithm. The roughness is defined as the average amplitude of the sinusoidal-like waves. Hollow gold nanoparticle has the same inner radius R_1= 25 nm and outer radius R_2= 50 nm but different surface roughness, a smooth surface, a roughness of 5 nm and a roughness of 8 nm as shown in Figure 5.10.

Figure 5.10 The surface was generated using a random number algorithm and the roughness is defined as the average amplitude of the sinusoidal-like waves. Hollow gold nanoparticle has the same inner radius R_1, and outer radius R_2, (R_1, R_2)=(25, 50) nm but different surface roughness. (a) a smooth surface, (b) a roughness of 5 nm and (c) a roughness of 8 nm.

In Figure 5.11 are the simulated extinction spectrum responses of solid and hollow gold nanoparticles with different surface roughness. Solid and hollow gold nanoparticles have the same outer radius of 50 nm and hollow gold nanoparticles have the same inner radius of 25 nm. For comparison, the extinction spectrum for solid gold nanoparticle (dashed line) with the same roughness as hollow gold nanoparticles (solid line) is shown in the Figure 5.11. Compared to solid particles, SPR peaks for hollow gold nanoparticles are only slightly red-shifted. This can be attributed to the relatively thick shell (>20 nm), which is very different from other nanoshell structures reported in literature, where very thin shells lead to a wide tunability of SPR peaks. For gold nanoparticle with smooth surface, the SPR peak is at ~600 nm. For gold nanoparticles with a roughness of 5 nm, SPR peak shifts to longer wavelength about ~630 nm and as the roughness increases to 8 nm, a much greater red-shift about ~730 nm is observed, The surface roughness significant increased the extinction cross section; from 5.96×10^{-14} m^2 for gold nanoparticles with smooth surface to 9.13×10^{-14} m^2 for gold nanoparticle with very rough surface. (physical cross section for 100 nm particle is 3.14×10^{-14} m^2)

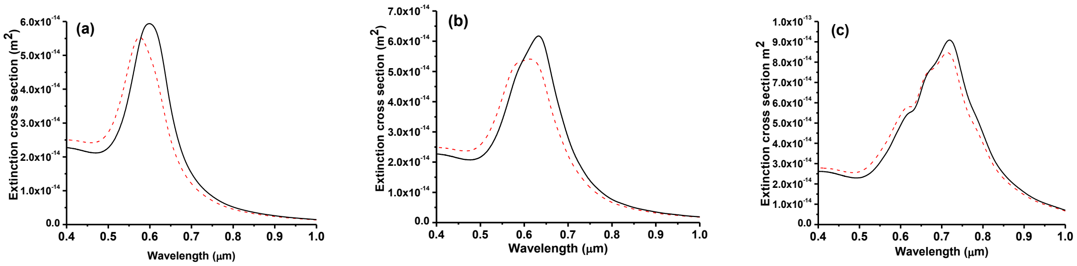

Figure 5.11 The simulated extinction spectrum responses of one solid and one hollow gold nanoparticle with different surface roughness. Solid and hollow gold nanoparticles have the same outer radius of 50 nm and hollow gold nanoparticles have the same inner radius of 25 nm. The extinction spectrum for hollow gold nanoparticle (solid line) (a) with a smooth surface. (b) with a roughness of 5 nm. (c) with a roughness of 8 nm. The extinction spectrum for solid gold nanoparticles with the same roughness as hollow gold nanoparticle (dashed line) is also shown for comparison.

In Figure 5.12 shows the two-dimension plot of the enhancement of the electric field when illuminated by light of the resonance peak and these results are corresponding to the results in Figure 5.11. Compared with the hollow gold nanoparticle with smooth surface, hollow gold nanoparticles with a roughness of 5 nm, the large enhanced electric field was observed and several hot spots appeared on the surface. As the roughness increases to 8 nm, almost all bumps became hot spots with very large electric field enhancement factor about ~200. The roughness effect is due to the strong interaction of electric fields from adjacent bumps, similar to the plasmonic properties of the aggregates of several nanoparticles that are known as "Dimer Effect"(124).

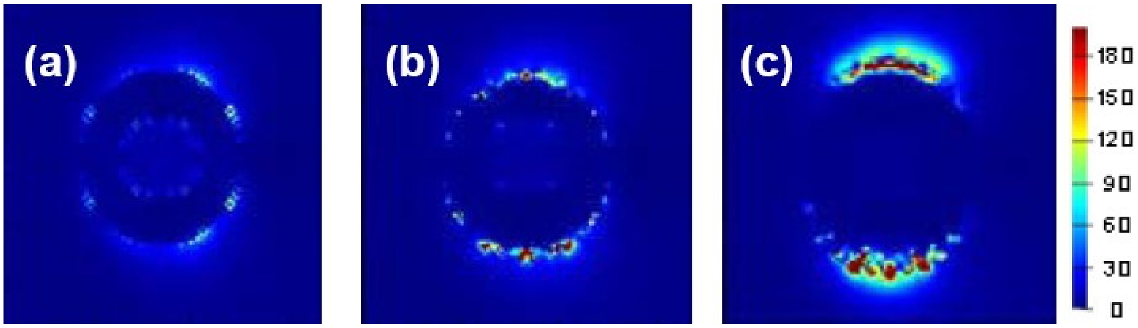

Figure 5.12 The two-dimension plot of the enhancement of the electric field when illuminated by light of the resonance peak for hollow gold nanoparticle with different roughnesses. Hollow gold nanoparticle has the same inner radius R_1, and outer radius R_2, (R_1, R_2)=(25, 50) nm. (a) with a smooth surface. (b) with a roughness of 5 nm. (c) with a roughness of 8 nm.

When the distance between two gold nanoparticles is relative far away, there is no plasmon coupling exist. But with the decrease of this distance, the strong plasmon coupling is occurred and creates so called “Hot Spot” between two nanoparticles. In Figure 5.13 shows the two-dimension plot of the enhancement of the electric field when two gold nanoparticles (diameter = 6 nm) with different gap distance, 2 nm and 7 nm are illuminated by light. The results show that the electric field was strongly enhanced with the decreased gap distance and the “Hot Spot” was also observed. Figure 5.14 shows the extinction spectrum corresponding to the Figure 5.13. The SPR peaks slightly red-shifted when gap distance is narrowed and two distinct resonance modes can be also observed for each curve. The main resonance peaks associated with coupled plasmon mode within the gap and the minor resonance peaks associated with dipole resonance of each single nanoparticle. The results also indicated that coupled plasmon is a main dominator in this dimer effect. The dimer effect significant increased the extinction cross section; from 3.1×10^{-17} m^2 for a 7 nm gap to 4.58×10^{-17} m^2 for a 2 nm gap.

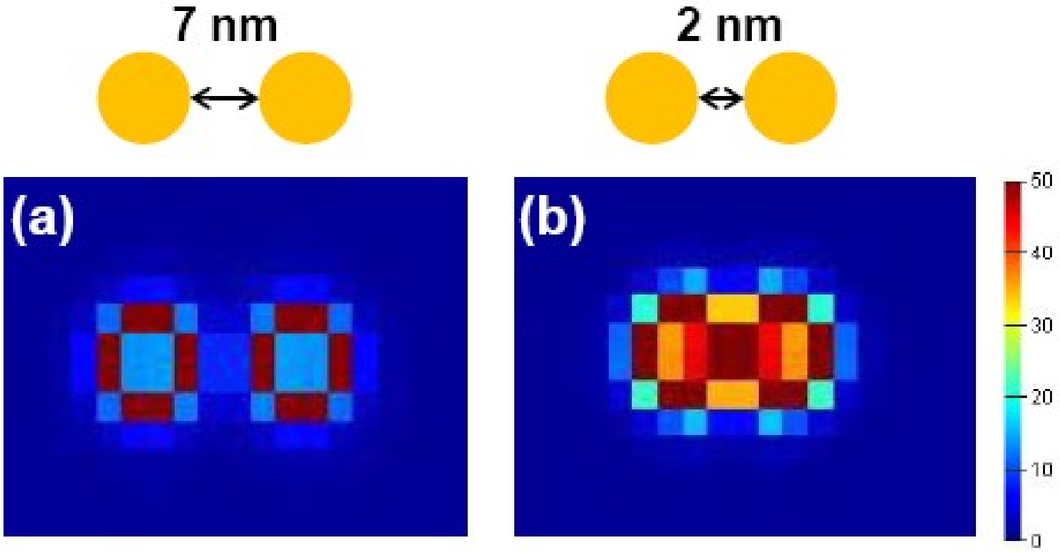

Figure 5.13 Effect of the gap distance between two adjacent gold nanoparticles forming a dimer. The two-dimension plot of the enhancement of the electric field when illuminated by light for two gold nanoparticles (diameter = 6 nm) with (a) a 7 nm gap and (b) a 2 nm gap. When the gap is decreased, the strong plasmon coupling created the "Hot Spot" in between.

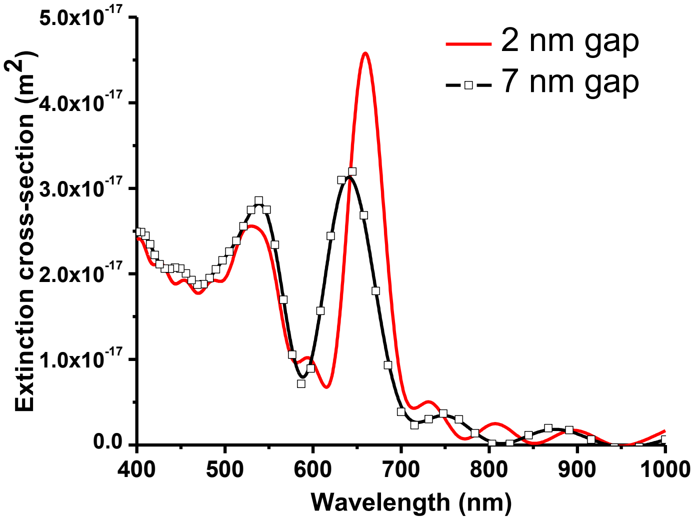

Figure 5.14 Effect of the gap distance between two adjacent gold nanoparticles forming a dimer. The simulated extinction spectrum of two gold nanoparticles (diameter = 6 nm) with different gap distance, 2 nm and 7 nm. The slightly red-shift of SPR peaks were observed when the gap distance is decreased.

5.4.2 Fabrication of Hollow Gold Nanoparticles with Roughened Surface

We have found that the surface roughness of hollow gold nanoparticles highly depends on the pH of the electrolyte. 0.2 M Na_2SO_3 (pH~9.0) was prepared to adjust the pH of the electrolyte. As shown in Figure 5.15, the surface of nanoparticles synthesized using electrolyte with a pH of 6.0 is pretty smooth. As pH increases to 6.5, the surface roughness increases. At pH = 7.0, large bumps and dimples appear on the surface. This pH dependence of the roughness can be attributed to the fact that the rate of autocatalytic reaction of $Na_3Au(SO_3)_2$, and in turn the gold grain growth rate, increases with pH.

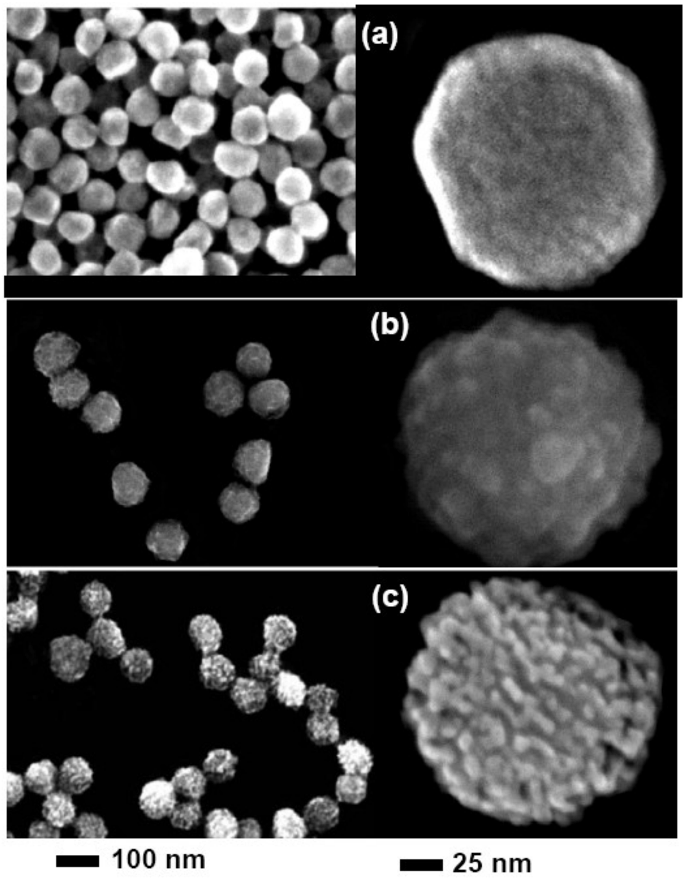

Figure 5.15 Surface morphology of hollow gold nanoparticles synthesized using electrolytes with different pH values. SEM micrographs (a) for a pH= 6.0. It shows relatively smooth surface. (b) for a pH= 6.5, showing the rough surface of hollow gold nanoparticles. (c) for a pH= 7.0. It shows very rough surfaces with bumps and dimples.

Figure 5.16 shows absorption spectra of corresponding nanoparticle water suspensions. The dashed line is the simulated result which is detailed in Figure 5.11. It can be seen that the plasmon peak shifts to longer wavelength with the increase of pH in electrolyte during the particle synthesis process. Since the core dimensions of all these nanoparticles do not change, such red–shift can only be explained by the increase of the surface roughness. When the pH changes from 6.0 to 6.5, the SPR peaks slightly shift from 600 nm to 630 nm. As pH increases to 7.0, a significant red-shift occurs; SPR peak shifts to 730 nm. As shown in Figure 5.16, the simulated results are in good agreement with experimental results. The roughness of synthesized hollow gold nanoparticle is due to the polycrystalline nature of the shell. The grain sizes are in the range from 5 nm to 8 nm, which can be a measure of the surface roughness.

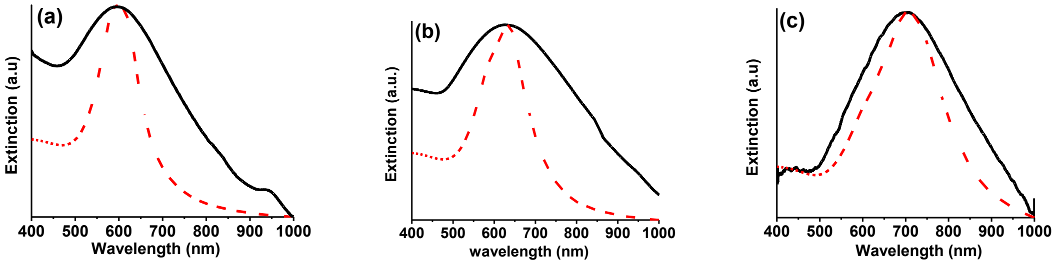

Figure 5.16 Absorption spectra of hollow gold nanoparticles synthesized using electrolytes with different pH values. (a) At pH=6.0, the SPR peak lies around 600 nm (solid line). (b) At pH=6.5, the SPR peak is around 630 nm (solid line). (c) At pH=7.0, the SPR peak shifts to 750 nm. The dashed lines are the simulated results that are detailed in Figure 5.9. The simulated results are in good agreement with experimental results.

However, in Figure 5.16 clearly shows that the simulated width of the plasmon resonances is far narrower than the experimental results. Several factors can contribute to the line shape of plasmon resonances. The first broadening mechanism in the plasmon experiment may be the non-uniform size distribution. According to the dynamic light scattering (DLS) measuring results, the experimental estimation of the size dispersion is a size distribution with a standard deviation of 10 %. A second factor in this experiment may be that the hollow gold nanoparticles are not perfectly spherical. It would be reasonable to expect that the hollow gold nanoparticle surfaces are relatively defect-rich during growth and may not be of uniform thickness. The third broadening factor is finite-size effects. When the shell thickness of the hollow gold nanoparticle is smaller than the mean free path of the electrons (~42 nm)(114), electron surface scattering will introduce an extra broadening of the plasmon resonance (15). This effect can be incorporated into the classical calculations by modifying the Γ factor in the bulk dielectric function. This modification influences the width of the resonance but leaves the energy unchanged. The forth important factor contributing to the plasmon widths in nanoparticles is phase retardation effects which increase the multipolar oscillations of the nanoshells and prevents the dipole from being tuned to shorter wavelengths that results in the generation of higher order plasmon modes, such as quadrupole, octupole and then caused the broadening of the plasmon resonances.

CHAPTER 6

IN VIVO BIOMEDICAL APPLICATIONS OF HOLLOW GOLD NANOPARTICLES

In this chapter, we demonstrate two routes to construct hollow gold nanoparticles as multifunctional agents for *in vivo* biomedical applications. First, pegylated Raman dye encoded hollow gold nanoparticles, terms as Raman nanotags, can be used as both optical diagnostic imaging agents and photothermal agents. The Raman nanotags have demonstrated their capability to enhance Raman scattering signal for the cell imaging. The cytotoxicity evaluation using [^{3}H] thymidine incorporation method has shown no sign of toxicity from both Raman nanotags and pegylated hollow gold nanoparticles. We also performed a calculation to estimate the heating efficiency of two kinds of gold nanoparticles, spherical gold nanoparticles and hollow gold nanoparticles used in photothermal applications. The calculation results show the temperature increase on the surface of gold nanoparticle is directly relative to the size of the nanoparticle, the intensity of the irradiation and the surface roughness of gold nanoparticles. In the photothermal experiment, the photothermal effects of hollow gold nanoparticles were evaluated in tissue-like phantom environment and recording the infrared images as temperature increase. The results show hollow gold nanoparticles are capable to generate sufficient heat to destroy the cancer cells. Second, trapping iron oxide nanoparticles inside hollow gold nanoparticles, terms as Fe_3O_4/Au core/shell nanoparticles, can be used as magnetic resonance imaging (MRI) contrast agents and photothermal agents. The results show Fe_3O_4/Au core/shell nanoparticles retained unique plasmonic and magnetic properties.

6.1 Fabrication of Raman Nanotags as Diagnostic Agents

Hollow gold nanoparticles were synthesized as described in chapter 4. Hollow gold nanoparticles with an inner diameter 50 nm and an outer diameter 100 nm, and the absorption peak centered at 730 nm were used to fabricate Raman nanotags. In order to achieve the maximum coverage of Raman reporter dye on the surface of hollow gold nanoparticles, the process was done before the dissolution of alumina membrane. An anodic alumina oxide membrane containing 1.1×10^{11} particles/mL hollow gold nanoparticles was immersed into a freshly made 20 mL of 5 μM diethylthiatricarbocyanine (DTTC) Raman reporter dye solution for 3 hours at room temperature. Then, the alumina membrane was rinsed with deionized water several times to allow complete diffusion of the DTTC out of the membrane. Raman-active hollow gold nanoparticles within the alumina membrane were further pegylated with 20 μM SH-mPEG (MW 5kDa) by an overnight incubation at 4^{0}C. The alumina membrane was dissolved using 1 M NaOH solution. The nanoparticles were cleaned by several cycles of dispersion in deionized water followed by centrifugation. The preparation process of Raman nanotag is illustrated in Figure 6.1.

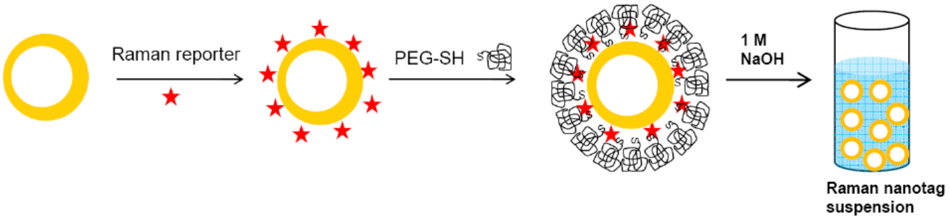

Figure 6.1 Illustration of the preparation process of Raman nanotag. In order to achieve the maximum coverage on hollow gold nanoparticles surface, the process was done before the dissolution of alumina membrane. After attachment of Raman reporter and pegylation, alumina membrane was dissolved using 1 M NaOH solution to release the Raman nanotags into solution.

6.1.1 Raman Spectroscopy Measurement

The Raman spectroscopy measurement was conducted in a home-made setup with a 785 nm laser light. Briefly, the laser light is propagated through an optic fiber (600 μm, NA=0.39) to a Raman module. At the Raman module, the light from this fiber attenuated by a neutral density filter (ND= 0.2) and collimated before it was incident on a dichotic which reflects the laser onto a 20X, 0.4 NA objective lens with working distance of 8.4 cm. The cell containing the Raman nanotag suspension is placed at the focus of this lens for SERS measurement. Light reflected and scattered by the suspension is collected by the objective and transmitted by the dichotic to a notch filter before being focused by a 10X, 2.5 NA lens into optic fiber (600 μm, NA=0.39) which then propagates the light to a spectrometer. The spectra were acquired with an exposure time of 8 seconds.

The Raman spectra of 50 μL Raman nanotags with concentration 5.8×10^{10}/mL demonstrated the major vibrational modes of DTTC at 379, 489, 622, 778, 843, 1017, 1074, 1103, 1129, 1232, 1329, 1405, 1460 and 1513 cm^{-1} as shown in Figure 6.2. This indicates the stable absorption of Raman dyes on the surface of hollow gold nanoparticles after going through the whole process including dissolving the alumina membrane using high concentration 1M NaOH solution.

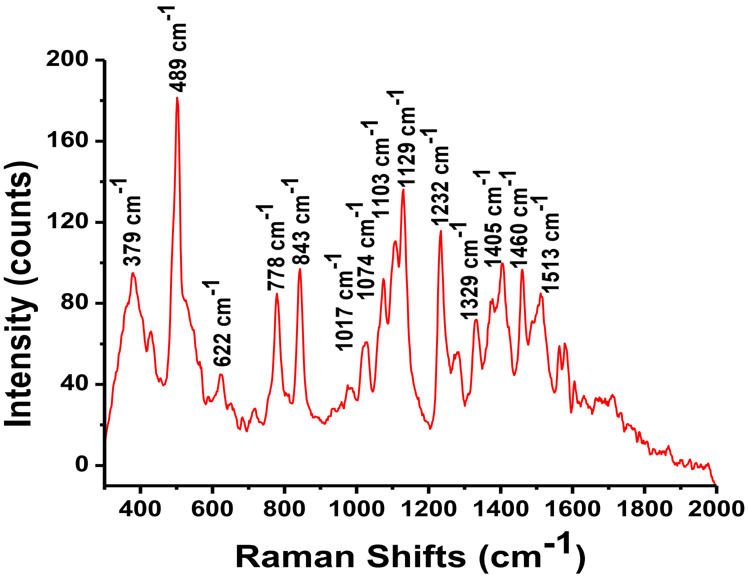

Figure 6.2 The Raman spectra of Raman nanotags showing all major vibrational modes of DTTC.

The attachment of DTTC to gold nanoparticles has been reported, and its stability was attributed to the fact that DTTC is positively charged and contains delocalized π-electrons and citrate-reduced gold nanoparticles has net negative charge on the surface. Both the electrostatic force and delocalized π-electrons contribute the strong absorption of DTTC on gold nanoparticles surface. However, the functionalization process of hollow gold nanoparticles was conducted before the dissolving of the alumina membrane in which the nanoparticles are well separated and fixed on the pore wall surface of the alumina membrane. It is not expected that hollow gold nanoparticles have any net charge on their surface since they have been washed with deionized water many times. Therefore, the absorption of DTTC on the hollow gold nanoparticles surface could be very weak. The possible mechanism for the stability can be that the thiol-PEG layer protects and stabilizes the weakly absorbed reporter dyes by electrostatic force and shielding. The stability due to steric effect rather than electrostatic effect is implied in Figure 6.3, where the absorption spectra of Raman nanotags in water and in 10 mM buffered saline (PBS) buffer solution are compared. Because of the very high ionic strength of PBS, electrostatically stabilized particle suspensions usually lose their stability in PBS buffer. Particles aggregate and absorption spectrum changes accordingly. Here, the absorption spectrum in PBS slightly shifts towards longer wavelength, and the peak slightly broadened. This may be due to the difference of refractive index between water and PBS buffer. The very small change in absorption spectrum in PBS buffer suggests that the PEG layer covers the particle surface and provides steric shielding. Also, shown in Figure 6.4 (a) is the result of dynamic light scattering (DLS) measurement, which is confirmed with the SEM micrograph, shown in Figure 6.4 (b). The particle size measure using DLS is about 10 nm larger than the size measured by inspecting the SEM images, Figure 6.4 (b), which is consistent with the conclusions drawn in the literature for pegylated gold nanoparticles(125).

Stability of the Raman nanotags was also tested in 3 M NaCl solution at room temperature. The Raman nanotag solutions were monitored by UV-VIS spectroscopy measurement up to one month. It does not show any sign of aggregation.

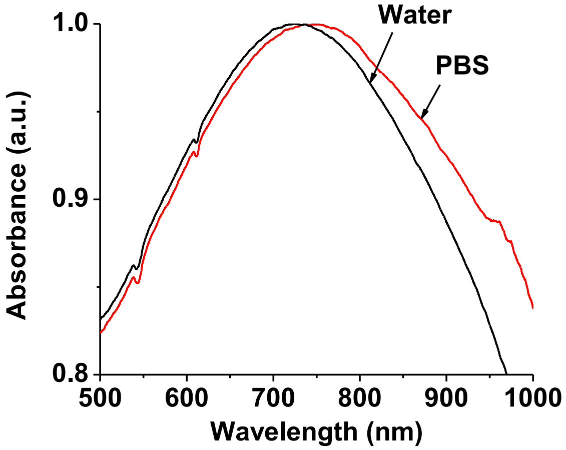

Figure 6.3 Comparison of the absorption spectra of Raman nanotags in water and in 10 mM phosphate buffered saline (PBS) buffer solution. The very small change in absorption spectrum in PBS suggests that PEG layer covers the particle surface and provides steric shielding.

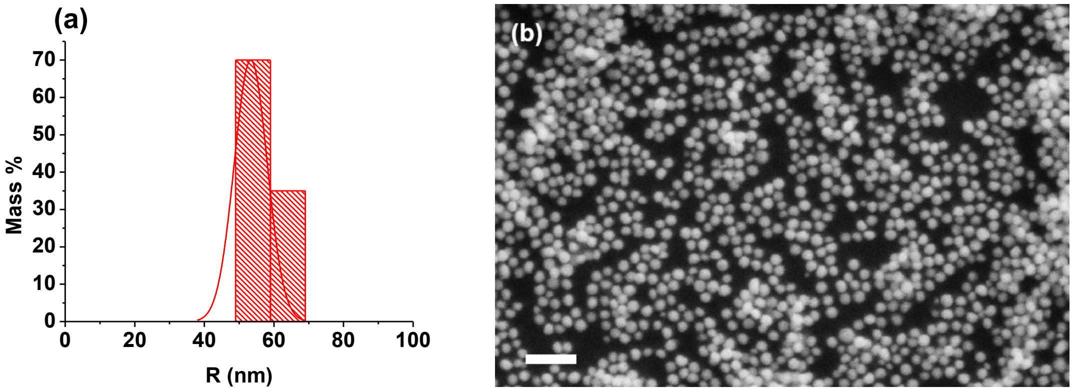

Figure 6.4 (a) Particle size distribution of Raman nanotags measured by dynamic light scattering (DLS). (b) SEM micrograph showing the monodispersity and indicating average diameter is about 100 nm. The scale bars is 500 nm.

Figure 6.5 shows the illustrating of a hollow gold nanoparticle with PEG coating. It could be seem that the pegylation process is necessary to provide the steric stabilization for Raman nanotags. Moreover, the coating of PEG layer can greatly improve the biodistribution properties for *in vivo* biomedical applications. PEG is a linear hydrophilic molecule that is resistant to protein adsorption and cell adhesion(126). Because once opsonizing proteins absorb to nanoparticles to identify them as foreign particles and mark them for removal(127), then as the particles pass to the liver and spleen, the particles are sequestered in Kupffer cells(128). This process can take less than one hour to remove 60-70% of particles from blood circulation(127).

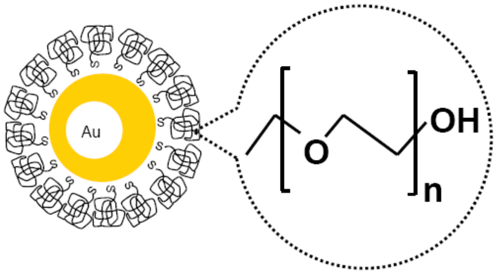

Figure 6.5 Illustrating hollow gold nanoparticle with PEG coating. Hollow gold nanoparticle is coated with polyethylene glycol (PEG) chains to prevent absorption of proteins.

6.2 Evaluation of Cytotoxicity of Raman Nanotags

Although both gold and PEG are biocompatible, Raman nanotags may still possess cytotoxicity caused by the leak of Raman reporter dyes, since the toxicity of the dyes is unknown. Therefore, it is important to evaluate the cytotoxicity of the hollow gold nanoparticle-based Raman nanotags.

6.2.1 Cell Maintenance

The PC-3 cell line, a human prostate cancer cell line, was obtained from the American Type Culture Collection (ATCC, Manassas, VA). Cells were maintained in GIBCO's T-medium supplemented with 5% FBS (fetal bovine serum), and 1X Penicillin/Streptomycin. Cells were incubated at 37^0C in a 5% CO_2 environment and were passed at 75 % confluence in P150 plates. The cultured PC-3 cells were harvested from monolayer using PBS and trypsin/EDTA, and suspended in T-media with 5 % FBS.

6.2.2 Cytotoxicity Study (MTT Assays)

Cytotoxicity evaluation of hollow gold nanoparticles was performed using MTT assays as described by Mosman(129). In this assay, only cells that are viable after 24 hours exposure to the hollow gold nanoparticles are capable of metabolizing a dye (3-(4,5-dimethylthiazol-2-yl)-2,5-diphenyltetrazolium bromide) efficiently and produce a purple colored precipitate which is dissolved in a detergent and analyzed. Approximately 3000 cells were seeded in a flat-bottomed 96-well polystyrene coated plate and were incubated for 48 hours at 37^0C in a 5% CO_2 incubator. The hollow gold nanoparticles with different coating (PEG only and Raman nanotags) were suspended in the T-medium. The concentration varied from 960, 480, 96 and 9.6 mM (total gold atom molar concentration). The hollow gold nanoparticles-loaded T-medium was added to the plate in hexaplets. After 24 hours of incubation, the T-medium was aspirated from each well and the cell layer was rinsed 2 times with complete growth T-medium and then 100 μL of growth T-medium and 10 μL of MTT reagent were added to each well and was further incubated for 4 hours. Formazan crystals formed after 4 hours in each well were dissolved in 100 μL of detergent, and after 24 hours, the absorbance of the formazan dye in each well was measured with a microplate reader (Molecular Device Spectra Max M5) at 565 nm. Wells with complete T-medium without cells and hollow gold nanoparticles were used as blanks. The viability results are shown in Figure 6.6.

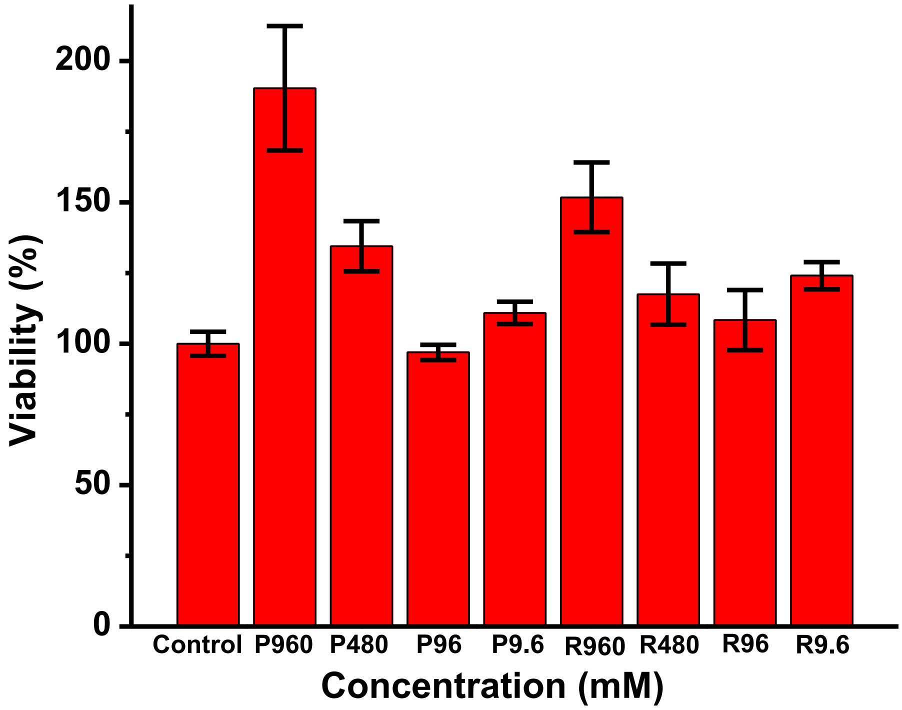

Figure 6.6 The MTT assays cell viability results. PC3 cells were cultured with pegylated hollow gold nanoparticles (without Raman dye, labeled with P) and Raman nanotags (labeled with R) with four different concentrations, 960, 480, 96, and 9.6 mM (total gold atom molar concentration).

The viability results are indicating a positive correlation between the concentration of nanoparticles and the cell viability. The results implied the non-toxic of hollow gold nanoparticles and promoted the growth of cells. These unusually results suggest that the MTT assays procedure need to be closely examined. The cell viability is measured based on the intensity of the absorbance of the formazan solution at a wavelength between 500 and 600 nm. However, our hollow gold nanoparticles also absorb light within this measurement range. The absorbance is most likely the add-up intensity from formazan and hollow gold nanoparticles themselves.

6.2.3 Cytotoxicity Study ([^{3}H]-Thymidine Incorporation)

In order to avoid the interference of hollow gold nanoparticles, cytotoxicity evaluation of hollow gold nanoparticles was performed using [^{3}H] Thymidine incorporation which is a measurement of DNA synthesis rate as a marker for cell proliferation. Approximately 3000 cells were seeded in a flat-bottomed 96-well polystyrene coated plate and were incubated for 24 hours at 37^{0}C in a 5% CO_2 incubator. The hollow gold nanoparticles with different coating (PEG only and Raman nanotags) were suspended in the T-medium. The concentration varied from 960, 480, 96, and 9.6 mM. The hollow gold nanoparticles-loaded T-medium was added to the plate in hexaplets. After 24 hours of incubation of cells and nanoparticles, the T-medium was aspirated from each well and the cell layer was rinsed 3 times with complete growth T-medium and then [^{3}H] thymidine solution (1 µCi/100 µl T-medium) was added to each well. After 2 hours incubation, the medium was aspirated from each well and the cell layer was rinsed 3 times with complete growth T-medium. The cells were then solubilized with 100 µl of 2 N NaOH solution. The solution was collected from wells to the scintillation vials which already filled with 5 mL of Budget-Solve Complete Counting Cocktail. Finally, [^{3}H] thymidine incorporated into DNA was quantified by Liquid Scintillation β-Counter (Beckman LS 6500). The viability results are shown in Figure 6.7.

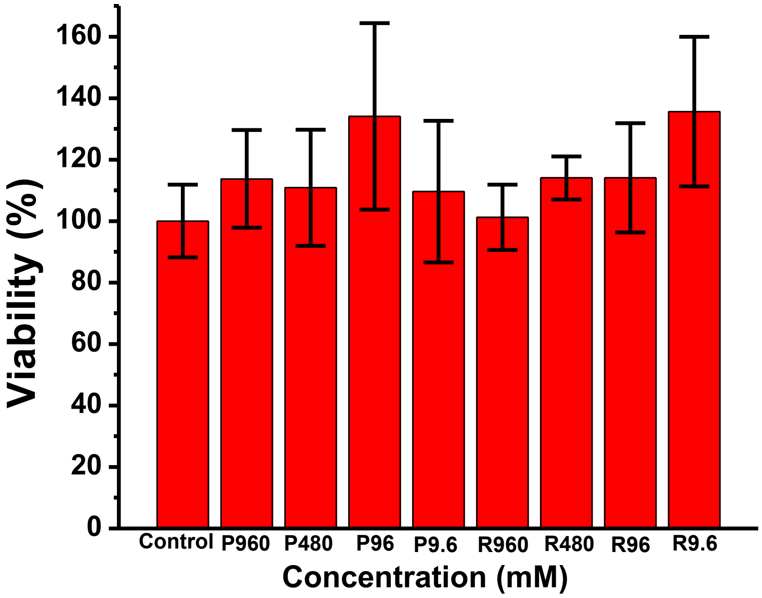

Figure 6.7 The [^{3}H]-Thymidine incorporation viability results. PC3 cells were cultured with pegylated hollow gold nanoparticles (without Raman dye, labeled with P) and Raman nanotags (labeled with R) with four different concentrations, 960, 480, 96, and 9.6 mM (total gold atom molar concentration).

Statistically, the treated cells showed the same viability as the control. This method eliminated the false increasing viability trend with nanoparticle concentration, which was evidently resulted from the influence of hollow gold nanoparticles in the MTT assays. The result demonstrated that the MTT methods not suitable for gold nanoparticle cytotoxicity evaluation and the hollow gold nanoparticles-based Raman nanotags have no toxicity to PC-3 cells. These results clearly demonstrated that the nontoxic Raman nanotags can be used for the future *in vitro* and *in vivo* study.

6.3 Heat Generated by Gold Nanoparticles

Gold nanoparticles absorb electromagnetic radiation strongly around their SPR frequency(27, 130). A consequence of the strong absorption of radiation associated with the

SPR is heat generation. Three sequential processes are involved in heat generating (131). First, electrons on the nanoparticles oscillate under the influence of the incident electromagnetic field. Second, the photon energy is transferred to the electrons by interband transition. During this process, the internal electron energy redistribution by electron-electron scattering, the free carrier is easily heated up to thousands of Kelvin. While keeping the metal lattice temperature relatively low since its heat capacity is one to two orders of magnitude larger than the electron one. This strong electron temperature rise induces the modification of their Fermi-Dirac distribution and consequently creates the hot electron. In the relaxation process of electrons, the energy is transferred to the lattice via electron-phonon interaction. Finally, through phonon-phonon interactions at the lattice, nanoparticles transfer heat to the surrounding medium. The relaxation times of electrons-phonon interactions and phonon-phonon interactions have been measured to be on the picoseconds scale(48, 132, 133). Here, we performed a simple calculation to estimate the heat-generating efficiency of gold nanoparticles under the illumination of light.

6.3.1 Heat Generated by Spherical Gold Nanoparticles

In the absence of phase transformations, heat transfer in a system with nanoparticles is described by the usual heat transfer equation:

$$\rho(r)c(r)\frac{\partial T(r,t)}{\partial(t)} = \nabla k(r)\nabla T(r,t) + Q(r,t) \tag{6-1}$$

where T(r,t) is temperature as a function of coordinate r and time, ρ(r), c(r) and k(r) are the mass density, specific heat, and thermal conductivity, respectively.

In the steady–state, the temperature distribution T(r) generated by the heating power density distribution Q (r) is governed by the Poisson equation:

$$k_0\nabla^2 T(r) = -Q(r) \tag{6-2}$$

where k =(318 W/m·K) is the thermal conductivity of gold. A dimensional analysis of this equation permits to estimate the expected temperature spatial variation δT throughout the structure.

$$\delta T \sim \frac{l^2 Q}{k_0 V_{NP}} \tag{6-3}$$

where ꞁ is the typical spatial dimension of the structure, and V_{NP} is the volume of a single nanoparticle. For a very small spatial dimension of the system, the thermal diffusion is so fast that, even though the heating power density undergoes strong spatial variations; the temperature diffuses quickly and remains almost uniform. The temperature increase depends on how efficient the thermal diffusion through the surroundings, which is characterized by its thermal conductivity k_0 (=0.6 W/m K for water). In the steady–state, the Poisson equation ($k_0\nabla^2 T(r) = 0$) is easy to solve analytically with spherical symmetry with boundary condition: r → ∞; T = Ta and r → R_{NP}; T = T_R, where r is the distance away from sphere center and Ta is the temperature at the distance of r. R_{NP} is the radius of nanoparticle and T_R is the temperature of the surface of nanoparticle. The temperature profile simply gives

$$T = (T_R - T_a)\frac{R}{r} + T_a \tag{6-4}$$

Using Fourier's law and differentiating the temperature profile, the heat flux is

$$q = -k_0 \frac{dT}{dr} = k_0(T_R - T_a)\frac{R}{r^2} \tag{6-5}$$

The rate of heat dissipation Q is

$$Q = q \times 4\pi r^2 = 4\pi r^2 k_0 (T_R - T_a)\frac{R}{r^2} \tag{6-6}$$

The maximum temperature increase occurs on the surface of nanoparticle.

$$\Delta T_{max} = \frac{V_{NP}Q}{4\pi k_0}\frac{1}{R} \qquad (6\text{-}7)$$

where k_0 is the thermal conductivity of water (0.561 $W\cdot K^{-1}\cdot m^{-1}$).

The local heat intensity Q(r,t) comes from light dissipation in gold nanoparticles:

$$Q(r,t) = < j(r,t) \bullet E(r,t) >_t = -\frac{1}{2}\mathrm{Re}[i\omega\frac{\varepsilon(r) - 1}{4\pi}\tilde{E}(r)\tilde{E}^*(r)] \qquad (6\text{-}8)$$

where j(r,t) is the current density, $E(r,t)=\mathrm{Re}[\tilde{E}(r)e^{-i\omega t}]$ is the resulting electric field in the system and ε(r) is the dielectric constant. Here was assumed that the system is excited with the external laser field $E_0(t)=\mathrm{Re}[\tilde{E}_0(r)e^{-i\omega t}]$. If light is turned on at t=0, the light intensity is given by $I(t) = I_0 = cE_0^2\sqrt{\varepsilon_0}/8\pi$ for t > 0 and 0 at t < 0. Here, ε_0 is the dielectric constant of medium (for water ε_0 = 1.8).

To calculate the local heat Q, we used the equation (6-9) for $r < R_{NP}$.

$$\tilde{E}(r)= [\frac{3\varepsilon_0}{2\varepsilon_0 + \varepsilon(\omega)}]E_0 \qquad (6\text{-}9)$$

The rate of heat dissipation Q depends on the induced electric field inside gold nanoparticle and is given by the equation:

$$Q= -\mathrm{Re}\,[\, i\omega\frac{\varepsilon(\omega)- 1}{8\pi}E_0^2|\frac{3\varepsilon_0}{2\varepsilon_0+\varepsilon(\omega)}|^2\,] \qquad (6\text{-}10)$$

The maximum temperature increase occurs at $r = R_{NP}$:

$$\Delta T_{max}(I_0)= \frac{R_{NP}^2}{3k_0}\mathrm{Re}\left[\, i\omega\frac{1- \varepsilon(\omega)}{8\pi}|\frac{3\varepsilon_0}{2\varepsilon_0+ \varepsilon(\omega)}|^2\right]\frac{8\pi I_0}{c\sqrt{\varepsilon_0}} \qquad (6\text{-}11)$$

where I_0 is the light intensity inside the medium. Figure 6.8 show calculated $\Delta T_{max}(I_0, R_{NP})$ using the dielectric constant of bulk gold (43). We see from Equation 6-11 that in order to achieve a visible heating effect of a few K for typical light fluxes 10^3-10^6 W/cm^2 one should use nanoparticles of relatively large radius (≥ 10 nm). If the light intensity flux is given by the illumination power (P) of 25 mW and the laser-spot diameter of 4 μm ($A= \pi r^2$), we can obtain light fluxes (I_0 = P/A) about 10^5 W/cm^2. Note that these calculations were made the bulk gold dielectric constant, and they do not include-quantization effects. These estimates are valid for the solid spherical gold nanoparticles. Therefore, in the case of hollow gold nanoparticles, the different approach has to be made which was covered in the next section.

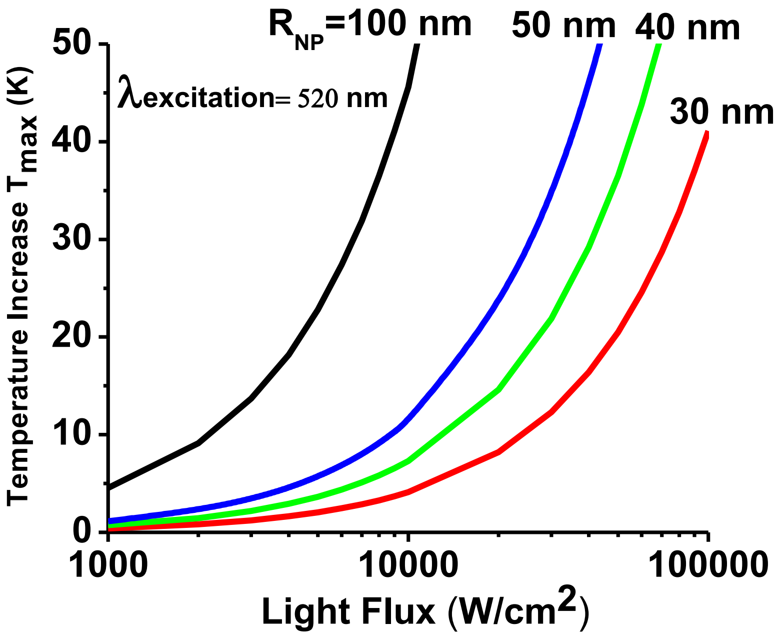

Figure 6.8 Calculated temperature increase at the surface of gold nanoparticle in the water as a function of illumination power. The graph is given at the excitation wavelength 520 nm. The medium is water with ε_0 = 1.8(27).

6.3.2 Heat Generated by Hollow Gold Nanoparticles

The FDTD simulation was used to calculate absorption and scattering efficiency of hollow gold nanoparticles. Q_{sca} (scattering cross-section, C_{sca}, divided by geometric cross-section area), Q_{abs} (absorption cross-section, C_{abs}, divided by geometric cross-section area), and extinction efficiency, Q_{ext} ($Q_{ext} = Q_{sca} + Q_{abs}$). Hollow gold nanoparticle with a fixed outer R_2 and inner radius R_1, (R_1, R_2) = (25, 50) nm, but different surface roughness, smooth surface, with a roughness of 5 nm and with a roughness of 8 nm were simulated. The hollow gold nanoparticles were simulated as a suspension in water. Simulations were performed on each hollow gold nanoparticle between wavelengths of 400 and 1000 in 3 nm increments. This range of wavelengths was chosen as they include the surface modes for all particle geometries and hence include the dominant absorption peaks.

In order to discard the volume effect mentioned above and to focus on the morphology effects, all the structures are assigned a common volume $v = (4\pi R_{NP}^3/3)$, where the outer radius R_{NP} is fixed at 50 nm. Temperature distribution outside the nanoparticle is given by a simple equation:

$$\Delta T_{max} = \frac{Q}{4\pi k_0}\frac{1}{R_{NP}} \tag{6-12}$$

where k_0 is the thermal conductivity of water (0.6 W/K·m); Assuming that all the energy absorbed from the incident light is converted to thermal energy, then under steady-state condition the power absorbed by a single particle is

$$Q = C_{abs} \times I_0 \tag{6-13}$$

And absorption efficiency Q_{abs} is

$$Q_{abs} = \frac{C_{abs}}{\pi R_{NP}^2} \tag{6-14}$$

where Q is the heat transfer rate (W), C_{abs} the absorption cross-section, Q_{abs} is the absorption efficiency, and I_0 is the light intensity (W/cm^2). By injecting Equation (6-13) into Equation (6-12), the maximum temperature increase on the surface of hollow gold nanoparticle gives

$$\Delta T_{max} = \frac{R_{NP}}{4k_0} \times Q_{abs} \times I_0 \tag{6-15}$$

It was assumed that the wavelength of this laser could be tuned to the wavelength of maximum absorption of hollow gold nanoparticles. The surface roughness of hollow gold nanoparticle is the dominating factor on the wavelength at which maximum absorption occurs as shown in Figure 6.9. For hollow gold nanoparticle with an outer radius 50 nm, the optimum absorption efficiency of $Q_{abs} \approx 8$ occurs at 730 nm with a roughness of 8 nm on the surface. For spherical gold nanoparticle with a radius 50 nm and smooth surface, the peak absorption efficiency is almost a factor of 8 smaller, $Q_{abs} \approx 1$. Figure 6.10 shows calculated temperature increase ΔT_{max} using the absorption efficiency obtained from FDTD simulation results. For the spherical gold nanoparticle investigated above, we found that the temperature increase is $\Delta T_{max} = 20$ K at $I_0 = 10^5$ (W/cm^2), which is of the order of magnitude reported in literature (134).

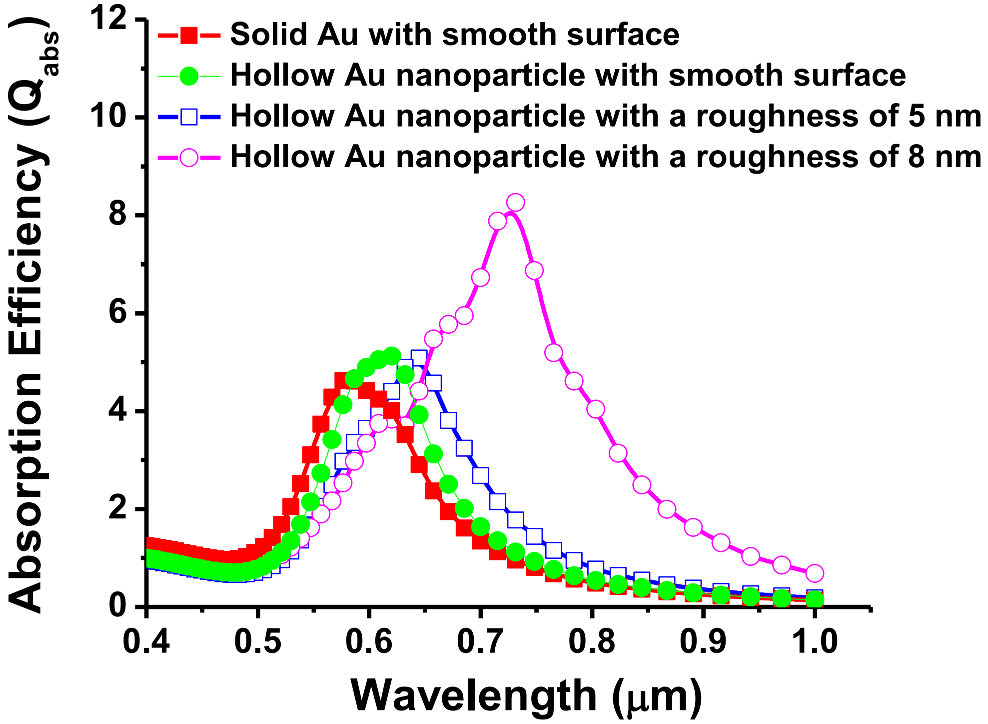

Figure 6.9 The absorption efficiency, Q_{abs}, of hollow gold nanoparticle with the same inner radius R_1 and outer radius R_2, (R_1, R_2)=(25, 50) nm but different surface roughness (smooth surface, 5 nm roughness and 8 nm roughness). The solid gold nanoparticle with a radius 50 nm and smooth surface is also shown for comparison.

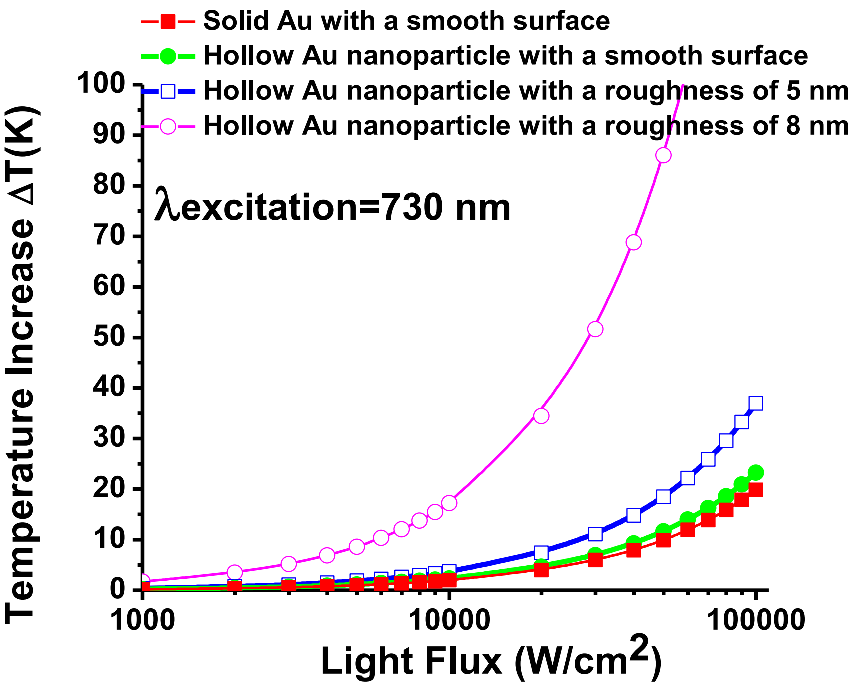

Figure 6.10 The calculation of temperature increase on the hollow gold nanoparticle surface as a function of illumination power. Hollow gold nanoparticle with the same inner radius R_1 and outer radius R_2, $(R_1, R_2)=(25, 50)$ nm but different surface roughness (smooth surface, 5 nm roughness and 8 nm roughness). The solid spherical gold nanoparticle with a radius 50 nm and smooth surface is also shown for comparison. The graph is given at the excitation wavelength 730 nm.

6.3.3 Photothermal Effect in Tissue-Like Phantom

We investigated the photothermal effect in tissue-like phantom under the NIR laser irradiation. Gel phantoms were prepared using 1% Intralipid, gelatin powder and paraformaldehyde to mimic tissue optical properties. Briefly, 2400 mg of highly purified gelatin powder was mixed with 228 mL of deionized water and heated by microwave for 2–4 minutes (~90^0C) with intermittent mixing until the gelatin was dissolved and the solution appeared clear and colorless. With continuous mixing at room temperature, the gelatin solution was permitted to cool to 60^0C at which time 12 mL of Intralipid (20% fat emulsion) and paraformaldehyde were added, which caused the solution to become white and opaque. The tissue phantom had a thin pocket in which 50 μL hollow gold nanoparticles (3.0×10^9/mL) suspension with SPR peak center at 750 nm was pipetted. A laser fiber was placed inside that pocket in touch with the suspension in that pocket. The diode laser with a mean wavelength of 810 nm was centered to the cavity and the temperature change was recorded by thermometer. The temperature change was recorded as a function of distance and as a function of time. Figure 6.11 illustrates the experimental setup.

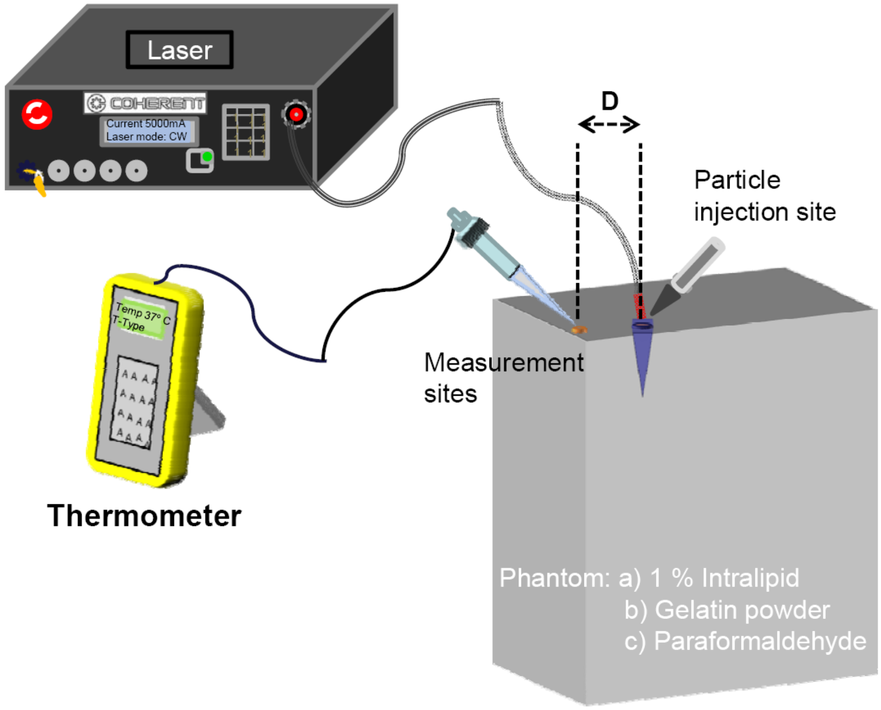

Figure 6.11 (a) Illustration of the experimental setup of phantom embedded with hollow gold nanoparticles suspension, focused laser beam, and temperature recorder.

Heating was provided by the irradiation of 50 µL hollow gold nanoparticles (3.0×10^9/mL) with a 810 nm NIR diode laser for 1 minute at power density 5 W/cm^2. With 1 minute irradiation time, the temperature alternation rise to 23, 13, and 8 degrees at distance 1, 3 and 4 mm away from irradiation point, respectively. It is necessary to note that 810 nm laser radiations was also absorbed by water, and the temperature alternation of background (water) rise to 12, 7, and 5 degrees at distance 1, 3, and 4 mm away from irradiation point, respectively. The results are shown in Figure 6.12. In this experiment, it shows very promising capability of heat-generating by hollow gold nanoparticles.

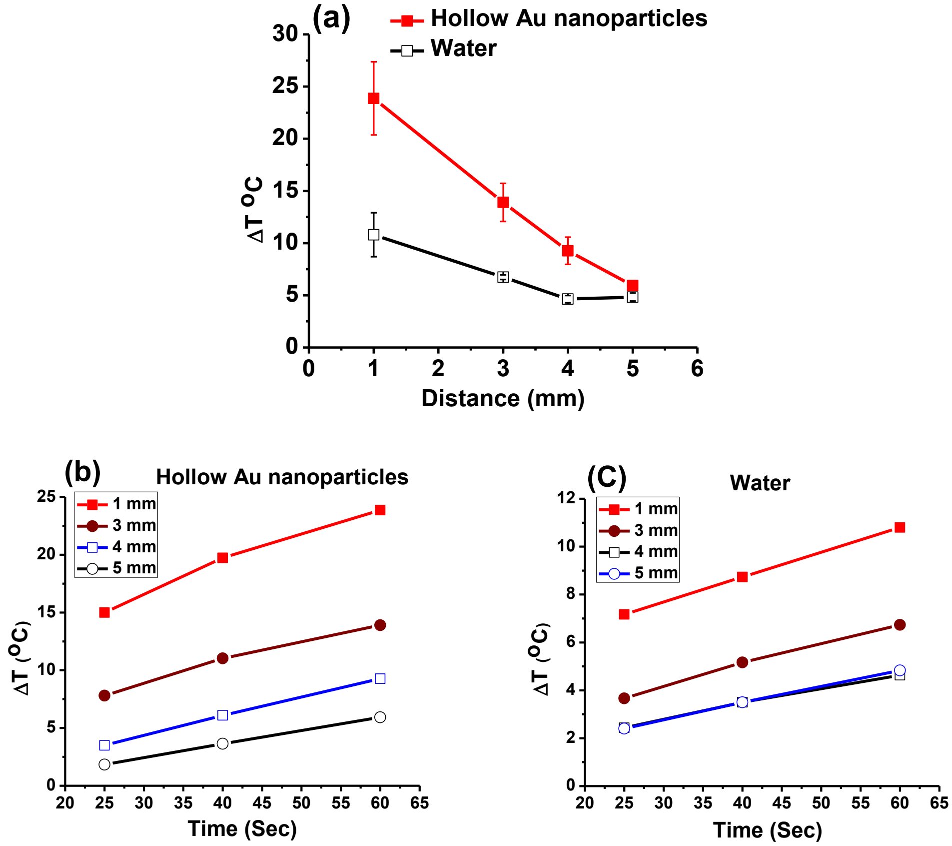

Figure 6.12 The comparisons of the temperature increase between hollow gold nanoparticles and background (water) (a) shows the temperature increase at different measuring distance from the irradiation point with a irradiation time 60 seconds, (b) and (c) show the temperature increase recorded at different time point for hollow gold nanoparticles and water, respectively.

6.3.4 Photothermal Effect Recorded by Infrared Focal Plane Array Camera

Heating of hollow gold nanoparticles under the irradiation of near infrared laser light with a wavelength 800 nm was measured using an infrared focal plane array camera (FLIR model SC6000, 640×513 pixels, 25 μm pitch) with detection window of 8-9.6 μm. Any object above 0 °K will radiate electromagnetic energy with spectrum peak and intensity dependent on temperature and emissivity of the object. Reported temperature increase of suspended gold nanoparticles due to the photothermal effect has been measured using thermocouples. The accuracy of the temperature change with thermocouples is questionable since the stray infrared (IR) light (direct and scattered) can heat the bi-metallic thermocouple probe. Our experiments utilizing thermocouples for measuring temperature increase indicates that the direct and scattered light (visible and NIR) heat up the thermocouple. Moreover, another major limitation of using thermocouple is that only limited spatial sites can be probed and therefore a complete spatial heat profile cannot be measured.

The setup for photothermal induced temperature increase measurement consist of a infrared camera and the cuvette filled with two kinds of gold suspensions, solid spherical gold nanoparticles with a diameter 80 nm (1.0×10^{10}/mL) and hollow gold nanoparticles with an inner diameter 50 nm and an outer diameter 100 nm (1.0×10^{10}/mL). The cuvette was placed at the focal plane of the camera lens, and collimated laser light incident at the center of the cuvette. The image acquisition rate is set at 1 frame/s. Image acquisition is initiated with the illumination of the gold suspension with the laser light. The incident laser power is 350 mW and the diameter of the collimated Gaussian beam is 3 mm. The incident light flux at the gold suspension is 1.2 W/cm^2. The gold suspensions were illuminated with laser light for 10 minutes. Image sequences of the photothermal temperature increase in water and gold nanoparticles were recorded for 30 minutes. Assigning a temperature value to measured intensity value of infrared radiation for each image pixel requires calibration. The calibration was carried out by recording images of a cuvette though with water was circulated from a water bath that was being heated. A thermocouple placed in the water bath measured the temperature continuously in synchronization with the image acquisition. Figure 6.13 shows the infrared absorbance image of the cuvette filled with hollow gold nanoparticles. The maximum temperature increase occurred at the center of the cuvette. Compared to the solid spherical gold nanoparticle, the temperature increase for the hollow gold nanoparticle is significant as shown in Figure 6.14.

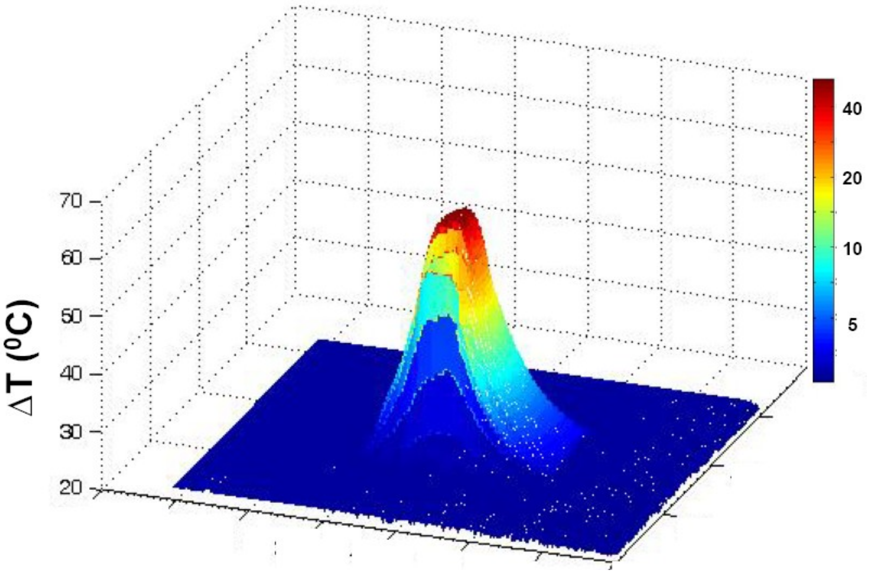

Figure 6.13 Infrared absorbance image of the cuvette filled with hollow gold nanoparticles under the irradiation of infrared light for 10 minutes. The maximum temperature increase occurred at the center of the cuvette.

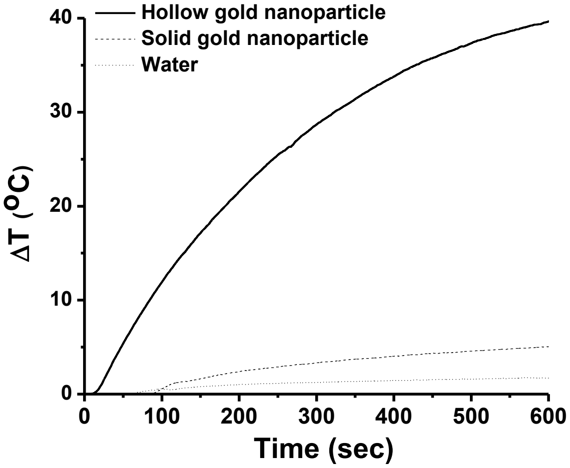

Figure 6.14 The comparisons of the temperature increase of solid gold nanoparticles, hollow gold nanoparticles and background (water).

6.4 Trapping Iron Oxide Nanoparticles inside Hollow Gold Nanoparticles

In recently years, integrating superparamagnetic iron oxide nanoparticles (SPIONs) with gold nanoparticles to form a composite multifunctional nanoparticle has attract considerable attention(30, 32, 33, 135). To date, the effort has been mostly limited on coating iron oxide articles with a thin layer of gold, where the gold shell not only provides convenient anchorage sites for functionalization of bimolecular through the well-established Au-thiol conjugation procedure but also protects SPIONs from dissolution and aggregation. However by such an approach, it is difficult to tune the SPR wavelengths to the NIR region. Reported core/shell nanoparticles usually have their SPR in the visible light range, which limits their plasmonic functions for *in vivo* biomedical applications.

We demonstrated another approach to construct Fe_3O_4/Au core/shell nanoparticles by trapping iron oxide nanoparticles into the hollow interior of hollow gold nanoparticles. Such nanoparticles are strongly magnetic with their SPR peaks in the NIR region.

6.4.1 Experiment

The trapping process started from synthesizing porous hollow gold nanoparticles (PHAuNPs) which has been mentioned in chapter 4. A modification was made to produce a porous shell instead of a smooth one. In this case, the pH value of the electrolyte was adjusted with 0.2 M sodium sulfite (pH~10) to reach a pH~6.5, and the deposition time was controlled in the range of 400 to 600 seconds. Synthesized PHAuNPs feature a sub-25 nm shell with a 50 nm hollow core. The shell is of porous nature with the pore size about 2-3 nm, as measured in the high resolution transmission electron microscopy (HRTEM) image shown in Figure 6.15. These nanoscale pores in the shell allow ions (Fe^{2+} and Fe^{3+}) to diffuse.

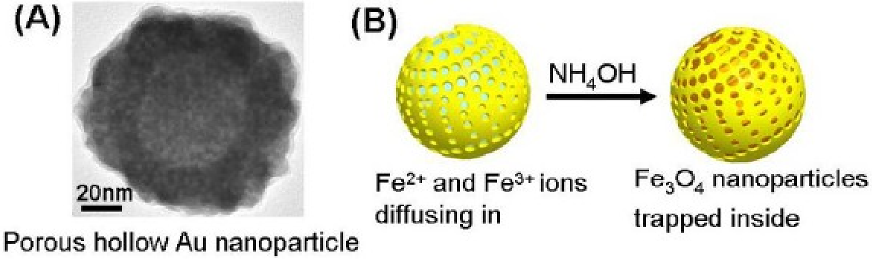

Figure 6.15 (A) HRTEM micrograph of a PHAuNP showing the hollow core and the porous shell with pore size about 2-3 nm. (B) Schematic illustration of trapping Fe_3O_4 nanoparticles inside a PHAuNP.

The iron oxide nanoparticles were produced by co-precipitation method(136). Briefly, anhydrous 5.2 g $FeCl_3$ (0.032 mol) and 2g $FeCl_2$ (0.016mol) were mixed to 25 ml of deionized water containing 0.85 mL of 12.1 N HCl under vigorous stirring. The above aqueous solution was delivered into the alumina membrane channels through the vacuum filtration process. Then, the wetted alumina membrane was transferred into 5 mL of 0.5 % NH_4OH solution for an additional 10 minutes. The yellow-orange color formed which indicates the formation of iron oxide nanoparticles. The free iron oxide nanoparticles (~10 nm) formed inside the alumina membrane were pre-filtrated out using a typical vacuum filtration procedure. The Fe_3O_4/Au core/shell nanoparticles were released into deionized water with the dissolution of alumina membrane using 1M NaOH solution. The nanoparticles were cleaned by several cycles of dispersion in deionized water followed by centrifugation.

6.4.2 Characterization of Fe_3O_4/Au Core/Shell Nanoparticles

Figure 6.16 shows TEM analysis before and after loading of iron oxide nanoparticles. After loading, the hollow core of PHAuNPs is occupied by solid substances. During the precipitation, Fe_3O_4 nanoparticles also formed outside of PHAuNPs, but TEM micrographs clearly show that no small iron oxide nanoparticles were attached to the PHAuNP surface. This is in agreement with the common notion that iron oxide usually does not stick to the gold surface(137). Given the very different sizes of PHAuNPs (~100 nm) and non-trapped Fe_3O_4 nanoparticles (< 20 nm); they can be readily separated using filtration and centrifugation.

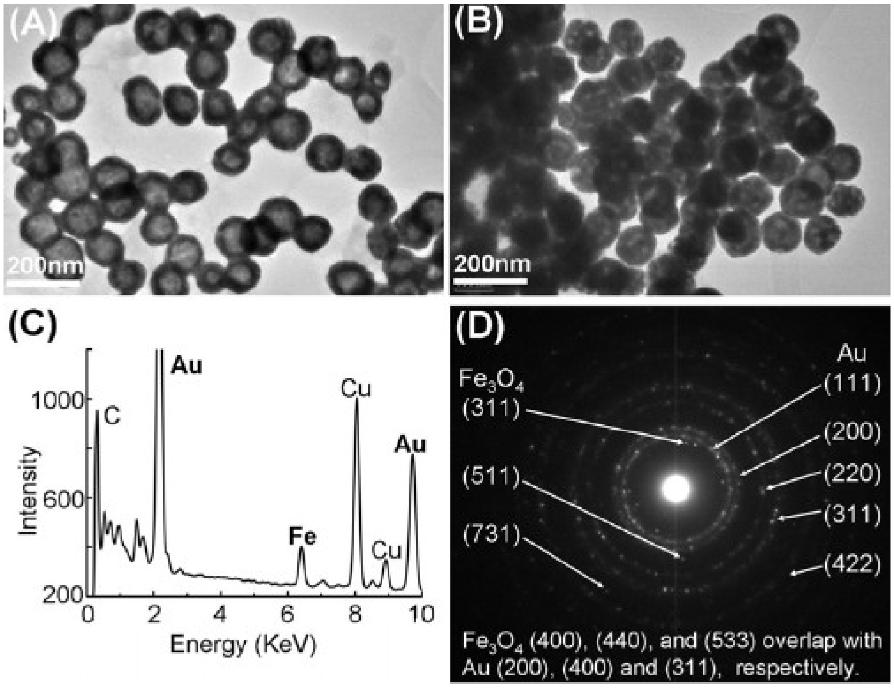

Figure 6.16 TEM micrographs of PHAuNPs before (A) and after (B) loading iron oxide nanoparticles. (C) EDS spectrum of one single particle, showing the coexistence of gold and Fe.(D) SAED pattern from three particles, showing a superposition of Au and Fe_3O_4 lattices.

The loading of Fe_3O_4 to the core of PHAuNPs was confirmed by energy dispersive X-ray (EDS) analysis of a single particle and the selected area electron diffraction (SAED) pattern from three particles. EDS shows the co-existence of Au and Fe in a single particle as shown in Figure 6.16 (C), and Cu peak is from the TEM grid. The low intensity of Fe is due to the shield effect of the thick gold shell. The SAED pattern is a superposition of Au and Fe_3O_4 lattices showing three distinguishable planes of (311), (511) and (731) from Fe_3O_4 as shown in Figure 6.16 (D). Other Fe_3O_4 planes overlap with Au planes.

In Figure 6.15 (a) is the appearance of a bottle of particle water suspension. The cyan color indicates that the suspension absorb red light. The absorption spectrum is shown in Figure

6.17 (b), which has a broad peak centering at 750 nm. This absorption peak corresponds to the SPR wavelength. Compared to PHAuNPs before loading iron oxide, the absorption spectrum shows little change. For core/shell nanoparticles, it is well known that the SPR wavelength is dependent on the refractive indices of medium, shell and core. Changing core material usually causes a shift of the SPR wavelength. However, PHAuNPs have a relatively thick shell (>20 nm). It has been shown in section 5.4 that at this thickness the core has little effect on the SPR wavelength. Therefore, the loading of iron oxide into the core does not change the overall optical properties of these nanoparticles. We have also proved in chapter 5 that the red-shift of the SPR peak to the NIR region mainly arises from the roughness of the PHAuNP surface. Such an observation indicates - it is possible to maintain the optical properties of PHAuNPs even after the loading of iron oxide. As shown in Figure 6.17 (a), the particles can be dragged towards a permanent magnet, unequivocally indicating the magnetic characteristics of the gold nanoparticles.

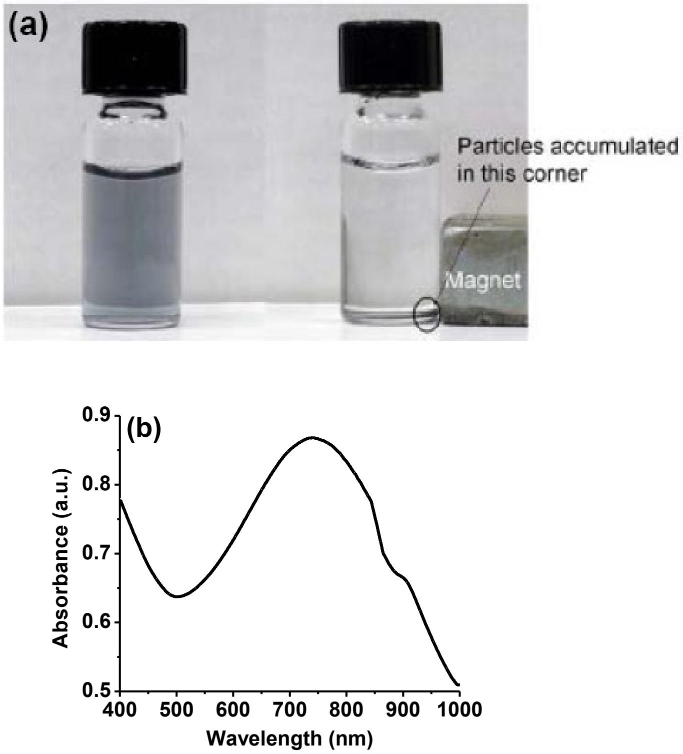

Figure 6.17 The plasmonic and magnetic properties of the Fe_3O_4-loaded PHAuNPs. (a) Appearance of a bottle of particle water suspension. The particles can be dragged towards a permanent magnet. (b) Absorption spectrum of the particle water suspension, showing a broad peak centering at 750 nm.

Hysteresis loop of dried particle powder is shown in Figure 6.18. Since the inside Fe_3O_4 nanoparticles are believed to be smaller than 20 nm, we expect to see a typical superparamagnetic behavior: zero remanence, zero coercivity and a large saturation field. The small hysteresis shown in the measurement may reflect the presence of some large Fe_3O_4 nanoparticles (> 30 nm) inside PHAuNPs. Given the size of the hollow space (> 50 nm) and the thickness of the porous shell (25 nm), the inward diffusion of OH^- ions may be partially obstructed resulting in a much slower nucleation rate. As such, the inside particles could grow large. The measured high saturation field is inconsistent with the superparamagnetic characteristic. This suggests a mixture of superparamagnetic and ferromagnetic nanoparticles. Ferromagnetic nanoparticles are usually undesirable for biomedical applications because of their agglomeration caused by magnetic attraction. However, for iron oxide nanoparticles loaded PHAuNPs, the thick Au shell can effectively separate them far apart to avoid such magnetic aggregation.

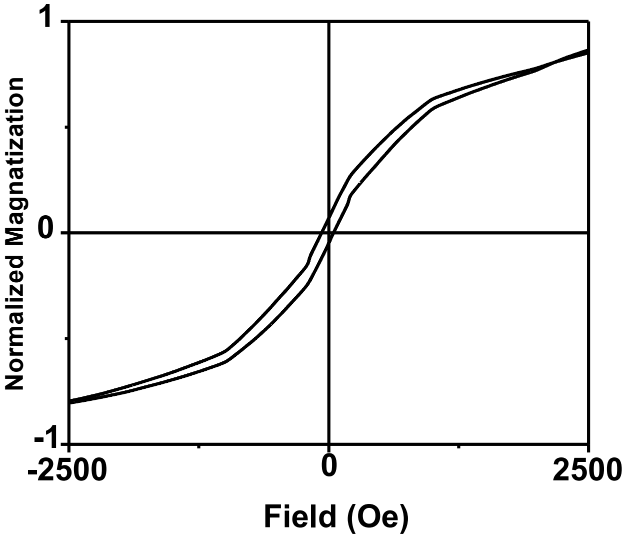

Figure 6.18 Hysteresis loop of dried particle powder, showing that the suspension consists of a mixture of superparamagnetic and ferromagnetic nanoparticles.

Because the resulted composite nanoparticles combine the desirable magnetic and plasmonic properties into one nanoentity, they are particularly suitable for *in vivo* diagnostic and therapeutic applications, where the gold surface provides anchorage sites for attachment of functional molecules and the particles can be activated by both NIR light and magnetic field.

CHAPTER 7

CONCLUSION

The electrochemically evolved hydrogen bubbles can serve as templates and reducing agents for the synthesis of hollow gold nanoparticles. In this thesis, we seek to understand the formation mechanism and plasmonic properties of hollow gold nanoparticles that are expected to be used for *in vivo* biomedical applications.

The Ag stripes were pattered lithographically on the glass slide and served as substrate to study the formation mechanism of hollow gold nanoparticles. The electrochemically evolved hydrogen nanobubbles were generated when the applied potential is more negative than the equilibrium of hydrogen evolution potential. The hydrogen nanobubbles served as the templates and reducing agents for the formation of hollow gold nanoparticles through the electroless reaction with sodium gold sulfite electrolyte. The formation mechanism of hollow gold nanoparticles can be described in three stages: (I) hydrogen nanobubbles were generated electrochemically; (II) Au^+ ions were reduced to become metallic gold clusters at the boundary of hydrogen nanobubbles; (III) metallic gold clusters act as autocatalyst to trigger the Au^+ ion s disproportionation reaction or the hydrogen nanobubbles act as catalyst to trigger the Au^+ ions disproportionation reaction. The additives of EDA and Ni^{2+} ions are the key components for the formation of hollow gold nanoparticles. EDA has the capability to increase the stability of gold sulfite electrolyte and clean surface oxides of electrode to enhance hydrogen evolution efficiency. The electrodeposited Ni metal on the electrode promoted hydrogen evolution efficiency, therefore improved the size distribution of hollow gold nanoparticles.

Alumina membranes were used to capture the electrochemically evolved hydrogen nanobubbles, and subsequently to generate a large number of hollow gold nanoparticles inside the membranes. Hydrogen nanobubbles with a radius of about 25 nm were captured by electroless deposition of gold on the inner wall surface of channels inside alumina membranes, and hollow gold nanoparticles with a complete nanocrystalline shell and a 50 nm hollow core also were fabricated in the alumina membrane. The particle size can be varied from 100 nm to 150 nm by controlling the shell thickness in terms of the deposition time. The more complicate nanostructure “nanomatryoshka” were fabricated by using pulse potential route to manipulate the nanobubble formation process. The surface roughness of hollow gold nanoparticles can be tuned from smooth to very rough by adjusting the pH (from 6.0 to 7.0) of the electrolyte.

FDTD simulation confirmed that the red-shifts of SPR peaks are mainly caused by the surface roughness of hollow gold nanoparticles and the hollow nature of these nanoparticles play only a minor role. The SPR peaks can be tuned into the NIR region by roughing the surface of nanoparticles. This unique SPR tuning mechanism provides an easy route to produce suitable hollow gold nanoparticles for *in vivo* biomedical applications.

The pegylated Raman dye encoded hollow gold nanoparticles, Raman nanotags, have demonstrated the enhancement of Raman signal. Cytotoxicity evaluation using [^{3}H] thymidine incorporation method has also shown non-toxicity of the Raman nanotags. The calculations estimating the heating efficiency of hollow gold nanoparticles have shown that the temperature increase on the surface of hollow gold nanoparticles can be increased dramatically with the roughened surface. The photothermal effects of hollow gold nanoparticles have been examined by two methods: (1) by embedding hollow gold nanoparticles in tissue-like phantom environment; (2) by recording infrared images as temperature increase. The results show that hollow gold nanoparticles are capable to generate sufficiency heat to ablate the cancer cells. Using the nanocontainers of hollow gold nanoparticles as carriers has been demonstrated by trapping iron oxide nanoparticles inside the hollow interior. These Fe_3O_4/Au core/shell nanoparticles exhibited two desirable properties, magnetic and plasmonic that can be applied to *in vivo* biomedical applications. All these experimental results strongly propose that the optical tunable Raman nanotags and magnetic Fe_3O_4/Au core/shell nanoparticles can be used as diagnostic agents for the cancer cell imaging and as therapeutic agents for the photothermal cancer ablation.

APPENDIX A

MATLAB SCRIPT OF HEAT GENERATED BY OPTICAL DRIVE SOLID GOLD NANOPARTICLES

```
r = 50E-7  % Radius of Solid gold Nanoparticle Unit: cm
E0= 1.8;  % Dielectric Constant of the surrounding Medium (Water)
c = 3.0E10 ; % Speed of Light Unit: cm
E2 = (0.58/100)*1000; % Thermal Conductivity of Water Unit: w/(k·cm)
I = [1000 2000 3000 4000 5000 6000 7000 8000 9000 10000 20000 30000 40000 50000 60000
70000 80000 90000 100000] % Light Intensity Unit: w/cm^2
n = -16.5028;  % Real Part of Bulk gold Dielectric Constant
k = 1.0594;  % Imaginary Part of Bulk gold Dielectric Constant
d = 2.69279E+15;  % Frequency of Light
Em = n+k*I; % Dielectric Constant of bulk gold at Wavelength 520 nm
a = (r*r)/(3*E2)
a1= d/(8*pi)
a2 = (abs((3*E0)/(2*E0+Em)))^2
a3= (8*3.14.*I)/(c*sqrt(E0))
a4 = imag(Em).*a3
T = a*a1*a2*a4*1000; % Temperature Increased Unit: K
hold on
plot(I, T)
hold off
save heating-01.xls A -ascii
```

APPENDIX B

MATLAB SCRIPT OF HEAT GENERATED BY OPTICAL DRIVE HOLLOW GOLD NANOPARTICLES

```
r = 50E-9; % Radius of Hollow gold Nanoparticle Unit: m
E2 = 0.6 ; % Thermal Conductivity of Water Unit: W/K·m
I = [1000 2000 3000 4000 5000 6000 7000 8000 9000 10000 20000 30000 40000 50000 60000 70000 80000 90000 100000]; % Light Intensity Unit: w/cm^2
ab = 0.95213; % Absorption Efficiency of Hollow Gold Nanoparticle with Smooth Surface and has an Outer radius R= 50nm and inner Radius r= 25 nm Suspend in Water
T = [r/(E2*4)]*ab*I*10000 % Temperature Increased Unit: K
A = [I, T];
hold on
plot(I, T)
hold off
save heating-01.xls A -ascii
```

REFERENCES

1. Oldenburg SJ, Westcott SL, Averitt RD, & Halas NJ (1999) Surface enhanced Raman scattering in the near infrared using metal nanoshell substrates. *Journal of Chemical Physics* 111(10):4729-4735.
2. Kerker M, Wang DS, & Chew H (1980) Surface Enhanced Raman-Scattering (Sers) by Molecules Adsorbed at Spherical-Particles. (Translated from English) *Applied Optics* 19(24):4159-4174 (in English).
3. Olofsson L, Rindzevicius T, Pfeiffer I, Kall M, & Hook F (2003) Surface-based gold-nanoparticle sensor for specific and quantitative DNA hybridization detection. *Langmuir* 19(24):10414-10419.
4. Chen J*, et al.* (2005) Gold nanocages: Bioconjugation and their potential use as optical imaging contrast agents. *Nano Letters* 5(3):473-477.
5. Gobin AM*, et al.* (2007) Near-infrared resonant nanoshells for combined optical imaging and photothermal cancer therapy. *Nano Letters* 7(7):1929-1934.
6. Huang XH, El-Sayed IH, Qian W, & El-Sayed MA (2006) Cancer cell imaging and photothermal therapy in the near-infrared region by using gold nanorods. (Translated from English) *Journal of the American Chemical Society* 128(6):2115-2120 (in English).
7. Jain PK, El-Sayed IH, & El-Sayed MA (2007) Au nanoparticles target cancer. *Nano Today* 2(1):18-29.
8. faraday M (1857) The Bakerian Lecture: Experimental Relations of Gold (and Other Metals) to Light. *Philosophical Transactions of the Royal Society of London* 147(147):145-181.
9. Martin CR (1994) Nanomaterials - a Membrane-Based Synthetic Approach. (Translated from English) *Science* 266(5193):1961-1966 (in English).
10. Yu YY, Chang SS, Lee CL, & Wang CRC (1997) Gold nanorods: Electrochemical synthesis and optical properties. (Translated from English) *Journal of Physical Chemistry B* 101(34):6661-6664 (in English).
11. Jana NR, Gearheart L, & Murphy CJ (2001) Seeding growth for size control of 5-40 nm diameter gold nanoparticles. (Translated from English) *Langmuir* 17(22):6782-6786 (in English).
12. Gans R (1912) The shape of ultra microscopic gold particles. *Ann. Phys.* (37):881.
13. Oldenburg SJ, Averitt RD, Westcott SL, & Halas NJ (1998) Nanoengineering of optical resonances. *Chemical Physics Letters* 288(2-4):243-247.
14. Halas N (2005) Playing with plasmons. Tuning the optical resonant properties of metallic nanoshells. (Translated from English) *MRS Bull.* 30(5):362-367 (in English).
15. Averitt RD, Westcott SL, & Halas NJ (1999) Linear optical properties of gold nanoshells. *Journal of the Optical Society of America B-Optical Physics* 16(10):1824-1832.
16. Chen JY*, et al.* (2005) Gold nanocages: Engineering their structure for biomedical applications. *Advanced Materials* 17(18):2255-2261.
17. Sun YG, Mayers BT, & Xia YN (2002) Template-engaged replacement reaction: A one-step approach to the large-scale synthesis of metal nanostructures with hollow interiors. *Nano Letters* 2(5):481-485.
18. Merchant B (1998) Gold, the Noble metal and the paradoxes of its toxicology. (Translated from English) *Biologicals* 26(1):49-59 (in English).

19. Paciotti GF, Kingston DGI, & Tamarkin L (2006) Colloidal gold nanoparticles: A novel nanoparticle platform for developing multifunctional tumor-targeted drug delivery vectors. (Translated from English) *Drug Development Research* 67(1):47-54 (in English).
20. Yu KN*, et al.* (2007) Multiplex targeting, tracking, and imaging of apoptosis by fluorescent surface enhanced raman spectroscopic dots. (Translated from English) *Bioconjugate Chemistry* 18(4):1155-1162 (in English).
21. Keren S*, et al.* (2008) Noninvasive molecular imaging of small living subjects using Raman spectroscopy. *Proceedings of the National Academy of Sciences of the United States of America* 105(15):5844-5849.
22. Kneipp J, Kneipp H, Rajadurai A, Redmond RW, & Kneipp K (2009) Optical probing and imaging of live cells using SERS labels. (Translated from English) *J. Raman Spectrosc.* 40(1):1-5 (in English).
23. Qian XM*, et al.* (2008) In vivo tumor targeting and spectroscopic detection with surface-enhanced Raman nanoparticle tags. (Translated from English) *Nature Biotechnology* 26(1):83-90 (in English).
24. Lal S, Clare SE, & Halas NJ (2008) Nanoshell-Enabled Photothermal Cancer Therapy: Impending Clinical Impact. (Translated from English) *Accounts of Chemical Research* 41(12):1842-1851 (in English).
25. Terentyuk GS*, et al.* (2009) Laser-induced tissue hyperthermia mediated by gold nanoparticles: toward cancer phototherapy. (Translated from English) *Journal of Biomedical Optics* 14(2):9 (in English).
26. Liu CH, Mi CC, & Li BQ (2008) Energy absorption of gold nanoshells in hyperthermia therapy. (Translated from English) *Ieee Transactions on Nanobioscience* 7(3):206-214 (in English).
27. Govorov AO & Richardson HH (2007) Generating heat with metal nanoparticles. *Nano Today* 2(1):30-38.
28. Weissleder R (2001) A clearer vision for in vivo imaging. *Nature Biotechnology* 19(4):316-317.
29. Lyon JL, Fleming DA, Stone MB, Schiffer P, & Williams ME (2004) Synthesis of Fe oxide core/Au shell nanoparticles by iterative hydroxylamine seeding. *Nano Letters* 4(4):719-723.
30. Lim JK, Tilton RD, Eggeman A, & Majetich SA (2007) Design and synthesis of plasmonic magnetic nanoparticles. *Journal of Magnetism and Magnetic Materials* 311(1):78-83.
31. Bardhan R*, et al.* (2009) Nanoshells with Targeted Simultaneous Enhancement of Magnetic and Optical Imaging and Photothermal Therapeutic Response. (Translated from English) *Advanced Functional Materials* 19(24):3901-3909 (in English).
32. Zhang J*, et al.* (2006) Laser-assisted synthesis of superparamagnetic Fe@Au core-shell nanoparticles. *Journal of Physical Chemistry B* 110(14):7122-7128.
33. Lin J*, et al.* (2001) Gold-coated iron (Fe@Au) nanoparticles: Synthesis, characterization, and magnetic field-induced self-assembly. (Translated from English) *Journal of Solid State Chemistry* 159(1):26-31 (in English).
34. Skrabalak SE, Au L, Li XD, & Xia Y (2007) Facile synthesis of Ag nanocubes and Au nanocages. *Nature Protocols* 2(9):2182-2190.
35. Freestone I, Meeks N, Sax M, & Higgitt C (2007) The Lycurgus Cup - A Roman nanotechnology. (Translated from English) *Gold Bulletin* 40(4):270-277 (in English).
36. Hayat MAe (1989) Colloidal Gold: Principles, methods, and Applications. *Academic Press New York*.

37. Brust M, Fink J, Bethell D, Schiffrin DJ, & Kiely C (1995) SYNTHESIS AND REACTIONS OF FUNCTIONALIZED GOLD NANOPARTICLES. *Journal of the Chemical Society-Chemical Communications* (16):1655-1656.

38. Brust M, Walker M, Bethell D, Schiffrin DJ, & Whyman R (1994) SYNTHESIS OF THIOL-DERIVATIZED GOLD NANOPARTICLES IN A 2-PHASE LIQUID-LIQUID SYSTEM. *Journal of the Chemical Society-Chemical Communications* (7):801-802.

39. van der Zande BMI, Bohmer MR, Fokkink LGJ, & Schonenberger C (2000) Colloidal dispersions of gold rods: Synthesis and optical properties. *Langmuir* 16(2):451-458.

40. Perez-Juste J, Liz-Marzan LM, Carnie S, Chan DYC, & Mulvaney P (2004) Electric-field-directed growth of gold nanorods in aqueous surfactant solutions. (Translated from English) *Advanced Functional Materials* 14(6):571-579 (in English).

41. F. Fievet JPL, M. Figlarz (1989) Preparing monodisperse metal powers in micrometer and submicrometer sizes by the polyol process. *MRS Bull.* (14):29.

42. Link S & Ei-Sayed MA (2003) Optical properties and ultrafast dynamics of metallic nanocrystals. *Annu. Rev. Phys. Chem.* 54:331-366.

43. Johnson PBC, R. W. (1972) Optical Constants of the Noble Metals. *Physical Review B* 6(12):4370-4379.

44. Kelly KL, Coronado E, Zhao LL, & Schatz GC (2003) The optical properties of metal nanoparticles: The influence of size, shape, and dielectric environment. (Translated from English) *Journal of Physical Chemistry B* 107(3):668-677 (in English).

45. Kreibig U, and Vollmer, M., (1995) *Optical Properties of Metal Clusters*. *Berlin :Springer*.

46. Alvarez MM*, et al.* (1997) Optical absorption spectra of nanocrystal gold molecules. (Translated from English) *Journal of Physical Chemistry B* 101(19):3706-3712 (in English).

47. Feldheim DL CA, Marcel D. (2002) Metal Nanoparticles: Synthesis, characterization and applications. *J. Phys. Chem.* 300(11202-11208).

48. Link S & El-Sayed MA (2000) Shape and size dependence of radiative, non-radiative and photothermal properties of gold nanocrystals. (Translated from English) *Int. Rev. Phys. Chem.* 19(3):409-453 (in English).

49. Hu M*, et al.* (2006) Gold nanostructures: engineering their plasmonic properties for biomedical applications. *Chemical Society Reviews* 35:1084-1094.

50. Link S, Mohamed MB, & El-Sayed MA (1999) Simulation of the optical absorption spectra of gold nanorods as a function of their aspect ratio and the effect of the medium dielectric constant. (Translated from English) *Journal of Physical Chemistry B* 103(16):3073-3077 (in English).

51. Neeves AE & Birnboim MH (1989) COMPOSITE STRUCTURES FOR THE ENHANCEMENT OF NONLINEAR-OPTICAL SUSCEPTIBILITY. *Journal of the Optical Society of America B-Optical Physics* 6(4):787-796.

52. Averitt RD, Sarkar D, & Halas NJ (1997) Plasmon resonance shifts of Au-coated Au2S nanoshells: Insight into multicomponent nanoparticle growth. *Physical Review Letters* 78(22):4217-4220.

53. Radloff C & Halas NJ (2004) Plasmonic properties of concentric nanoshells. (Translated from English) *Nano Letters* 4(7):1323-1327 (in English).

54. Prodan E, Radloff C, Halas NJ, & Nordlander P (2003) A hybridization model for the plasmon response of complex nanostructures. *Science* 302(5644):419-422.

55. Fuchs R (1975) Theory of Optical-Properties of Ionic-Crystal Cubes. (Translated from English) *Physical Review B* 11(4):1732-1739 (in English).

56. Aizpurua J, Rivacoba A, & Apell SP (1996) Electron-energy losses in hemispherical targets. (Translated from English) *Physical Review B* 54(4):2901-2909 (in English).

57. Prodan E, Nordlander P, & Halas NJ (2003) Electronic structure and optical properties of gold nanoshells. (Translated from English) *Nano Letters* 3(10):1411-1415 (in English).
58. Oubre C & Nordlander P (2004) Optical properties of metallodielectric nanostructures calculated using the finite difference time domain method. (Translated from English) *Journal of Physical Chemistry B* 108(46):17740-17747 (in English).
59. Wu YP & Nordlander P (2006) Plasmon hybridization in nanoshells with a nonconcentric core. (Translated from English) *Journal of Chemical Physics* 125(12):10 (in English).
60. Miller EK (1994) Time-Domain Modeling in Electromagnetics. (Translated from English) *Journal of Electromagnetic Waves and Applications* 8(9-10):1125-1172 (in English).
61. Anonymous (Gold nanoparticles are taken up by human cells but do not cause acute cytotoxicity.
62. Lee S*, et al.* (2008) A near-infrared-fluorescence-quenched gold-nanoparticle imaging probe for in vivo drug screening and protease activity determination. (Translated from English) *Angewandte Chemie-International Edition* 47(15):2804-2807 (in English).
63. Jemal A*, et al.* (2009) Cancer Statistics, 2009. *Ca-a Cancer Journal for Clinicians* 59(4):225-249.
64. Crochet JJ*, et al.* (2006) Temperature distribution in selective laser-tissue interaction. *Journal of Biomedical Optics* 11(3).
65. Zharov VP, Mercer KE, Galitovskaya EN, & Smeltzer MS (2006) Photothermal nanotherapeutics and nanodiagnostics for selective killing of bacteria targeted with gold nanoparticles. *Biophysical Journal* 90(2):619-627.
66. Dickerson EB*, et al.* (2008) Gold nanorod assisted near-infrared plasmonic photothermal therapy (PPTT) of squamous cell carcinoma in mice. (Translated from English) *Cancer Letters* 269(1):57-66 (in English).
67. O'Neal DP, Hirsch LR, Halas NJ, Payne JD, & West JL (2004) Photo-thermal tumor ablation in mice using near infrared-absorbing nanoparticles. *Cancer Letters* 209(2):171-176.
68. Stern JM, Stanfield J, Kabbani W, Hsieh JT, & Cadeddu JRA (2008) Selective prostate cancer thermal ablation with laser activated gold nanoshells. (Translated from English) *Journal of Urology* 179(2):748-753 (in English).
69. Au L*, et al.* (2008) A quantitative study on the photothermal effect of immuno gold nanocages targeted to breast cancer cells. (Translated from English) *Acs Nano* 2(8):1645-1652 (in English).
70. Anonymous (Gold Nanocages Synthesis Properties and application.
71. Ohmori T (1984) Role of a surface disruption of electrode in electrochemical characteristics.1.influence of a surface disruption of electrode on the rate of the hydrogen evolution reaction. (Translated from English) *Journal of Electroanalytical Chemistry* 172(1-2):123-130 (in English).
72. Kato M*, et al.* (2002) Substrate (Ni)-catalyzed electroless gold deposition from a noncyanide bath containing thiosulfate and sulfite - I. Reaction mechanism. *Journal of the Electrochemical Society* 149(3):C164-C167.
73. Liew MJ, Roy S, & Scott K (2003) Development of a non-toxic electrolyte for soft gold electrodeposition: an overview of work at University of Newcastle upon Tyne. (Translated from English) *Green Chem.* 5(4):376-381 (in English).
74. Kato M & Okinaka Y (2004) Some recent developments in non-cyanide gold plating for electronics applications. *Gold Bulletin* 37(1-2):37-44.
75. Green TA & Roy S (2006) Speciation analysis of Au(I) electroplating baths containing sulfite and thiosulfate. *Journal of the Electrochemical Society* 153(3):C157-C163.

76. Mordechay Schlesinger MP (2000) *Modern electroplating* (Wiley interscience) 4th Ed.
77. Honma H & Kagaya Y (1993) Gold plating using the disulfiteaurate complex. (Translated from English) *Journal of the Electrochemical Society* 140(9):L135-L137 (in English).
78. Okinaka Y & Hoshino M (1998) Some recent topics in gold plating for electronics applications. *Gold Bulletin* 31(1):3-13.
79. Honma H, Hasegawa A, Hotta S, & Hagiwara K (1995) Electroless gold plating by disulfiteaurate complex. (Translated from English) *Plat. Surf. Finish.* 82(4):89-92 (in English).
80. Morrissey RJ (1994) US.
81. P. Laude EM, and Z. Morrens (1980) Patent U.
82. He A, Liu Q, & Ivey DG (2009) Electroplating of gold from a solution containing tri-ammonium citrate and sodium sulphite. *Journal of Materials Science-Materials in Electronics* 20(6):543-550.
83. Green TA, Liew MJ, & Roy S (2003) Electrodeposition of gold from a thiosulfate-sulfite bath for microelectronic applications. *Journal of the Electrochemical Society* 150(3):C104-C110.
84. Osaka T*, et al.* (1997) Electrodeposition of soft gold from a thiosulfate-sulfite bath for electronics applications. *Journal of the Electrochemical Society* 144(10):3462-3469.
85. Liew MJ, Sobri S, & Roy S (2005) Characterisation of a thiosulphate-sulphite gold electrodeposition process. *Electrochimica Acta* 51(5):877-881.
86. Kibria AKMF (2008) Effect of ethylene diamine tetra acetic acid (EDTA) on the surface reaction behavior and the hydrogen evolution efficiency of Ni-30at. %Cu electrode in alkaline medium. *Bangladesh Journal of Scientific and Industrial Research* 43(2):145-158.
87. Vandeberg PJ & Johnson DC (1993) A study of the voltammetric response of thiourea and ethylene thiourea at gold electrode in alkaline media. *Journal of Electroanalytical Chemistry* 362(1-2):129-139.
88. Jaksic MM, Brun J, Johansen B, & Tunold R (1995) The Rowland or EDTA effect on electrochemical behavior of transition metals and in electrocatalysis for the hydrogen evolution reaction. The Rowland effect on some non-noble non-valve transition metals. *Russian Journal of Electrochemistry* 31(11):1187-1202.
89. Milan Paunovic MS (2006) Fundamentals of Electrochemical Deposition. *Wiley*.
90. Fernando CAN & Wetthasinghe SK (2000) Investigation of photoelectrochemical characteristics of n-type Cu2O films. (Translated from English) *Sol. Energy Mater. Sol. Cells* 63(3):299-308 (in English).
91. Lacovangelo CD & Zarnoch KP (1991) Substrate-catalyzed electroless gold plating (Translated from English) *Journal of the Electrochemical Society* 138(4):983-988 (in English).
92. Porter LA, Choi HC, Ribbe AE, & Buriak JM (2002) Controlled electroless deposition of noble metal nanoparticle films on germanium surfaces. *Nano Letters* 2(10):1067-1071.
93. Sato J*, et al.* (2002) Substrate (Ni)-catalyzed electroless gold deposition from a noncyanide bath containing thiosulfate and sulfite - II. Deposit characteristics and substrate effects. (Translated from English) *Journal of the Electrochemical Society* 149(3):C168-C172 (in English).
94. Oskam G, Long JG, Natarajan A, & Searson PC (1998) Electrochemical deposition of metals onto silicon. (Translated from English) *J. Phys. D-Appl. Phys.* 31(16):1927-1949 (in English).

95. Vogt H (1982) The Rate of Hydrogen Generation in the Electrodeposition of Metal-Powder at Gas-Evolving Electrodes. (Translated from English) *Surface Technology* 17(4):301-307 (in English).
96. Sawyer DT, Sobkowiak A, & Roberts JL (1995) *Electrochemistry for chemists*.
97. Boateng DA, Ng TC, Phllips CR, & Tombalaklan AS (1981) Production of nickel by hydrogen reduction of nickel-loaded organic acid solution. *Ind. Eng. Chem. Process Des. Dev.* 20.
98. Norskov JK*, et al.* (2005) Trends in the exchange current for hydrogen evolution. (Translated from English) *J. Electrochem. Soc.* 152(3):J23-J26 (in English).
99. Ljunggren S & Eriksson JC (1997) The lifetime of a colloid-sized gas bubble in water and the cause of the hydrophobic attraction. *Colloids and Surfaces a-Physicochemical and Engineering Aspects* 130:151-155.
100. Brenner MP & Lohse D (2008) Dynamic equilibrium mechanism for surface nanobubble stabilization. (Translated from English) *Phys. Rev. Lett.* 101(21):4 (in English).
101. Tyrrell JWG & Attard P (2001) Images of nanobubbles on hydrophobic surfaces and their interactions. (Translated from English) *Phys. Rev. Lett.* 87(17):4 (in English).
102. Zhang XH, Maeda N, & Craig VSJ (2006) Physical properties of nanobubbles on hydrophobic surfaces in water and aqueous solutions. (Translated from English) *Langmuir* 22(11):5025-5035 (in English).
103. Zhang XH*, et al.* (2004) Degassing and temperature effects on the formation of nanobubbles at the mica/water interface. (Translated from English) *Langmuir* 20(9):3813-3815 (in English).
104. Yang SJ*, et al.* (2007) Characterization of nanobubbles on hydrophobic surfaces in water. (Translated from English) *Langmuir* 23(13):7072-7077 (in English).
105. Zhang XH, Quinn A, & Ducker WA (2008) Nanobubbles at the interface between water and a hydrophobic solid. (Translated from English) *Langmuir* 24(9):4756-4764 (in English).
106. Attard P (2003) Nanobubbles and the hydrophobic attraction. (Translated from English) *Adv. Colloid Interface Sci.* 104:75-91 (in English).
107. Tyrrell JWG & Attard P (2002) Atomic force microscope images of nanobubbles on a hydrophobic surface and corresponding force-separation data. (Translated from English) *Langmuir* 18(1):160-167 (in English).
108. Lou ST*, et al.* (2000) Nanobubbles on solid surface imaged by atomic force microscopy. (Translated from English) *J. Vac. Sci. Technol. B* 18(5):2573-2575 (in English).
109. Attard P, Moody MP, & Tyrrell JWG (2002) Nanobubbles: the big picture. (Translated from English) *Physica A* 314(1-4):696-705 (in English).
110. Zhang LJ*, et al.* (2006) Electrochemically controlled formation and growth of hydrogen nanobubbles. (Translated from English) *Langmuir* 22(19):8109-8113 (in English).
111. Wang QT, Wang GZ, Han XH, Wang XP, & Hou JG (2005) Controllable template synthesis of Ni/Cu nanocable and Ni nanotube arrays: A one-step coelectrodeposition and electrochemical etching method. *Journal of Physical Chemistry B* 109(49):23326-23329.
112. Cao HQ*, et al.* (2006) Generation and growth mechanism of metal (Fe, Co, Ni) nanotube arrays. *Chemphyschem* 7(7):1500-1504.
113. Issa NA & Guckenberger R (2007) Optical nanofocusing on tapered metallic waveguides. (Translated from English) *Plasmonics* 2(1):31-37 (in English).
114. Mermin NWAaND (1976) Solid State Plysics. *Saunders philadelphia*.
115. U. Kreibig MV (1995) Optical Properties of Metal Clussters. *Textbook*.
116. Quinten M & Kreibig U (1986) OPTICAL-PROPERTIES OF AGGREGATES OF SMALL METAL PARTICLES. *Surface Science* 172(3):557-577.

117. Knight MW & Halas NJ (2008) Nanoshells to nanoeggs to nanocups: optical properties of reduced symmetry core-shell nanoparticles beyond the quasistatic limit. (Translated from English) *New Journal of Physics* 10:- (in English).
118. Wang H*, et al.* (2006) Symmetry breaking in individual plasmonic nanoparticles. (Translated from English) *Proceedings of the National Academy of Sciences of the United States of America* 103(29):10856-10860 (in English).
119. Wang H, Fu K, Drezek RA, & Halas NJ (2006) Light scattering from spherical plasmonic nanoantennas: effects of nanoscale roughness. (Translated from English) *Applied Physics B-Lasers and Optics* 84(1-2):191-195 (in English).
120. Wang H & Halas NJ (2008) Mesoscopic Au "Meatball" particles. *Adv. Mater.* 20(4):820-+.
121. Banholzer MJ*, et al.* (2008) Electrochemical approach to and the physical consequences of preparing nanostructures from gold nanorods with smooth ends. (Translated from English) *J. Phys. Chem. C* 112(40):15729-15734 (in English).
122. Bok HM, Shuford KL, Kim S, Kim SK, & Park S (2008) Multiple surface plasmon modes for a colloidal solution of nanoporous gold nanorods and their comparison to smooth gold nanorods. (Translated from English) *Nano Lett.* 8(8):2265-2270 (in English).
123. Wang H*, et al.* (2005) Controlled texturing modifies the surface topography and plasmonic properties of au nanoshells. *Journal of Physical Chemistry B* 109(22):11083-11087.
124. Wang ZB*, et al.* (2008) The influences of particle number on hot spots in strongly coupled metal nanoparticles chain. (Translated from English) *Journal of Chemical Physics* 128(9):- (in English).
125. Perrault SD, Walkey C, Jennings T, Fischer HC, & Chan WCW (2009) Mediating Tumor Targeting Efficiency of Nanoparticles Through Design. (Translated from English) *Nano Letters* 9(5):1909-1915 (in English).
126. Merrill EW*, et al.* (1982) PLATELET-COMPATIBLE HYDROPHILIC SEGMENTED POLYURETHANES FROM POLYETHYLENE GLYCOLS AND CYCLOHEXANE DIISOCYANATE. *Transactions American Society for Artificial Internal Organs* 28:482-487.
127. Moghimi SM, Muir IS, Illum L, Davis SS, & Kolbbachofen V (1993) COATING PARTICLES WITH A BLOCK-COPOLYMER (POLOXAMINE-908) SUPPRESSES OPSONIZATION BUT PERMITS THE ACTIVITY OF DYSOPSONINS IN THE SERUM. *Biochimica Et Biophysica Acta* 1179(2):157-165.
128. Conti Devirgiliis L, Dini L, & Russo-Caia S (1984) Electron microscopic evidence for the presence of an asialoglycoprotein receptor on isolated foetal rat hepatocyte surface. *J Embryol Exp Morphol* 79:41-51.
129. Mosmann T (1983) RAPID COLORIMETRIC ASSAY FOR CELLULAR GROWTH AND SURVIVAL - APPLICATION TO PROLIFERATION AND CYTO-TOXICITY ASSAYS. *Journal of Immunological Methods* 65(1-2):55-63.
130. Anonymous (Plasmonic photothermal therapy (PPTT) using gold nanoparticles.
131. Rashidi-Huyeh M & Palpant B (2004) Thermal response of nanocomposite materials under pulsed laser excitation. (Translated from English) *Journal of Applied Physics* 96(8):4475-4482 (in English).
132. Mohamed MB, Ahmadi TS, Link S, Braun M, & El-Sayed MA (2001) Hot electron and phonon dynamics of gold nanoparticles embedded in a gel matrix. (Translated from English) *Chemical Physics Letters* 343(1-2):55-63 (in English).
133. Hu M & Hartland GV (2002) Heat dissipation for Au particles in aqueous solution: Relaxation time versus size. (Translated from English) *Journal of Physical Chemistry B* 106(28):7029-7033 (in English).

134. Baffou G, Quidant R, & Girard C (2009) Heat generation in plasmonic nanostructures: Influence of morphology. (Translated from English) *Applied Physics Letters* 94(15):- (in English).
135. Seino S*, et al.* (2005) Gamma-ray synthesis of magnetic nanocarrier composed of gold and magnetic iron oxide. *Journal of Magnetism and Magnetic Materials* 293(1):144-150.
136. Kang YS, Risbud S, Rabolt JF, & Stroeve P (1996) Synthesis and characterization of nanometer-size Fe3O4 and gamma-Fe2O3 particles. (Translated from English) *Chemistry of Materials* 8(9):2209-& (in English).
137. Shevchenko EV*, et al.* (2008) Gold/Iron Oxide Core/Hollow-Shell Nanoparticles. (Translated from English) *Adv. Mater.* 20(22):4323-4329 (in English).

BIOGRAPHICAL INFORMATION

Chienwen (Kevin) Huang was born in Taiwan. He received his bachelor degree in chemistry engineering from Tamkang University in 2002. After that, he joined two years military training in Taiwan. In 2010, he received his Ph.D. degree in Materials Science and Engineering from the University of Texas at Arlington. He was a secretary of North Texas Chapter of ASM International, and also volunteered as an amateur photographer in MSE department during his Ph.D. education. His research focused upon the chemical and physical fabrication of nanoscale structures using sputtering, evaporation and electrochemical deposition. He has successfully fabricated several unique nanostructures such as magnetic and novel metallic nanotubes, nanorods and hollow nanostructures that can be used for biomedical applications. The results were published in several high-impact journals and also filed for the patent. As an engineer, he was well-trained to analyze the resulting nanostructures using various characterization tools, such as analytical transmission electron microscopy (TEM), high-resolution TEM, scanning electron microscopy (SEM), x-ray diffraction (XRD), energy dispersive spectrometer (EDS), auger electron spectroscopy (AES) and x-ray photoelectron spectroscopy (XPS), vibration sample magnetometer (VSM), alternative gradient magnetometer (AGM) and UV/vis spectroscopy. Moreover, through the collaboration with the University of Texas Southwestern Medical Center at Dallas, he conducted several biological studies such as cell culture, cytotoxicity and photothermal for cancer treatment.